Barium Disilicide for Photovoltaic Applications

Thin-Film Synthesis and Characterizations

Tian, Y.

DOI
10.4233/uuid:87c8e518-2abf-476b-a482-9a31049367d1

Publication date
2021

Document Version
Final published version

Citation (APA)
Tian, Y. (2021). *Barium Disilicide for Photovoltaic Applications: Thin-Film Synthesis and Characterizations*. [Dissertation (TU Delft), Delft University of Technology]. https://doi.org/10.4233/uuid:87c8e518-2abf-476b-a482-9a31049367d1

Barium Disilicide for Photovoltaic Applications

Thin-Film Synthesis and Characterizations

Yilei TIAN

田义磊

Barium Disilicide for Photovoltaic Applications

Thin-Film Synthesis and Characterizations

Proefschrift

ter verkrijging van de graad van doctor
aan de Technische Universiteit Delft,
op gezag van de Rector Magnificus Prof.dr.ir. T.H.J.J. van der Hagen,
voorzitter van het College voor Promoties,
in het openbaar te verdedigen op donderdag 17 juni 2021 om 10:00 uur

door

Yilei TIAN

Master of Engineering in Power Engineering and Engineering Thermophysics, Zhejiang University, China
geboren te Xiaogan, China

Dit proefschrift is goedgekeurd door de promotoren.

Samenstelling promotiecommissie bestaat uit:

Rector Magnificus	voorzitter
Prof.dr. M. Zeman	Technische Universiteit Delft, promotor
Dr. O. Isabella	Technische Universiteit Delft, promotor
Onafhankelijke leden:	
Prof.dr. T. Suemasu	University of Tsukuba, Japan
Prof.dr. S.O. Binetti	University of Milano-Bicocca, Italy
Prof.dr. P. Roca i Cabarrocas	Polytechnic Institute of Paris, France
Prof.dr. B. Dam	Technische Universiteit Delft
Dr. S.W.H. Eijt	Technische Universiteit Delft
Prof.dr. P. Palensky	Technische Universiteit Delft, reservelid

Keywords: Barium Disilicide, Sputtering, Thin Films, Photovoltaics

Printed by: Ipskamp Printing

Front & Back: Designed by Y. Tian, from a photograph image of the AES analysis instrument used in this research.

ISBN 978-94-6421-380-5

An electronic version of this dissertation is available at
`http://repository.tudelft.nl/`.

Contents

Summary

Energy and materials have been assigned with great significance for the development of society over the past centuries. For the sake of environmental sustainability, earth-abundant and eco-friendly materials for energy utilization have been gaining increasing attention. Among them, barium disilicide ($BaSi_2$) possesses attractive optical and electrical properties, enabling its potential for achieving low-cost and high-efficiency thin-film solar cells. This research provides a systematical investigation on sputtered $BaSi_2$ ranging from thin-film fabrication to properties characterizations.

Chapter 1 gives a general introduction about solar energy and photovoltaics. The prospects and challenges of thin-film solar cell technology are discussed.

Chapter 2 is a literature review of $BaSi_2$, including material structure, optical and electrical properties, thin-film fabrications, and recent advancements in $BaSi_2$-based solar cell development.

Chapter 3 lists experimental methods used in this research including deposition techniques and material characterization methods.

Chapter 4 exhibits the fabrication of poly-crystalline $BaSi_2$ films via sputtering with subsequent high-temperature annealing in N_2 atmosphere. The film thickness uniformity is determined by the target-to-substrate distance. The surface oxidation during high-temperature annealing results in the inhomogeneous structure of sputtered $BaSi_2$ films. An oxidation-induced structural transformation mechanism of $BaSi_2$ is proposed, which describes the complex reactions and elemental diffusion within the $BaSi_2$ film at high-temperature conditions.

Chapter 5 explores the effects of vacuum annealing condition on sputtered $BaSi_2$ film properties. The vacuum annealing method enables the $BaSi_2$ crystallization at 600 °C, and decreases the thickness of the surface oxide layer from ~200 nm (in N_2 atmosphere) to ~100 nm.

In Chapter 6, a face-to-face annealing (FTFA) approach is applied for the post-growth treatment of sputtered $BaSi_2$ films, which improves surface composition homogeneity and crystal quality of sputtered $BaSi_2$. By employing various covers for FTFA including $BaSi_2$, silicon, and glass, a transition of conductivity type from n- to p-type is observed. Thermal resistance analysis is carried out to understand the mechanism of the FTFA method and its impacts on the film crystallization process and properties.

Chapter 7 investigates the interface properties of Si/$BaSi_2$/Si hetero-structures serving as the fundamental for the development of $BaSi_2$/Si heterojunction solar cells. The effects of Si layer thickness on the composition and structure of Si/$BaSi_2$/Si under high-temperature conditions are analyzed. A thick Si layer ($d_{Si} > 20$ nm) can effectively suppress the surface oxidation and elemental diffusion during the high-temperature annealing. The process of structure and composition variations of Si/$BaSi_2$/Si samples consist of the oxidation of deposited Si layer, growth of the oxide layer, Ba diffusion and depletion, as well as Si isolation and crystallization. These interfacial phenomena lead to the

complex structure and composition of Si/$BaSi_2$/Si heterostructures.

Conclusions of this thesis and outlook for the future development of the material and devices are listed in Chapter 8. Recommendations are given for high-quality $BaSi_2$ film fabrications and solar cell development.

This thesis provides insights into $BaSi_2$ films from perspectives of thin-film depositions via sputtering and property characterizations. These results and knowledge shed light on fabrications of $BaSi_2$ films for the goal of efficient $BaSi_2$-based solar cells.

Samenvatting

Energie en materialen zijn gedurende de afgelopen eeuwen van groot belang beschouwd voor het ontwikkelen van de samenleving. In het belang van duurzaamheid wordt er met toenemende aandacht gekeken naar materialen die ruim beschikbaar en ecologisch verantwoord zijn. Van deze materialen bezit bariumdisilicide ($BaSi_2$) veelbelovende optische en elektrische eigenschappen, wat het een kandidaat voor goedkope en efficiënte dunne-laag zonnecellen maakt. Dit onderzoek presenteert een systematische analyse van gesputterde $BaSi_2$, reikend van dunne-film fabricatie tot de karakterisering van materiaaleigenschappen.

Hoofdstuk 1 geeft een algemene introductie van fotovoltaïsche zonne-energie. Hierin worden de vooruitzichten en uitdagingen van dunne-film zonnecel technologie besproken.

Hoofdstuk 2 is een literatuuroverzicht van $BaSi_2$ waarin materiaalstructuur, optische en elektrische eigenschappen, dunne-film fabricatie en recente vorderingen in op $BaSi_2$ gebaseerde zonnecelontwikkeling worden besproken.

Hoofdstuk 3 presenteert de experimentele methoden gebuikt in dit onderzoek, waaronder depositietechnieken en materiaalkarakteriseringsmethoden.

Hoofdstuk 4 vertoont de fabricatie van polykristallijne $BaSi_2$ films door middel van sputteren en daaropvolgend hoge-temperatuur warmtebehandeling in een N_2 atmosfeer. De gelijkmatigheid van de filmdikte wordt bepaald door de bron-tot-substraat afstand. De oppervlakteoxidatie gedurende hoge-temperatuur warmtebehandeling resulteert in de inhomogene structuur van gesputterde $BaSi_2$ films. Een oxidatie-geïnduceerde structureel transformatiemechanisme voor $BaSi_2$ wordt voorgesteld, die een beschrijving geeft voor de complexe reacties en elementaire diffusies in de $BaSi_2$ films onder hoge-temperatuur condities.

Hoofdstuk 5 verkent de effecten van vacuüm-warmtebehandeling omstandigheden op gesputterde $BaSi_2$ film eigenschappen. De vacuüm-warmtebehandeling methode maakt kristallisatie van $BaSi_2$ bij 600 °C mogelijk en reduceert de dikte van de oxide-laag van ~200 nm (in N_2 atmosfeer) naar ~100 nm.

In hoofdstuk 6 wordt een laag-tot-laag warmtebehandeling (face-to-face annealing, FTFA) toegepast als nabehandeling van gesputterde $BaSi_2$ films, wat de oppervlaktecompositiehomogeniteit en kristalkwaliteit van gesputterde $BaSi_2$ verbeterd. Door verschillende bedekkingen voor FTFA te gebruiken, waaronder $BaSi_2$, silicium en glas, wordt een overgang in geleidingstype van n- naar p-type waargenomen. Thermische weerstandsanalyse wordt toegepast om het mechanisme van de FTFA-methode en diens invloed op het kristallisatieproces en de eigenschappen van films te begrijpen.

Hoofdstuk 7 onderzoekt de grensvlakeigenschappen van $Si/BaSi_2/Si$ hetero-structuren ter grondlegging van het ontwikkelen van $BaSi_2/Si$ heterojunctie zonnecellen. Het effect van de Si laagdikte op de samenstelling en structuur van $Si/BaSi_2/Si$ onder hoge-temperatuurcondities wordt geanalyseerd. Een dikke Si laag ($d_{Si} > 20$ nm) kan effectief

de oppervlakteoxidatie en elementaire diffusie gedurende hoge-temperatuur warmtebehandeling onderdrukken. Het proces van structuur- en compositievariatie van Si/$BaSi_2$/Si proefstukken bestaat uit de oxidatie van de gedepositioneerde Si laag, de groei van de oxide-laag, Ba diffusie en uitputting en Si isolatie en kristallisatie. Deze grensvlakverschijnselen lijden tot de complexe structuur en compositie van Si/$BaSi_2$/Si heterojuncties.

De conclusies van deze scriptie en de vooruitzichten voor toekomstige ontwikkelingen van het materiaal en de apparaten worden opgesomd in Hoofdstuk 8. Aanbevelingen worden gegeven voor hoge-kwaliteit $BaSi_2$ film fabricatie en de ontwikkeling van zonnecellen.

Deze scriptie biedt inzicht in $BaSi_2$ films vanuit het perspectief van dunne-film depositie door middel van sputteren en eigenschap karakterisering. Deze resultaten en kennis werpen licht op de fabricatie van $BaSi_2$ films met als doel efficiënte zonnecellen gebaseerd op $BaSi_2$.

1

Introduction

1

1.1. Energy and photovoltaics

Meeting the rising demand of energy has been a pressing challenge facing humanity. Owing to global warming caused by the burning of fossil fuels, and geopolitical tensions over oil resources and nuclear energy, we are striving to accomplish a transition from traditional energy sources towards renewable energy sources, such as hydro, wind, and solar energy. Photovoltaics (PV), the direct conversion of light into electricity, is increasingly important in this transition.

1.1.1. Energy and sustainability

The rapid economic growth has radically transformed the primary energy mix over the last few centuries, as shown in Figure 1.1. Before the industrial revolution, the main source of energy was wood and other traditional biomass. From the latter half of the 19th century, fossil fuels such as coal, oil, gas became the major primary sources of energy. The energy consumption kept increasing rapidly during the last century. Nowadays, the main source of energy even in highly developed countries is still fossil fuels. This energy infrastructure that heavily depends on fossil fuels has aroused concerns of sustainability and environment.

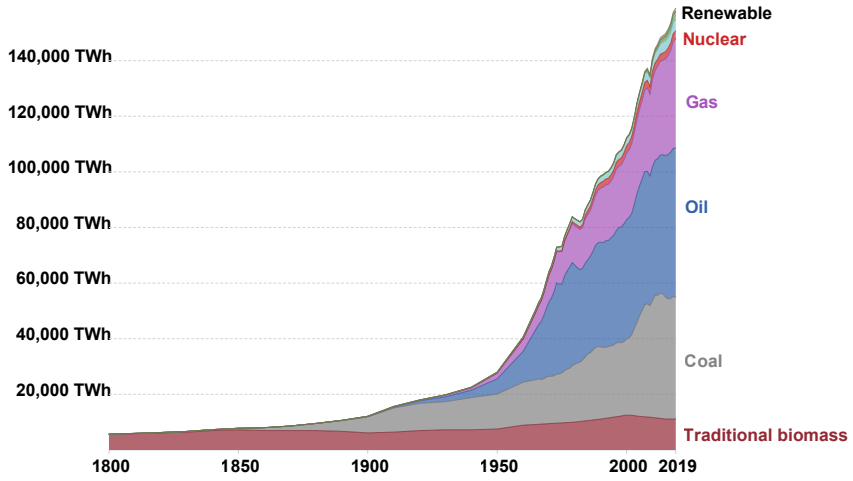

Figure 1.1: Global direct primary energy consumption. *Renewable* refers to renewable energy sources including hydro, wind, solar energy, geothermal, biomass, etc. Reproduced from Ref. [1].

Resources of fossil fuel are limited, and its production and consumption irreversibly affect the environmental conditions with the threat of catastrophic climate change on Earth. One major environmental impact of fossil fuels is the emission of green-house gases such as CO_2. The large growth in global CO_2 emissions caused by the burning of fossil fuel has had a significant impact on the concentrations of CO_2 in Earth's atmosphere. Since the Industrial Revolution, global CO_2 concentrations have been increasing rapidly. In the long term, we see that today's concentrations are the highest they have been for at least 800,000 years. CO_2 concentration did not exceed 300 ppm throughout the cycles of ice ages and warmer interglacials, yet today it is well over 400 ppm and

continues to rise [2]. The accumulation of CO_2 in the atmosphere leads to global temperature rise or global warming. The consequences of global warming include changes in rainfall patterns, extreme storms, heat-wave intensification, and rising sea levels.

These facts and concerns aroused the interest in renewable energy sources, such as hydro, wind, and solar energy. In contrast to fossil fuels, these renewable energy carriers can be replenished by natural processes at a rate comparable or faster than the consumption rates. Additionally, they can be converted to electricity without giving rise to carbon dioxide and other greenhouse gas emissions. Renewable energy sources are starting to be used as the panacea for solving climate change or global warming problems. Figure 1.2 shows the rapid increase of electricity production contributed by renewable energy sources. In 2019, around 11% of global primary energy came from renewable energy sources.

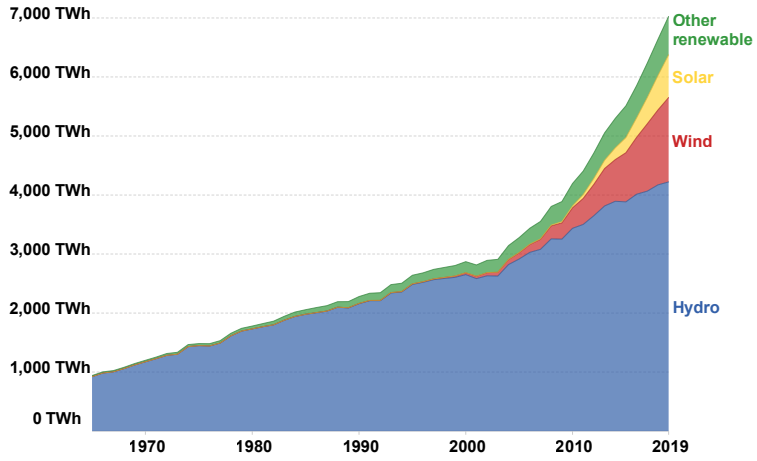

Figure 1.2: Electricity production from renewable energy sources. "Other renewables" refers to renewable energy sources including geothermal, biomass, waste, wave, and tidal. Adapted from Ref. [3].

Among these renewable energy sources, solar energy shows its inherent advantages that it is clean, quiet, and inexhaustible. The power of solar radiation on the Earth's surface exceeds the world's energy consumption by more than 1000 times. Figure 1.3 shows the share of primary energy that comes from solar energy across the world. In 2019, around 1% of global energy consumption was made up by solar energy, and 2% of global electricity was produced from solar energy.

Solar energy can be utilized by the direct conversion into electricity (photovoltaics), the conversion into heat (solar thermal energy), and the conversion into chemical energy (solar fuels). Currently, photovoltaics is the major path for harvesting solar energy and is increasingly important in the inevitable transition from our current level of dependence on fossil fuels.

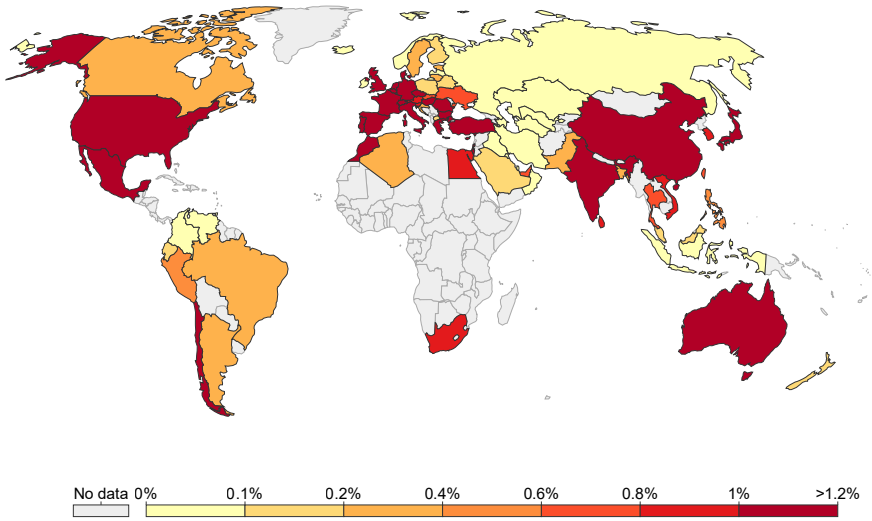

Figure 1.3: Share of primary energy from solar energy of 2019. Adapted from Ref. [3].

1.1.2. Photovoltaics

Photovoltaics is the direct conversion of solar energy into electricity, which process is facilitated by the device called solar cell. The working principle of solar cells is based on the photovoltaic effect, the generation of a potential difference at the junction of two different materials in response to electromagnetic radiation. Figure 1.4 illustrates a typical solar cell structure with external load. The generation of the potential difference consists of the following steps:

1. generation of charge carriers due to the absorption of light in the absorber material of the solar cell;
2. separation of the light-generated charge carriers;
3. collection of the light-generated charge carriers.

A typical current-voltage (I-V) characteristic of a solar cell is presented in Figure 1.5, which is used to characterize the solar cell performance. When in the dark, the solar cell performs as a p-n diode. When the device is under the illumination, following key parameters of a solar cell can be defined from the I-V curve:

- **Short-circuit current** (I_{SC}), which is measured when the output terminal is shorted ($V = 0$). I_{SC} represents the maximum current provided by the solar cell at a certain illumination level.
- **Open-circuit voltage** (V_{OC}), which is measured when the output terminal is opened ($I = 0$). V_{OC} represents the maximum voltage of solar cell at a certain illumination level.

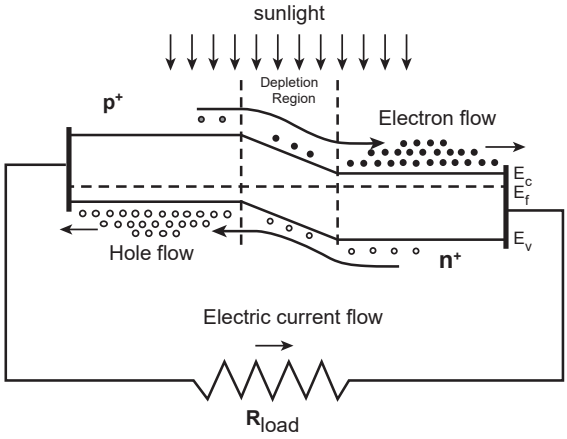

Figure 1.4: Illustration of a solar cell device structure in the form of p-n diode with external load. Reproduced from Ref. [4].

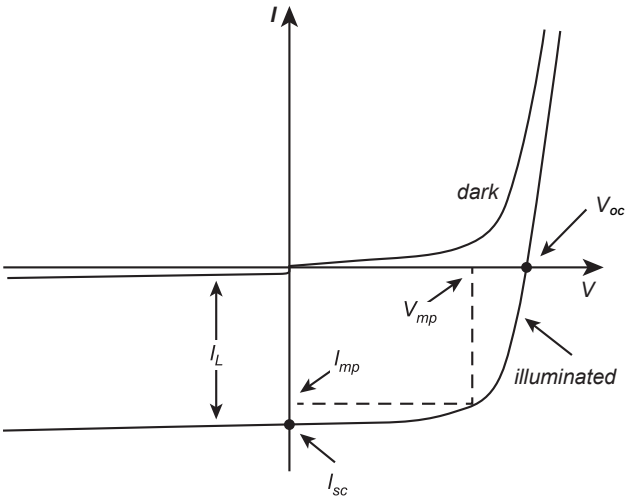

Figure 1.5: I-V characteristic of the solar cell in the dark and under illumination.

- **Fill factor (*FF*)**, which represents the ratio between the maximum power ($P_{\mathrm{MP}} = V_{\mathrm{MP}} I_{\mathrm{MP}}$, indicated in Figure 1.5) and the product I_{SC} times V_{OC}:

$$FF = \frac{V_{\mathrm{MP}} I_{\mathrm{MP}}}{V_{\mathrm{OC}} I_{\mathrm{SC}}}. \tag{1.1}$$

- **Conversion efficiency** (η), which is defined as the ratio of the electrical energy output to the total incoming sun-light energy striking the surface of the cell (P_{in}):

$$\eta = \frac{V_{\text{MP}} I_{\text{MP}}}{P_{\text{in}}} = \frac{V_{\text{OC}} I_{\text{SC}}}{P_{\text{in}}} FF. \tag{1.2}$$

Since the discovery of the photovoltaic effect in 1839, and the first modern solar cell in 1954, consistent efforts have been made to achieve high-efficient solar cells, ranging from the fundamental research on emerging materials and technologies, to the optimizations and improvements on commercial solar cells.

1.2. Thin-film solar cells

Currently, the major solar cell types are wafer-based silicon solar cells (c-Si) and thin-film solar cells, e.g., solar cells based on amorphous (a-Si) and micro-crystalline (μc-Si) silicon, cadmium telluride (CdTe), and copper indium gallium selenide (CIGS). Solar cells based on III-V semiconductors, e.g., GaAs and InGaP, though normally in form of thin film, are considered as a separate family of solar cells, owing to their high cost and applications in special areas.

Thin-film solar cells are significantly thinner than wafer-based solar cells. The typical thickness of thin-film solar cells ranges from a few hundred nanometers to several micrometers. Carriers are required for thin-film solar cells to ensure their mechanical stability. These carriers can either be rigid (e.g., glass) or flexible (e.g., metal foils, polymer). These features make thin-film solar cells a good candidate for low-cost and lightweight applications, including high-value markets in aerospace, person-portable and vehicle-integrated products, and building-integrated PV (BIPV) [5].

Despite the promise and potential that thin-film solar cells hold, some drawbacks and disadvantages hinder their market expansions. In 2019, only 5% market is made up by the thin-film solar cells, while c-Si solar cells accounted for about 95% of the global market share. The main concerns of thin-film solar cells stem from their conversion efficiency, manufacturing cost, raw materials, and environmental impacts.

Table 1.1 summarises the conversion efficiency records of some thin-film solar cells. Thin-film silicon (a-Si and μc-Si) solar cells presents a significant disadvantage in the conversion efficiency with respect to wafer-based c-Si solar cells which holds a conversion efficiency record of 26.7% [6]. CIGS and CdTe thin-film solar cells show higher energy conversion efficiencies as compared to thin-film silicon solar cells. This allows them occupy the main thin-film solar market. However, their module efficiencies are still lower than that of c-Si module. The record module efficiencies of CIGS and CdTe are 19.2% and 19.0%, respectively, while the record of c-Si module is 24.4% [6]. The full potential of CIGS and CdTe is still untapped, and continues efforts are being made to improve their cell and module performances.

CIGS and CdTe technologies also face other challenges. As CIGS is deposited in a complex process, it is challenging to perform large-scale deposition with a high production yield, and the manufacturing cost of CIGS is less competitive compared to c-Si solar cells. Besides, the utilization of and scarce and/or toxic elements is another concern that should be addressed. Figure 1.6 shows the abundance in the Earth's crust of

Table 1.1: Summary of thin-film solar cell performance records

Type	η [%]	V_{OC} [V]	I_{SC} [mA/cm^2]	FF [%]	Reference
a-Si	10.2	0.896	16.36	69.8	[7]
µc-Si	11.9	0.550	29.72	75.0	[8]
CIGS	23.35	0.734	39.58	80.4	[9]
CdTe	22.1	0.8872	31.69	78.5	[10]
Emerging photovoltaics					
Perovskite	25.2	1.1805	25.14	84.8	[11]
Dye sensitised	12.5	1.025	15.76	77.4	[12]
Organic	17.35	0.862	25.83	78.0	[13]

several elements. Rare or scarce elements, such as Te, Cd, In, Ga, as shown in Figure 1.6, are used in CdTe or CIGS. Moreover, both CdTe (larger amounts) and CIGS (smaller amounts) use Cd, which is classified as one of the most toxic substances. Disposal of the Cd-containing products causes adverse effects on the environment, and produces toxic effects on humans. These issues or concerns related to manufacturing, raw materials, and environmental impacts need to be solved or addressed for the development of thin-film solar cells.

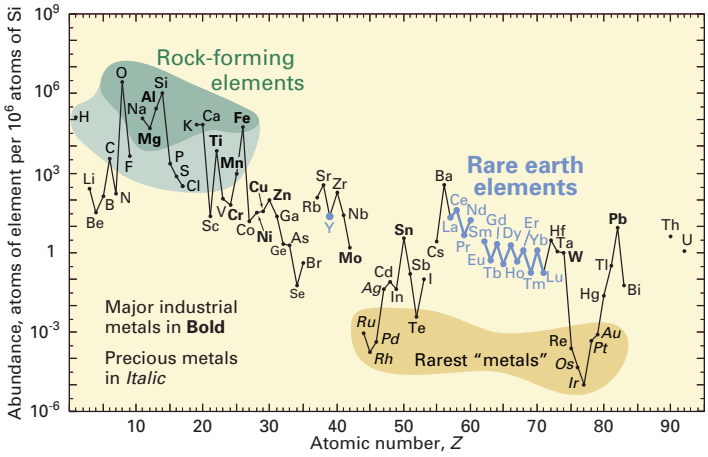

Figure 1.6: Abundance (atom fraction) of the chemical elements in Earth's upper continental crust as a function of atomic number, adapted from Ref. [14].

Besides these commercialized thin-film solar cell technologies, "emerging photovoltaics" such as perovskites, dye-sensitized, and organic solar cells, have show great potential for high-efficiency thin-film solar cells, as shown in Table 1.1. Among them, perovskite solar cells have achieved remarkable progress with conversion efficiency, from 3.8% in 2009 to 25.2% in 2019 [6]. One of major challenges of perovskites is their poor stability, resulting in the significant degradation of solar cell performance. These emerging

photovoltaics are still in the stage of research and have limited commercial availability.

1.3. Aim and Outline

Among a broad range of novel photovoltaic materials, barium disilicide ($BaSi_2$) has recently gained an increasing interest as a promising light-absorbing material toward high-performance thin-film solar cells [15, 16]. Composed by Si and Ba, $BaSi_2$ shows its inherent advantages of adequate elemental availability (Si and Ba are the 2nd and 14th most abundant element in the Earth's crust, respectively, as shown in Figure 1.6) and nontoxicity. Besides, $BaSi_2$ presents good opto-electronic properties for photovoltaic applications. $BaSi_2$ possesses a band gap E_g = ~1.3 eV, and a high absorption coefficient (α) over 10^4 cm^{-1} at the photon energy of 1.5 eV.[17]. It presents a large minority-carrier lifetime $\tau \approx 14$ µs [18], and a long minority-carrier diffusion length $L \approx 60$ µm [19].

These features allow $BaSi_2$ a promise candidate for the realization of low-cost and high-efficiency thin-film solar cells [18, 20, 21]. Based on computational results, the energy conversion efficiency η of an n-p $BaSi_2$ homojunction solar cell reaches 22.5%, while $BaSi_2$/Si and n-Si/$BaSi_2$/p-Si heterojunction solar cells possess potential η up to 22.7% and 30.4%, respectively [15, 22, 23].

To enable the transition of $BaSi_2$ from a promising material to an efficient thin-film solar cell, there are still many scientific issues and technical challenges that need to be addressed and solved. An industrially applicable $BaSi_2$ thin-film synthesis method and a comprehensive materials characterizations on fabricated films come to the forefront in the development of $BaSi_2$ thin films for photovoltaics.

1.3.1. Aim and scopes

This thesis aims to present fabrications of $BaSi_2$ thin films by the industrially applicable and low-cost sputtering deposition technique and a comprehensive characterization of sputtered $BaSi_2$ thin films. These pieces of knowledge about sputtered $BaSi_2$ can serve as the basis for the development of high-quality $BaSi_2$ films and their further application in thin-film solar cells.

Accordingly, this thesis stems from the following aspects:

1. **Depositions of $BaSi_2$ films by sputtering**. Fabricate $BaSi_2$ films through sputtering, and investigate the effects of deposition conditions on film growth rate and thickness uniformity.

2. **Post-growth annealing treatments**. Facilitate the $BaSi_2$ film crystallization by post-growth annealing treatments. Determine the suitable annealing temperature and duration for $BaSi_2$ crystallization. Characterize the structure and composition of annealed $BaSi_2$ films and their effects on film optical and electrical properties.

3. **Methods to suppress surface oxidation of $BaSi_2$ films**. Develop and employ methods to suppress the surface oxidation of $BaSi_2$ films caused by the exposure to ambient atmosphere and the high-temperature annealing treatment. Investigate their effects on film composition, structure, and properties.

4. **Interface investigations on $BaSi_2$/Si heterostructures**. Fabricate $BaSi_2$/Si heterostructures, and investigate their structure and composition variations during high-temperature annealing treatments. Understand the mechanism of structure and composition variations at $BaSi_2$/Si interfaces.

1.3.2. Thesis outline

Accordingly, this thesis is outlined in the following way:

- **Chapter 1. Introduction**. This chapter gives a general introduction of photovoltaics and thin-film solar cells. The prospects and challenges of thin-film solar cells are discussed.

- **Chapter 2. Barium Disilicide**. A comprehensive review of recent studies on $BaSi_2$ is given, including its crystal and electronic structures, opto-electronic properties, thin-film deposition methods, and recent advancements in $BaSi_2$-based solar cells.

- **Chapter 3. Experimental**. A brief introduction of material deposition methods and characterization techniques applied in this work is provided.

- **Chapter 4. Sputtered $BaSi_2$ Films**. $BaSi_2$ films are deposited by sputtering. Post-growth annealing in N_2 atmosphere is applied for crystallization. Phenomena of surface oxidation and elemental inter-diffusion in sputtered $BaSi_2$ are investigated. A mechanism of oxidation-induced structure transformation is introduced based on the material characterization results.

- **Chapter 5. Vacuum-Annealed $BaSi_2$ Films**. The vacuum condition is applied for annealing of sputtered $BaSi_2$, which can suppress the elemental inter-diffusion in sputtered $BaSi_2$ at the high-temperature condition. The optical and electrical properties of films are analyzed.

- **Chapter 6. Face-to-Face Annealing Method**. A face-to-face annealing method (FTFA), in which two $BaSi_2$ films on the glass substrate are placed together, the film surface to the film surface, is employed to avoid surface oxidation of sputtered $BaSi_2$ films during the high-temperature annealing. The surface composition homogeneity of the sample is investigated by the Raman spectral mapping method. Properties of FTFA annealed samples are measured to understand the effects of the FTFA method. Besides, the heat transfer during the FTFA is studied based on the thermal resistance analysis to investigate the mechanism of the FTFA method.

- **Chapter 7. Investigations on Si/$BaSi_2$/Si Structures**. Si/$BaSi_2$/Si heterostructures are fabricated by sputtering a $BaSi_2$ target and an intrinsic Si target in the same deposition chamber. The surface oxidation of $BaSi_2$ due to the exposure to ambient atmosphere is avoided with the subsequently deposited Si layer on the $BaSi_2$ surface. The influence of Si layer thickness on the composition, structure, and properties of Si/$BaSi_2$/Si heterostructures are systematically investigated and analyzed.

- **Chapter 8. Conclusion**. The chapter summaries the key results of this thesis and gives an outlook for the research on $BaSi_2$ from aspects of material and device development.

1.4. Contribution to the Field

This work contributes to the development of sputtered $BaSi_2$ films from the following aspects:

1. **Fabrications of sputtered $BaSi_2$ films.** This work provides an alternative low-cost route to manufacture $BaSi_2$ films, consisting of the room-temperature sputtering deposition and the post-growth annealing. The industrially applicable magnetron sputtering technique is employed to deposit $BaSi_2$ films at room temperature. Effects of deposition conditions on film growth rate and thickness uniformity are investigated. Post-growth annealing at N_2 atmosphere is applied for the film crystallization. The annealing temperature and duration are optimized for a good crystalline quality of sputtered $BaSi_2$ films. Various methods are used to suppress the surface oxidation of $BaSi_2$ at high-temperature conditions, including vacuum annealing, the face-to-face annealing method, and the Si anti-oxidation layer. The mechanisms and effects of these methods are discussed. This research provides fundamental knowledge for the further material quality improvement of sputtered $BaSi_2$ films.

2. **Characterizations of sputtered $BaSi_2$ films.** In this work, various characterization methods are employed to investigate the material structure, composition, and properties. Auger electron spectroscopy provides elemental composition depth profiles of $BaSi_2$, while Raman spectral mapping yields images of composition, structure, and crystallinity of the $BaSi_2$ surfaces. Besides, techniques such as X-ray diffraction, transmission electron microscopy, are employed to analyze the structure, composition, and phase of sputtered $BaSi_2$ films. These techniques allow systematical and comprehensive investigations on $BaSi_2$ for a deeper understanding of its behaviors at high-temperature conditions, such as elemental inter-diffusion and surface oxidation.

3. **Mechanisms of structure and composition variations at high-temperature conditions.** An oxidation-induced structure transformation mechanism is proposed based on the structure and composition investigations on sputtered $BaSi_2$ films, which demonstrates the elemental diffusion caused by surface oxidation during the high-temperature annealing. Together with the silicide-mediated Si crystallization mechanism, it explains structure and composition variations in $Si/BaSi_2/Si$ heterostructures. These proposed mechanisms provide essential knowledge for the further material quality improvement and solar cell design of sputtered $BaSi_2$.

4. **Development of $BaSi_2$-based solar cells.** The knowledge and results in this thesis provide the basis for the realization of efficient $BaSi_2$-based thin-film solar cells. Investigations of interfacial reactions at $BaSi_2/SiO_x$ and $BaSi_2/Si$ interfaces, surface oxidation due to the exposure to the ambient atmosphere and caused by the

high-temperature conditions, and electrical and optical properties of sputtered $BaSi_2$ films studied in this thesis provides the essential knowledge and information for designing and manufacturing $BaSi_2$ thin-film solar cells.

1

References

[1] H. Ritchie and M. Roser, *Energy,* (2018), https://ourworldindata.org/energy.

[2] H. Ritchie and M. Roser, *CO_2 and greenhouse gas emissions,* (2017), https://ourworldindata.org/co2-and-other-greenhouse-gas-emissions.

[3] H. Ritchie and M. Roser, *Renewable energy,* (2019), https://ourworldindata.org/renewable-energy.

[4] F. Enrichi and G. Righini, *Solar Cells and Light Management: Materials, Strategies and Sustainability* (Elsevier, 2019).

[5] M. O. Reese, S. Glynn, M. D. Kempe, D. L. McGott, M. S. Dabney, T. M. Barnes, S. Booth, D. Feldman, and N. M. Haegel, *Increasing markets and decreasing package weight for high-specific-power photovoltaics,* Nature Energy **3**, 1002 (2018).

[6] M. A. Green, E. D. Dunlop, J. Hohl-Ebinger, M. Yoshita, N. Kopidakis, and X. Hao, *Solar cell efficiency tables (version 56),* Progress in Photovoltaics: Research and Applications **28**, 629 (2020).

[7] T. Matsui, A. Bidiville, K. Maejima, H. Sai, T. Koida, T. Suezaki, M. Matsumoto, K. Saito, I. Yoshida, and M. Kondo, *High-efficiency amorphous silicon solar cells: impact of deposition rate on metastability,* Applied Physics Letters **106**, 053901 (2015).

[8] H. Sai, T. Matsui, H. Kumagai, and K. Matsubara, *Thin-film microcrystalline silicon solar cells: 11.9% efficiency and beyond,* Applied Physics Express **11**, 022301 (2018).

[9] M. Nakamura, K. Yamaguchi, Y. Kimoto, Y. Yasaki, T. Kato, and H. Sugimoto, *Cd-free Cu(In,Ga)(Se,S)$_2$ thin-film solar cell with record efficiency of 23.35%,* IEEE Journal of Photovoltaics **9**, 1863 (2019).

[10] First Solar, *First solar achieves yet another cell conversion efficiency world record,* (2016), https://www.businesswire.com/news/home/20160223005315/en/.

[11] E. H. Jung, N. J. Jeon, E. Y. Park, C. S. Moon, T. J. Shin, T.-Y. Yang, J. H. Noh, and J. Seo, *Efficient, stable and scalable perovskite solar cells using poly (3-hexylthiophene),* Nature **567**, 511 (2019).

[12] H. Jiang, Y. Ren, W. Zhang, Y. Wu, E. C. Socie, B. I. Carlsen, J.-E. Moser, H. Tian, S. M. Zakeeruddin, W.-H. Zhu, *et al.*, *Phenanthrene-fused-quinoxaline as a key building block for highly efficient and stable sensitizers in copper-electrolyte-based dye-sensitized solar cells,* Angewandte Chemie International Edition **59**, 9324 (2020).

[13] Z. Li, L. Ying, P. Zhu, W. Zhong, N. Li, F. Liu, F. Huang, and Y. Cao, *A generic green solvent concept boosting the power conversion efficiency of all-polymer solar cells to 11%,* Energy & Environmental Science **12**, 157 (2019).

[14] J. B. H. Gordon B. Haxel and G. J. Orris, *Rare earth elements—critical resources for high technology,* (2002), https://pubs.usgs.gov/fs/2002/fs087-02/.

[15] T. Suemasu, *Exploring the possibility of semiconducting $BaSi_2$ for thin-film solar cell applications,* Japanese Journal of Applied Physics **54**, 07JA01 (2015).

[16] T. Suemasu and N. Usami, *Exploring the potential of semiconducting $BaSi_2$ for thin-film solar cell applications,* Journal of Physics D: Applied Physics **50**, 023001 (2016).

[17] K. Toh, T. Saito, and T. Suemasu, *Optical absorption properties of $BaSi_2$ epitaxial films grown on a transparent silicon-on-insulator substrate using molecular beam epitaxy,* Japanese Journal of Applied Physics **50**, 068001 (2011).

[18] K. O. Hara, N. Usami, K. Nakamura, R. Takabe, M. Baba, K. Toko, and T. Suemasu, *Determination of bulk minority-carrier lifetime in $BaSi_2$ earth-abundant absorber films by utilizing a drastic enhancement of carrier lifetime by post-growth annealing,* Applied Physics Express **6**, 2 (2013).

[19] M. Baba, K. Toh, K. Toko, N. Saito, N. Yoshizawa, K. Jiptner, T. Sekiguchi, K. O. Hara, N. Usami, and T. Suemasu, *Investigation of grain boundaries in $BaSi_2$ epitaxial films on Si(111) substrates using transmission electron microscopy and electron-beam-induced current technique,* Journal of Crystal Growth , 75.

[20] R. Takabe, K. O. Hara, M. Baba, W. Du, N. Shimada, K. Toko, N. Usami, and T. Suemasu, *Influence of grain size and surface condition on minority-carrier lifetime in undoped n -$BaSi_2$ on Si(111),* Journal of Applied Physics **115**, 0 (2014).

[21] T. Deng, T. Suemasu, D. Shohonov, I. Samusevich, A. Filonov, D. Migas, and V. Borisenko, *Transport properties of n- and p-type polycrystalline $BaSi_2$,* Thin Solid Films **661**, 7 (2018).

[22] J.-S. Huang, K.-W. Lee, and Y.-H. Tseng, *Analysis of the high conversion efficiencies β-$FeSi_2$ and $BaSi_2$ n-i-p thin film solar cells,* Journal of Nanomaterials **2014**, 1 (2014).

[23] T. Deng, T. Sato, Z. Xu, R. Takabe, S. Yachi, Y. Yamashita, K. Toko, and T. Suemasu, *p-$BaSi_2$/n-Si heterojunction solar cells on Si(001) with conversion efficiency approaching 10%: comparison with Si(111),* Applied Physics Express **11**, 062301 (2018).

2

Barium Disilicide

2.1. Introduction

The potential of $BaSi_2$ for photovoltaic applications stems from its excellent optical and electronic properties, and essentially elemental abundance and non-toxicity. These features allow its application in low-cost, high-efficiency, and environmentally friendly solar cells. In this chapter, structures and properties of $BaSi_2$ are discussed. Recent advancement in material depositions and solar cell development are reviewed.

2.2. Crystal structures

The semiconducting $BaSi_2$ presents an orthorhombic crystal structure with a space group of D_{2h}^{16} – Pnma, which is stable at atmospheric pressure and temperature [1–3]. The crystal structure of $BaSi_2$ is shown in Figure 2.1. Table 2.1 lists the lattice constants (a, b, c) from experimental and computational results. As shown in Figure 2.1a, 8 Ba atoms occupy two inequivalent 4*c* Wyckoff sites, i.e., Ba1 and Ba2, and 16 Si atoms occupy three inequivalent positions at 4*c* and 8*d* Wyckoff sites, namely Si1, Si2, and Si3. Each Si atom is covalently bonded with three neighboring Si atoms forming a silicon tetrahedron cluster ($[Si_4]^{4-}$, ST), as illustrated in Figure 2.1b. In a ST, there are three inequivalent Si positions. Accordingly, Ba1 and Ba2 sites show different local environment, i.e., the coordination polyhedra (CP) at the Ba1 site (CP1) is a 12-face polyhedron with 9 vertices, while that at the Ba2 site (CP2) is a 14-face polyhedron with 11 vertices, as shown in Figure 2.1c and 2.1d, respectively.

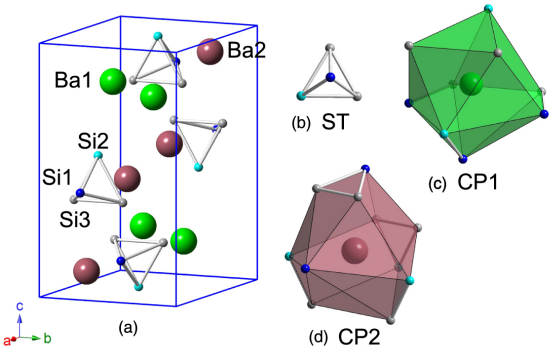

Figure 2.1: (a) Crystal structure of orthorhombic $BaSi_2$. (b) The $[Si_4]^{4-}$ tetrahedron (ST). (c) Coordination polyhedron at the Ba1 site, CP1. (d) Coordination polyhedron at the Ba2 site, CP2. Adapted from Ref. [4]

.

As the crystal structure characteristic of $BaSi_2$, the silicon tetrahedron provides a spectroscopy signature of crystalline $BaSi_2$, e.g., by Raman spectroscopy. The $[Si_4]^{4-}$ anion in $BaSi_2$ exhibits T_h point group symmetry. The vibrational modes of the cluster anion and their Raman (R) or infrared (IR) activities are given by

$$\Gamma(T_h) = A_g(\mathrm{R}) + 2E_g(\mathrm{R}) + 3F_g(\mathrm{R}) + 3F_u(\mathrm{R}), \tag{2.1}$$

where A_g, E_g, and F_g are Raman reactive, while the F_u is IR active. A_g mode corresponds to a symmetric breathing vibration of the tetrahedral cluster, E_g, and F_g is a 2- and 3-fold

Table 2.1: Lattice parameters (a, b, c) of orthorhombic $BaSi_2$.

a [Å]	b [Å]	c [Å]	Method	Ref.
First-principle calculation results				
8.918	6.680	11.451	GGA[a]	[5]
8.790/9.077	6.627/6.786	11.336/11.644	LDA[b]/GGA	[6]
9.224	6.827	11.716	GGA	[7]
8.930	6.752	11.530	HSE06[c]	[8]
Experimental data				
8.942	6.733	11.555		[9]
8.92	6.75	11.57		[3]
8.92	6.80	11.58		[1]

[a] Generalized gradient approximation [10]; [b] Local density approximation [11]; [c] Heyd–Scuseria–Ernzerhof screened hybrid functional method [12].

degenerate symmetric deformation. These modes give rise to the peaks in the Raman spectra of $BaSi_2$, as shown in Table 2.2.

Table 2.2: Raman peak positions originated from $[Si_4]^{4-}$ in $BaSi_2$.

	Raman peak position [cm^{-1}]						Ref.
Mode	A_g	E_g			F_g		
$BaSi_2$/Si(001)[a]	488	295	363	280	358	379	[13]
$BaSi_2$/Si(111)[a]	488	295	364	280	358	379	[13]
$BaSi_2$ powder	486	293	-	276	355	376	[14]
Calculation[b]	486	296	363	282	-	381	[15]

[a] $BaSi_2$ thin films deposited by molecular-beam epitaxy; [b] Phonon density of states (DOS).

2.3. Electronic structures

Figure 2.2 presents the electronic band structure of $BaSi_2$ calculated from density-functional theory DFT HSE06 [16]. It shows that $BaSi_2$ is an indirect band gap semiconductor, of which the valence band maximum (VBM) and conduction band minimum (CBM) are located at different k-points. The calculated fundamental band gap is E_g = 1.25 eV, and the smallest direct band gap is 1.37 eV. These values are in good agreement to experimental results E_g = 1.13 – 1.3 eV [2, 17, 18]. The relatively flat dispersion of the lowest conduction band in Figure 2.2 increases the difficulty in accurate experimental estimation of E_g [16].

The atomically resolved and orbital projected density of states (DOS) is shown in Figure 2.3. The valence band of $BaSi_2$ is dominated by Si-p states, which are derived mainly from the silicon tetrahedron, while the conduction band mainly consists of localized Ba-d states [16]. In agreement with the band structure, the top of the valence band and the bottom of the conduction band exhibit relatively small energy dispersion in the DOS.

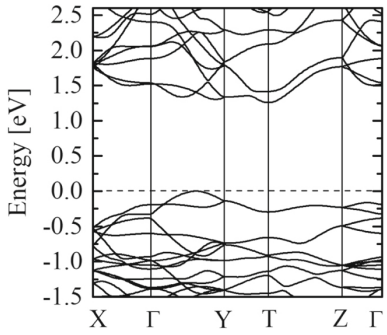

Figure 2.2: Calculated electronic band structure along high-symmetry directions of $BaSi_2$. Adapted from Ref. [16].

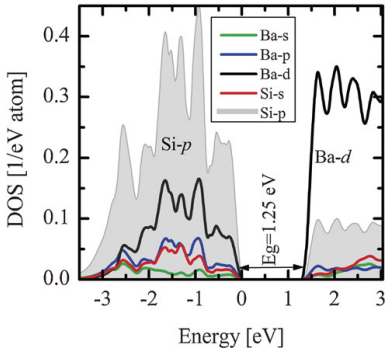

Figure 2.3: Atomically resolved and orbital projected DOS of $BaSi_2$. Adapted from Ref. [16].

Molecular orbital (MO) diagram of $BaSi_2$ is shown in Figure 2.4. The MO diagram is constructed based on the MO diagram of $[Si_4]^{4-}$ and the atomic orbital diagram for Ba^{2+}. The valence bands consist of electronic states derived from the $1e$, $2t_2$, and $2a_1$ orbitals of $[Si_4]^{4-}$, while the conduction bands originate from the $3t_2$ and $1t_1$ orbitals of $[Si_4]^{4-}$, and the $6s$ and $5d$ orbitals of Ba^{2+}. The MO diagram suggests an explanation for the flat conduction and valence band as well as the sharp slope at the band edges of $BaSi_2$. Since $[Si_4]^{4-}$ is a type of molecule, its electronic states are localized, resulting in flat bands, while the Ba $5d$ contributing to the conduction band in general are localized.

2.4. High light absorption

One of the superior performance aspects of $BaSi_2$ is its high optical absorption, which is crucial for realizing economic and efficient solar cells with extremely thin absorber layer. Figure 2.5 shows the calculated absorption coefficient (α) of $BaSi_2$. Despite of the indirect band gap that $BaSi_2$ holds, the high absorption coefficient of $BaSi_2$ is evident. The calculated absorption coefficient at photon energy $h\nu = 1.5$ eV is fairly large, $\alpha = 2.6 \times 10^4$ cm^{-1}, which is in good agreement to the experimentally obtained result $\alpha = 3 \times 10^4$ cm^{-1} [20]. The high optical absorption coefficient of $BaSi_2$ stems from the

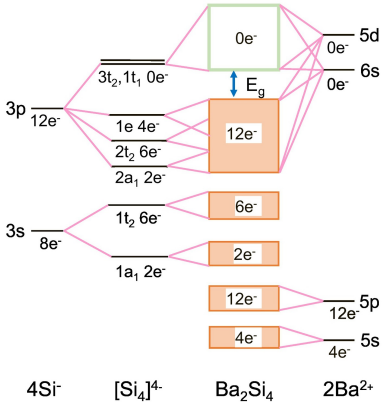

Figure 2.4: Molecular orbital diagram for $BaSi_2$. Adapted from Ref. [19].

large slope at the band edges in its DOS structure, as shown in Figure 2.3. Besides, valence and conduction bands are relatively flat with several local minima and maxima, resulted from its electronic states as discussed in Section 2.3. This leads to a small difference between its fundamental indirect band gap ($E_{g,\,\text{indirect}} = 1.25$ eV) and its direct band gap ($E_{g,\,\text{direct}} = 1.37$ eV) [16]. All these structure features contribute to the high optical absorption of $BaSi_2$.

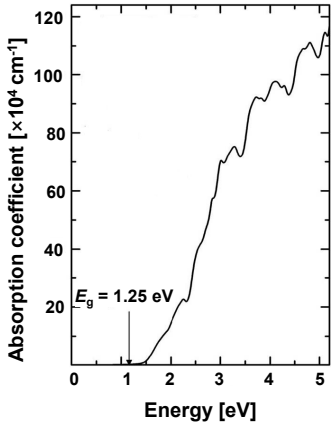

Figure 2.5: Calculated absorption coefficient (α) of $BaSi_2$, reproduced from Ref. [16].

The complex dielectric function represents the optical characteristics of a semiconductor and is given by

$$\varepsilon = \varepsilon_1 + i\varepsilon_2, \tag{2.2}$$

where ε_1 and ε_2 are the real part and the imaginary part, respectively, i is imaginary unit.

The calculated dielectric functions of $BaSi_2$ are presented in Figure 2.6.

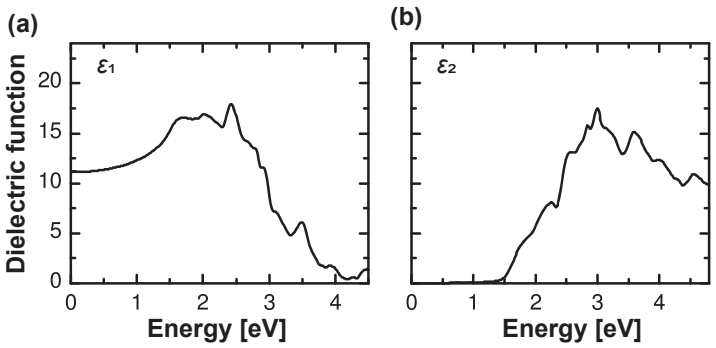

Figure 2.6: Dielectric function of $BaSi_2$, (a) real part ε_1, (b) imaginary part ε_2. Reproduced from Ref. [8].

The complex refractive index ($\tilde{n}$) is given as the square root of ε,

$$\tilde{n} = \sqrt{\varepsilon} = n + i\kappa, \tag{2.3}$$

Here, n denotes the real part of refractive index, and κ denotes the imaginary part of the refractive index or extinction coefficient, which exhibits the relationship with absorption coefficient (α),

$$\alpha = \frac{4\pi\kappa}{\lambda_0}, \tag{2.4}$$

where λ_0 is the wavelength *in vacuo*. Figure 2.7 shows the measured refractive index n and extinction coefficient κ of 150-nm thick epitaxial $BaSi_2$ layer on Si(111).

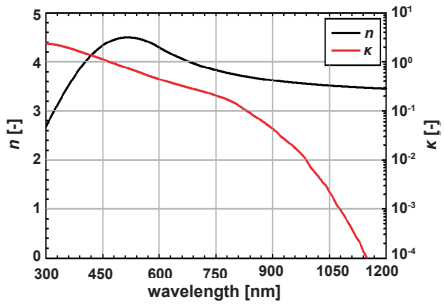

Figure 2.7: Wavelength dependence of refractive index n and extinction coefficient κ of $BaSi_2$.Reproduced from Ref. [21].

2.5. Intrinsic defects and extrinsic doping

The dopability of semiconductor materials plays a decisive role in device architecture design and performance optimization. Dopability refers to the carrier concentration

limits achievable in a semiconductor material. These limits are set by the compensating intrinsic (or native) defects and the solubility of extrinsic dopants. In this section, the intrinsic defects and extrinsic doping of $BaSi_2$ are discussed.

2.5.1. Intrinsic defects

The realistic description of intrinsic defects is based on the defect formation energies as well as their resulting concentrations. The formation energy of intrinsic defect can be given by

$$\Delta H_{D,q} = (E_{D,q} - E_H) + \sum_i n_i \mu_i + qE_F + E_{corr}, \tag{2.5}$$

where $\Delta H_{D,q}$ denotes the formation energy of defect D in charge state q (for a neutrl defect, $q = 0$; if one electron is removed, $q = 1+$; if one electron is added, $q = 1-$, etc), $E_{D,q}$ and E_H are the total energy of the supercells with and without defect, respectively, μ_i is the chemical potentials of different atomic species describing exchange of particles with the respective reservoirs, E_F is the Fermi energy, E_{corr} is the Makov–Payne correction term (essentially the Madelung energy of a lattice of point charges in a dielectric environment) [22, 23]. The concentration of a defect D with charge state q can be obtained by

$$C_{D,q} = N\exp(\frac{-\Delta H_{D,q}}{K_B T}), \tag{2.6}$$

where N is the concentration of the corresponding lattice sites, and k_B is the Boltzmann constant. Accordingly, the charge neutrality condition is given as

$$\sum_D qC_{D,q} - n + p = 0, \tag{2.7}$$

where n and p are the electron and hole concentrations, respectively.

In a defect formation energy *v.s.* Fermi energy diagram, the slope of the line indicates the charge state q, and a kink of the line indicates the thermodynamic transition level $\varepsilon(q_1/q_2)$, which is defined as the Fermi-level position for which the formation energies of charge states q_1 and q_2:

$$\varepsilon(q_1/q_2) = \frac{\Delta H_{D,q_1}(E_F = 0) - \Delta H_{D,q_2}(E_F = 0)}{q_2 - q_1}, \tag{2.8}$$

$\Delta H_{D,q}(E_F = 0)$ is the formation energy of the defect D in the charge state q when the Fermi level is at the VBM ($E_F = 0$). For Fermi-level positions below $\varepsilon(q_1/q_2)$, charge state q_1 is stable, while for Fermi-level positions above $\varepsilon(q_1/q_2)$, charge state q_2 is stable [24].

Figure 2.8 shows the calculated formation energies for the predominant charge states of these native defects under Si-rich (Ba-poor) and Si-poor (Ba-rich) conditions. In general, there majorly are six types of intrinsic defects in $BaSi_2$, namely silicon vacancies (V_{Si}), barium vacancies (V_{Ba}), silicon substituted for barium antisites (Si_{Ba}), barium substituted for silicon antisites (Ba_{Si}), silicon interstitials (Si_i), and barium interstitials (Ba_i).

Si_{Ba} defect shows the highest formation energy, and present the neutral charge state in a large range of Fermi energy, indicating its lower concentration and less contribution to the free carrier generation in the $BaSi_2$. Defects such as Ba_i and V_{Ba} are less stable

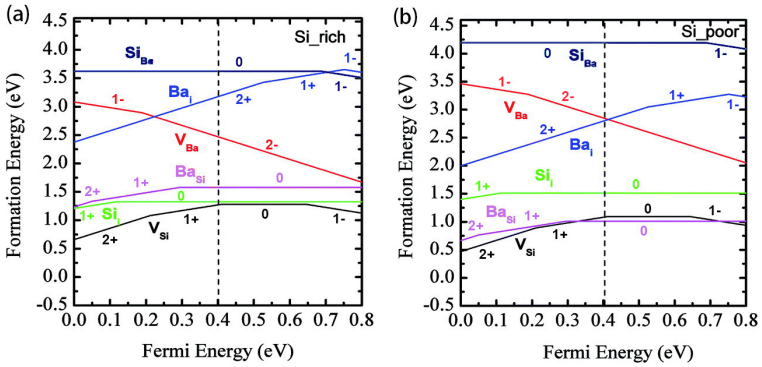

Figure 2.8: Calculated formation energies as a function of the Fermi energy of the intrinsic point defects in $BaSi_2$ under (a) Si-rich and (b) Si-poor conditions. The vertical dashed lines mark the estimated equilibrium Fermi level at T = 600 °C. Reproduced from Ref. [25].

as compared to Si_i, Ba_{Si}, and V_{Si}, suggesting by their higher formation energy. Among these more stable defects, Si_i, Ba_{Si} become charge neutral in a wide range of Fermi energies at the middle of the band gap and are thus not capable of generating carriers. The lower formation energy of Ba_{Si} can be observed under the Si-poor condition, which is understandable given the higher content of Ba.

The silicon vacancy V_{Si}, exhibiting the lowest formation energy in a wide range of Fermi energy, is of great significance in $BaSi_2$ properties. Even in the Si-rich condition, V_{Si} still shows the lowest formation energy, which can be explained by the self-compensation of dangling bonds among the three silicon atoms left in the $[Si_4]^{4-}$ tetrahedron so that less energy is consumed for removing a silicon atom. Both positive (q = 2+ and 1+) and negative (q = 1−) charge state can be observed with V_{Si} defects. This indicates they can act as both donor- and acceptor-like defects within the $BaSi_2$. According to the calculation results from Equation 2.7, the undoped $BaSi_2$ holds electron concentration $n \approx 10^{16} - 10^{17}$ cm^{-3}, which is in good agreement of experimental results $n \approx 5 \times 10^{15} - 2 \times 10^{16}$ cm^{-3} [18, 26, 27]. Research has shown that the chemical potential allowed for stable growth condition of $BaSi_2$ is narrowly ranged, indicating synthesis condition must be well optimized for realizing the stoichiometric phase of $BaSi_2$ [25]. This also suggests that the conductivity type may be altered by varying growth conditions. Indeed, the transition between n-type and p-type conductivity with a hole concentration $p \approx 1 \times 10^{15}$ cm^{-3} has been reported, in which the deposition rate between Ba and Si were adjusted [28].

Besides, experimental techniques have also been employed in the study of intrinsic (native) defects of $BaSi_2$, such as deep-level transient spectroscopy (DLTS) [27, 29, 30], Raman spectroscopy [31], photoluminescence (PL) [32–34], electron paramagnetic resonance (EPR) [35], and positron annihilation spectroscopy (PAS) [36, 37]. Several trap levels were detected by within the undoped epitaxial $BaSi_2$ films by DLTS, i.e., a hole trap level (H1) of 0.27 eV from the VBM with a density around 10^{13} cm^{-3}, electron trap level E1 and E2 located around 0.1 eV and 0.2 eV below the CBM, respectively, which show concentrations approximately 10^{15} cm^{-3} [27, 29]. The hole trap level H1 is supposed to

be caused by V_{Si} defects [29]. The existence of defects such as Ba_{Si}, V_{Si}, and Si_i can be assigned to the origins of some specific PL peaks, and the main Raman peak at around 490 cm^{-1} shifts to a lower wavenumber [31, 32]. Besides, defects are also detected by advanced technology such as EPR and PAS [35–37].

2.5.2. Extrinsic doping

Theoretical calculation has revealed the possibility to achieve both *n*- and *p*-type $BaSi_2$ with the electron concentration n up to 10^{19} cm^{-3}, and the hole concentration p up to 10^{18} cm^{-3} through external doping [25, 38]:

- *p*-type conductivity:
  i. substitute Si with a trivalent element, such as B, Al, Ga, or In;
  ii. substitute Ba with a monovalent element, such as Li, Na, or K.
- *n*-type conductivity:
  i. substitute tetravalent Si with a pentavalent element, such as N, P, As, or Sb;
  ii. substitute divalent Ba with a trivalent element, such as La or Y.

Experimental attempts of doped-$BaSi_2$ have been carried out. Table 2.3 lists the carrier types and concentrations of impurity-doped $BaSi_2$ films. Both *n*- and *p*-type $BaSi_2$ can be achieved, with a large range of carrier concentration. These results pave the path of the development of $BaSi_2$-based solar cell development. It should be mentioned that these experimental attempts are majorly based on molecular-beam epitaxial $BaSi_2$ films, which is not suitable for large-scale and low-cost manufacturing. Efforts are still needed to develop doped-$BaSi_2$ based on other industrially-applicable deposition techniques.

Table 2.3: Carrier type and concentration of impurity-doped $BaSi_2$ films

Carrier type	Dopants	Carrier Concentration [cm^{-3}]	Doping techniques	Post-growth treatments	Ref.
p-type	B	3.4×10^{19} – 6.5×10^{19}	in-situ co-evaporation[a]	RTA[b] at 800 °C	[39, 40]
	In	10^{16} – 10^{17}	in-situ co-evaporation		[41, 42]
	Al	10^{16} – 10^{17}	in-situ co-evaporation		[42, 43]
	Ag	3×10^{16}	in-situ co-evaporation		[42]
n-type	As	4.3×10^{18}	evaporation GaAs		[44]
	As	6.0×10^{19}	ion implantation	annealing at 500 °C	[45]
	P	10^{18}	ion implantation	annealing 500 to 700 °C	[46]
	Li	3×10^{20}	LiF evaporation	RTA at 500 °C	[47]
	Na	3×10^{17} – 4×10^{17}	NaF evaporation	RTA at 500 °C	[47]
	K	3×10^{17} – 4×10^{17}	KF evaporation	RTA at 500 °C	[47]
	Cu	10^{19} – 10^{20}	in-situ co-evaporation		[42, 48, 49]
	Sb	10^{16} – 10^{20}	in-situ co-evaporation		[41, 42]
	Ga	10^{16}	in-situ co-evaporation		[42]

[a] Dopants evaporated with standard Knudsen cells; [b] Rapid thermal annealing.

2.5.3. Surface passivation

The surface represents rather severe defects in the crystal structure and is the site of many allowed states within the forbidden energy gap of semiconductor materials including $BaSi_2$. These facts would lead to intensive surface recombination. To reduce surface

recombination velocities of materials for high-efficiency solar cells, two approaches are hitherto applied:

i. growth of a thin layer of a suitable material onto the semiconductor surface to reduce surface-state density;

ii. creation of a strong built-in electric field (high-low junction) to repel the minority carriers from recombination sites at the surface.

For $BaSi_2$, various surface passivation methods have been applied and studied:

- **Native-oxide passivation.** Owing to the high reactivity with oxygen and moisture, the surface of $BaSi_2$ can be easily oxidized. An around 8-nm-thick native oxide layer on $BaSi_2$ surface can be obtained after being exposed in the air [50]. In fact, the native oxide layer can function as a passivation layer that enhance the Shockley-Read-Hall lifetime (τ_{SRH}) from 0.42 to 8.6 µs [51]. However, the native oxide layer consequently results in a barrier height for minority carrier (hole) around 3.9 eV [50].

- **AlO_x passivation.** The AlO_x passivation layer was prepared by sputtering of Al followed by air oxidation. The unpassivated evaporated $BaSi_2$ holds a minority-carrier lifetime of 2.5 µs. With the AlO_x passivation, the minority-carrier lifetime increases to 6 µs. The annealing treatment can further increase the lifetime to a higher value of 27 µs [52].

- **Amorphous-Si (a-Si) passivation.** The thin layer of a-Si was deposited on the surface of $BaSi_2$ to prevent surface oxidation, which reduces the barrier height to -0.96 eV [53]. It was found that the a-Si layer also acts as the passivation layer, increasing the minority-carrier lifetime up to approximately 10 µs [54]. And a-Si/p-$BaSi_2$(20 nm)/n-Si heterojunction solar cells show efficiency up to 9.9 % [55]. Besides, hydrogenated amorphous Si (a-Si:H) was used for passivation, which was deposited by evaporation with a simultaneous hydrogen plasma treatment [56].

- **Atomic hydrogen passivation.** Hydrogen passivation has been widely used in materials such as Si, diamond, and GaAs, to reduce their defects, which can also be applied for $BaSi_2$. After growth of the $BaSi_2$ film, a subsequently treatment with hydrogen plasma is carried out at a temperature of 580 °C [57, 58]. Hydrogen atoms are considered to occupy V_{Si} and passivate point defects in $BaSi_2$, resulting in a minority-carrier lifetime of 14 µs [57]. By increasing the H-plasma treatment duration, the trap concentration decreases, which is around 2.2×10^{12} cm^{-3} with duration of 15 min [57]. Doped $BaSi_2$ can be passivated by hydrogen plasma. e.g., B-doped $BaSi_2$ [58]. For a B-doped p-$BaSi_2$/n-Si heterojunction solar cells, the atomic H supply significantly decreased the reverse saturation current density and improved the conversion efficiency from 2.59% to 6.20% [58].

2.6. Material synthesis

In 1991, the first $BaSi_2$ thin film was fabricated by molecular-beam epitaxy (MBE) via the surface reaction between barium metal and silicon substrates [59]. In turn of the century, researchers realized the potential of $BaSi_2$ in photovoltaics, triggering a renewed research interest in $BaSi_2$ [17]. Nowadays, thin-film $BaSi_2$ has been produced by techniques including reactive deposition epitaxy (RDE) [60], molecular-beam epitaxy (MBE) [18, 20, 28, 30, 61–69], thermal evaporation (TE) [70–73], sputtering [74–77], pulsed laser deposition (PLD) [78], close-spaced evaporation (CSE) [79], solid-phase epitaxy (SPE)[80], etc. Besides, the vertical Bridgman method was applied for growth of $BaSi_2$ bulk [81], and the chemical-vapor deposition (CVD) achieved the $BaSi_2$ nanowire arrays (NWs) [82]. Table 2.4 lists the fabrication conditions of these methods as well as properties of $BaSi_2$ that they produced.

2.6.1. Molecular-beam epitaxy

Molecular beam epitaxy (MBE) denotes the epitaxial growth of a wide variety of materials, ranging from oxides to semiconductors to metals, by a process involving the reaction of one or more thermal process molecular beams incident upon a heated crystal that has previously been processed to produce a nearly atomically clean surface in an ultra-high vacuum (UHV) environment [83, 84]. The arriving constituent atoms form a crystalline layer in registry with the substrate, namely an epitaxial film. The MBE technique allows the production of a large range of unique structures, benefiting from its precise control of composition during growth. Together with the cleanliness of the growth environment, MBE structures closely approximate the idealized models used in solid-state theory. These features enable the prominent position of MBE in the development and research of new materials, e.g., $BaSi_2$.

Figure 2.9 shows the typical arrangement of an MBE set-up. Substrates are amounted on a heater block enabling high-temperature condition during the film growth. Knudsen cells are always used as evaporation sources, allowing the stabilization of a defined vapor pressure inside the cell by precise temperature control of the heater. Effusion cells are used for chemical compounds using plasma sources for source cracking. The reflection high energy electron diffraction (RHEED) system is used for monitoring the growth of epitaxial films, providing a diffraction pattern as the indicator of film crystallinity.

For the epitaxial growth of $BaSi_2$, crystalline silicon is used as a substrate given the higher lattice match between them. Prior to the epitaxial growth, a thin layer of crystalline $BaSi_2$template is deposited by RDE. Epitaxial films are grown based on the template. The two-step MBE deposition are shown in Figure 2.10, which includes [61]:

i. **Template formation by RDE**. Ba atoms are evaporated by Knudsen cells and arrive at the heated silicon substrate. $BaSi_2$ template is produced by the reaction between the Ba and silicon substrate. The substrate temperature of RDE for template growth is around 500 °C.

ii. **Epitaxial-film growth by MBE**. Si and Ba atoms are co-evaporated during the epitaxial film growth on the $BaSi_2$ template. $BaSi_2$ can be grown over a wide temperature range from 450 – 700 °C [61]. By controlling the deposition-rate ratio between Si and Ba (R_{Si}/R_{Ba}), the properties of deposited $BaSi_2$ can be tuned [28]. Moreover,

Table 2.4: $BaSi_2$ synthesis techniques and properties

Techniques	Deposition conditions			Post-growth annealing	Properties			Remarks	Ref.
	Sources	Substrates	Temperature		Band gap	Majority Carrier	Other		
Thin films									
MBE	Ba	Si(001)	> 840 °C	-	-	-	-	-	[59, 85]
RDE	Ba	Si(111)	600 – 650 °C	-	-	-	[100]-oriented	-	[60]
	Ba, Si	Si(111)	600 °C	-	-	-	[100]-oriented	-	[61]
	Ba, Si	Si(111)	600 °C	-	-	$n = 5 \times 10^{15}$ cm^{-3}	$\mu_e = 820$ cm^2/Vs [b], $\alpha = 10^5$ cm^{-1} [c], when $h\upsilon = 1.5$ eV	$R_{Ba} = 2.0$ nm/min, $R_{Si} = 1.2$ nm/min [d]	[18]
	Ba, Si	Si(111)	600 °C	-	$E_{g,indirect} = 1.23$ eV, $E_{g,direct} = 1.38$ eV [e]	-	-	$R_{Ba} = 3.7$ nm/min, $R_{Si} = 1.6$ nm/min	[62]
MBE (RDE) [a]	Ba, Si	poly-Si/SiO_2 [f]	600 °C	-	-	-	$EQE = 8\%$ (at 1.60 eV, $V_{bias} = 5$ V [g]	-	[63, 64]
	Ba, Si	SOI [h]	575 °C	-	$E_{g,indirect} = 1.34$ eV	-	$\alpha = 3 \times 10^4$ cm^{-1}, when $h\upsilon = 1.5$ eV	-	[20]
	Ba, Si	Si(001), Si(111)	600 °C	-	-	-	$L = 10\,\mu$m [i], grain size 0.1 – 0.3 µm	-	[65]
	Ba, Si	Si(111)	580 °C	$T_{an} = 760$ °C [j]	-	-	grain size 4 µm	$R_{Ba} = 2.0$ nm/min $T_{RDE} = 600$ °C, $t_{RDE} = 60$ min [k]	[66, 67]
	Ba, Si	Si(111)	600 °C	$T_{an} = 800$ °C	-	-	$\tau = 14\,\mu$s [l], $L = 60\,\mu$m	-	[68]
	Ba, Si	Ge(111)	580 °C	-	-	-	-	$BaGe_2$ template (RDE), $BaSi_2$ (SPE)	[69]
	Ba, Si	Si(111)	580 °C	-	-	$p = 1 \times 10^{15}$ cm^{-3} [m]	p-type when $R_{Ba}/R_{Si} = 2.0 – 2.6$, else, n-type conductivity	3 nm a-Si capping layer,	[28]
	Ba, Si	Si(111)	650 °C	-	-	-	-	Three-step growth [n]	[30]
TE	$BaSi_2$	glass, quartz, Si(111)	500 – 600 °C	-	$E_{g,indirect} = 1.14 – 1.21$ eV	-	$\alpha = 2 \times 10^4$ cm^{-1} at 1.5 eV, $\tau = 0.027 – 0.031$ µs,	-	[70, 71]
	$BaSi_2$	Si(111)	550 °C	$T_{an} = 100$, RTA [o]	-	$n = 2 \times 10^7$ cm^{-3}	$\tau = 13$ µs	-	[72]
	$BaSi_2$	a-Si/Ge(100)	500 °C	-	-	-	$\tau = 1.5$ µs	-	[73]
	Ba	Si (111)	RT [p]	$T_{an} = 400 – 800$ °C	-	-	poly-crystalline	-	[74]
Sputtering	$BaSi_2$	glass	500 – 600 °C	-	$E_{g,indirect} = 1.25$ eV	-	$n_{refractive} \approx 4.0$ for long wavelengths [q], deposition rate 33.3 nm/min	-	[75]
	$BaSi_2$	Si(111), Si_3N_4/Si	500 – 600 °C	$T_{an} = 600 – 700$ °C	-	$n = 5 \times 10^{19}$ cm^{-3}	$\tau_e = 20$ cm^2/Vs [r], grain size 10 – 20 nm	-	[76]
	$BaSi_2$ + Ba	Si(111), CaF_2	600 °C	-	-	$n = 2 \times 10^{16}$ cm^{-3}	photoresponsivity = 0.19 A/W (at 2.0 eV, $V_{bias} = -0.4$ V)	-	[77]
PLD	$BaSi_2$	SiO_2, CaF_2 (111), Si/SiO_2	-	-	$E_{g,indirect} = 1.32$ eV	-	$\alpha > 10^5$ cm^{-1} ($h\upsilon > 1.6$ eV)	-	[78]
CSE	$BaAl_4$, Ni	Si(001)	900 – 1000 °C	-	-	-	-	$BaAl_4 + 4Ni = 4NiAl + Ba$(g)	[79]
SPE	Ba, Si	Si(111)	RT	Two-stage annealing: 600 and 800 °C	-	-	$\alpha > 1 \times 10^4$ cm^{-1}	-	[80]
Bulk									
Vertical Bridgman	Ba, Si	-	> melting point [s]	-	-	-	-	(at.%Ba) / (at.%Si) = 50/50 – 24/76	[81]
Nanowire arrays (NWs)									
CVD	Ba	Si NWs	930 °C	-	$E_{g,indirect} = 1.27$ eV, $E_{g,direct} = 1.06$ eV	-	-	-	[82]

[a] MBE with RDE template; [b] Electron mobility, μ_{rme}; [c] Absorption coefficient, α; [d] Si deposition rate R_{Ba}/R_{Si}, Ba deposition rate R_{Ba}/R_{Ba}; [e] Indirect band gap $E_{g,indirect}$, direct band gap $E_{g,direct}$; [f] Poly-Si prepared by Al-induced crystallization; [g] External quantum efficiency EQE, bias voltage V_{bias}; [h] Silicon on insulator, SOI; [i] Minority carrier diffusion length, L; [j] Annealing temperature, T_{an}; [k] RDE deposition temperature T_{RDE}, duration t_{RDE}; [l] Minority carrier life time, τ; [m] When $R_{Ba}/R_{Si} = 2.2$; [n] i) RDE, ii) Ba-rich deposition, and iii) Si-rich deposition; [o] Rapid thermal annealing, RTA; [p] Room temperature, RT; [q] Refractive index $n_{refractive}$; [r] Electron mobility, μ_e; [s] 20 – 100 K above the compound melting point.

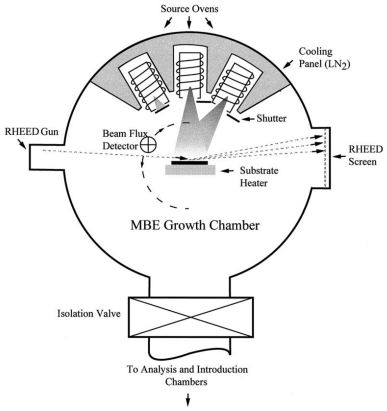

Figure 2.9: Schematic drawing of a simple MBE chamber. Adapted from Ref. [84].

the employment of multi-stage deposition, e.g., a Ba-rich deposition followed by a Si-rich deposition, can further improve the epitaxial film quality [30].

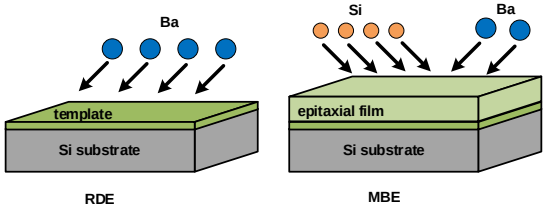

Figure 2.10: Schematic illustration of a typical MBE deposition process of $BaSi_2$.

The preparation of high-quality epitaxial thin films requires a carefully controlled layer-by-layer growth process. Hence, a precise low-rate deposition with controlled evaporation rates is highly preferred for MBE. The deposition rate of epitaxial $BaSi_2$ film is approximately 1 nm/min [86]. Besides, UHV is required for MBE to avoid the disturbing influence of residual gas impurities. These features enable MBE to serve as an excellent research platform for $BaSi_2$, somehow, narrow its implementation in the low-cost and large-scale production of $BaSi_2$ films.

2.6.2. Thermal evaporation

Thermal evaporation, a practical approach for large-scale and high-deposition-rate thin-film fabrication, has also been applied for the fabrication of $BaSi_2$ films. The thermal evaporation system is rather simple as compared to the MBE. A typical thermal evaporation system consists of a deposition chamber and heating sources. The operation pressure of evaporation is normally in the range of 10^{-3} – 10^{-4} Pa.

Figure 2.11 depicts the process of thermal evaporation for $BaSi_2$ thin films. $BaSi_2$ granules are used as the evaporation source which is placed in a heated tungsten boat. The Ba and Si vapors are formed from the decomposition of $BaSi_2$ at high temperatures.

Ba and Si atoms arrive at the heated substrate and form $BaSi_2$ layer. The substrate temperature is around 600 °C [70]. Various substrates can be used for evaporated $BaSi_2$, such as glass and silicon [70]. The deposition rate of thermal evaporation is quite large, ranging from 64 – 2800 nm/min [87].

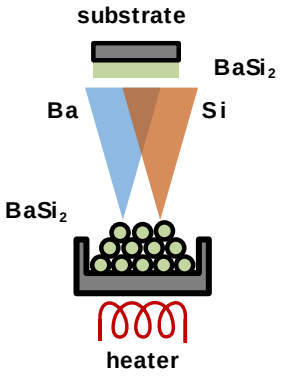

Figure 2.11: Schematic illustration of a typical thermal evaporation deposition process of $BaSi_2$.

Evaporated $BaSi_2$ films show a multi-phase composition and their quality that is inferior to that of the epitaxial films [70–73, 87]. Reactions between the $BaSi_2$ and the tungsten boat can vary the ratio between the Ba and Si vapor flux [70]. To obtain stoichiometric $BaSi_2$, the evaporation condition such as deposition rate and substrate temperature needs to be carefully adjusted. Rather than using $BaSi_2$ granule evaporation sources, co-evaporation of Ba and Si can contribute to stoichiometric control over evaporated films.

2.6.3. Sputtering

Sputtering is another widely used physical vapor deposition (PVD) technique for thin-film fabrications. The detailed information about the sputtering system and mechanism introduction is given in Section 3.1.1.

To obtain sputtered $BaSi_2$ films, either a Ba target or a $BaSi_2$ is used for sputtering. Silicon wafer substrates are required when using the Ba target. And after the sputtering at room temperature, the Ba/c-Si samples need to be annealing at around 800 °C for the formation of $BaSi_2$ crystals [74]. On the contrary, sputtering of stoichiometric $BaSi_2$ has no the specific requirement on substrate type, which enables depositions on substrates of glass and wafer. The sputtering can be executed either at high temperatures or at room temperature yet with subsequent annealing [75–77]. The deposition rate is adjustable by controlling the pressure and plasma power during depositions, which is around a-few-nanometer per minute [77].

The sputtered $BaSi_2$ films are poly-crystalline and show higher majority carrier (electron) concentration in the scale of 10^{19} cm^{-3}, which may be related to the existence of impurities and defects [76]. Indeed, the film quality of sputtered $BaSi_2$ still needs to be improved for photovoltaic applications.

2.6.4. Potential alternative techniques

As shown in Table 2.4, other thin-film deposition techniques, such as PLD, CSE, and SPE, have been employed for $BaSi_2$ thin-film synthesis, whereas research on these methods are limited. Here, we make some brief introductions on these methods:

- **Pulsed laser deposition (PLD)**. Ba and Si are vaporized from a stoichiometric $BaSi_2$ target by a high-power pulsed laser beam, which deposits as a thin film on a heated substrate. SiO_2 and CaF_2 were used as substrates. Poly-crystalline $BaSi_2$ thin films are obtained. [78]

- **Close-spaced evaporation (CSE)**. $BaAl_4$ and Ni powders are placed on a set of two Si wafers (one of them acting as the substrate), which is around 2 mm and forms the so-called close space. The Ba vapor is produced by reaction between $BaAl_4$ and Ni in high temperatures, which forms the $BaSi_2$ thin film on the heat Si wafer substrate.[79]

- **Solid-phase epitaxy (SPE)**. Ba and Si are co-evaporated on the Si substrate, which is similar to MBE yet is carried out at a room temperature. After depositions, samples are treated by two-step annealing at 600 °C and 800 °C to obtain poly-crystalline $BaSi_2$ films.[80]

2.7. Solar cell developments

Along with the development of thin-film fabrication methods, researches on $BaSi_2$-based solar cells have been carried out, including theoretical computations and experimental attempts. In this section, a brief review of recent advances in the development of $BaSi_2$-based solar cells is given.

Indeed, theoretical studies have exhibited the great promise of $BaSi_2$ to achieve high-efficient solar cell applications. Various structures of solar cells have been proposed, as listed in Table 2.5. A $BaSi_2$-based homojunction solar cell can reach an efficiency around 22.5% [88], while an n-i-p the heterojunction structure can achieve extremely high efficiency around 30.4% [89]. These proposed structures guide practical attempts to achieve these attractive efficiencies.

Here, the experimental attempts on $BaSi_2$-based are introduced in detail. Currently, investigations on structures, including Schottky barrier solar cells, n-p heterojunction solar cells, and homojunction solar cells, have been reported, which provides the fundamental for the development of high-efficient $BaSi_2$ solar cells.

2.7.1. Schottky-barrier solar cells

A Schottky barrier (SB) formed by a metal/n-(p-)type semiconductor has long been considered as the simplest photovoltaic devices of all. The simplicity of the structure of a Schottky-barrier cell makes it a good starting point for solar cell development. The Schottky cell exhibits optimal performance when one contact is ohmic while the other is the barrier contact.

Accordingly, Schottky-barrier solar cells has been reported, with a structure of Al-doped ZnO(AZO)/Si_3N_4/$BaSi_2$/Al-Nd [94]. The $BaSi_2$ layer is deposited by sputtering followed by annealing at 500 °C. In fact, this solar cell presents extremely low efficiency,

Table 2.5: Theoretical calculation results of $BaSi_2$-based solar cells performance.

Structures	V_{OC}[V]	J_{SC} [mA/cm^2]	FF [%]	η [%]	Ref.
n-Si/i-$BaSi_2$/p-Si	0.594	22.93	82.63	30.4	[89]
Zn_3P_2/n-$BaSi_2$ [a]	0.800	33.66	85.99	23.17	[90]
n^+-Si/p-$BaSi_2$ [b]	-	-	-	14.2	[88]
p^+-Si/n-$BaSi_2$ [c]	-	-	-	22.7	[88]
n^+-$BaSi_2$/p-$BaSi_2$ [d]	-	-	-	22.5	[88]
p^+-$BaSi_2$/n-$BaSi_2$ [e]	-	-	-	22.5	[88]
p-$BaSi_2$/n-$BaSi_2$ [f]	0.83	30.61	86	21.74	[91]
p-$BaSi_2$/i-$BaSi_2$/n-$BaSi_2$ [g]	0.87	32.09	87	24.22	[91]
Al/FTO/CdS/CIGS/$BaSi_2$/Mo [h]	0.843	40.56	76.76	26.24	[92]
Al/FTO/CdS/p-$BaSi_2$/Cu [i]	1.065	34.23	72.14	26.32	[93]

[a] Concentration of acceptor $N_A = 10^{19}$ cm^{-3}, concentration of donor $N_D = 10^{16}$ cm^{-3}; [b] Thickness of n^+−Si $d_{n^+-Si} = 0.1$ µm, $N_D = 10^{19}$ cm^{-3}, $d_{p-BaSi_2} = 2$ µm, $N_A = 10^{17}$ cm^{-3}; [c] $d_{p^+-Si} = 0.1$ µm, $N_A = 5\times10^{19}$ cm^{-3}, $d_{n-BaSi_2} = 2$ µm, $N_D = 10^{18}$ cm^{-3}; [d] $d_{n^+--BaSi_2} = 5$ nm, $N_D = 5\times10^{19}$ cm^{-3}, $d_{p-BaSi_2} = 2$ µm, $N_A = 10^{17}$ cm^{-3}; [e] $d_{p^+-BaSi_2} = 5$ nm, $N_A = 5\times10^{19}$ cm^{-3}, $d_{n-BaSi_2} = 2$ µm, $N_D = 10^{17}$ cm^{-3}; [f] $d_{n-BaSi_2} = 10$ nm, $N_D = 5\times10^{19}$ cm^{-3}, $d_{p-BaSi_2} = 2$ µm, $N_A = 1\times10^{17}$ cm^{-3}; [g] $d_{n-BaSi_2} = 10$ nm, $N_D = 5\times10^{19}$ cm^{-3}, $d_{i-BaSi_2} = 2$ µm, $d_{p-BaSi_2} = 120$ nm, $N_A = 5\times10^{19}$ cm^{-3}; [h] $d_{FTO} = 0.05$ µm, $d_{CdS} = 0.05$ µm, $d_{CIGS} = 0.8$ µm, $d_{BaSi_2} = 0.3$ µm; [i] $d_{BaSi_2} = 1.2$ µm, $N_A = 10^{19}$ cm^{-3}, $d_{CdS} = 60$ nm, $N_D = 10^{17}$ cm^{-3}.

i.e., 0.10% at room temperature and 0.68% at 90 K [94]. This can result from the poor quality of sputtered $BaSi_2$ as well as the selection of metal (or TCO) electrodes.

Figure 2.12 shows the band diagrams of structures using p- and n-$BaSi_2$. In the case of p-$BaSi_2$, the contact between p-$BaSi_2$ and Al-Nd is ohmic. AZO/Si_3N_4/p-$BaSi_2$ forms a metal-insulator-semiconductor Schottky-barrier structure. The built-in potential barrier is around $V_{bi} = 0.02$ V, indicating a narrow depletion region. This results in a small photocurrent. As shown in Figure 2.12b, both AZO/Si_3N_4/n-$BaSi_2$ and n-$BaSi_2$/Al-Nd form Schottky-barrier junction, which hold V_{bi} of 1.3 V and 1.0 V, respectively [94]. This structure fails to collect charges effectively.

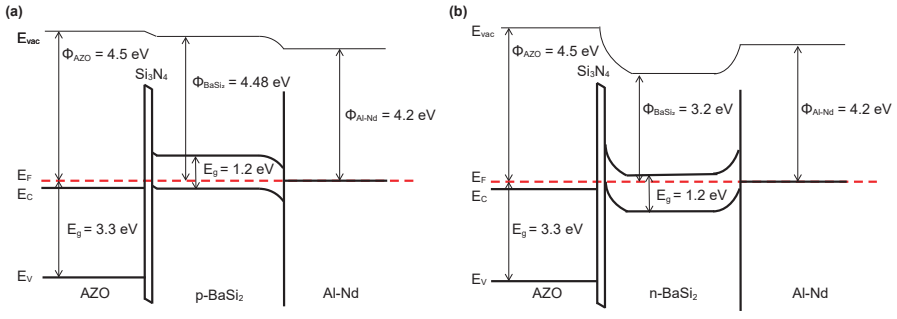

Figure 2.12: Schematic energy band diagrams of (a) AZO/Si_3N_4/p-$BaSi_2$/Al-Nd and (b) AZO/Si_3N_4/n-$BaSi_2$/Al-Nd structures. Reproduced from Ref. [94].

Researchers have pointed out the possibility of $CoSi_2$ acting as the metal in the Schottky-barrier junction [95, 96]. $CoSi_2$ is a metallic silicide, with a work function of approximately 4.7 eV [97]. Given the electron affinity of $BaSi_2$ around 3.2 eV [98], a Schottky-barrier height as large as 1.5 eV is expected for the $CoSi_2$/n-$BaSi_2$ junction. This large barrier height allows a large open-circuit voltage and efficient photogenerated carriers collection in the Schottky-barrier solar cells. A $BaSi_2$ (240 nm)/$CoSi_2$ (27 nm) Schottky-barrier structure has been epitaxially fabricated on Si(111) by MBE [95], which shows clear rectifying properties owing to Schottky-barrier junction at room temperature. It needs to be mentioned that the film quality of $BaSi_2$ is critically dependent upon the surface condition of $CoSi_2$ layer [96].

Besides, Cr/n-$BaSi_2$ Schottky-barrier junction also shows clear rectifying properties in the J-V characteristics at room temperature [26]. The Schottky-barrier junction exhibits a barrier height of 0.73 eV and V_{bi} = 0.53 V. Further research is still needed for the achievement of efficient $BaSi_2$-based Schottky-barrier solar cells.

2.7.2. Heterojunction solar cells

$BaSi_2$-based heterojunction solar cells have attracted more research interest. Heterojunction structures, such as MoO_x/$BaSi_2$ [99], SnS/$BaSi_2$ [100, 101], and Si/$BaSi_2$, have been studied and demonstrate their potential for solar cell development.

Transition metal oxides (TMOs) have been extensively studied for solar cells applications, due to their large band gap and selective carrier collection properties [102]. Among them, MoO_x has shown its ability to selectively extract holes from silicon [103]. Considering the small electron affinity of $BaSi_2$, a MoO_x/n-$BaSi_2$ hetero-structure has been proposed, where MoO_x acts as the hole transport layer [99]. An ITO/MoO_x/n-$BaSi_2$ heterojunction diode is fabricated, in which the MoO_x was deposited by thermal evaporation, and the n-$BaSi_2$ was deposited by MBE. The structure exhibits V_{OC} = 200 mV and J_{SC} = 0.5 mA/cm^2 under AM1.5 illumination, which are still far away from an efficient solar cells.

The SnS/$BaSi_2$ heterojunction has also been studied [100, 101]. SnS and $BaSi_2$ were deposited by thermal evaporation. The hetero-structure was fabricated on the n-Si(100) substrate. The junction was formed by depositions of both SnS and $BaSi_2$ at the low-temperature (150 °C) followed by post-annealing at 400 °C for 10 min [100]. Extremely small V_{OC} of 2 – 3 mV and J_{SC} of 0.012 – 0.025 mA/cm^2 were observed [101]. These low performances can result from the inter-diffusion and reactions at the SnS/$BaSi_2$ interface [100, 101].

As compared to the above-mentioned structures, Si/$BaSi_2$ heterojunctions have attracted more research attention, given the good lattice match between $BaSi_2$ and Si and the fact that high-quality $BaSi_2$ films deposited by MBE are always on the silicon substrates.

Figure 2.13 exhibits the band diagrams of p-Si/n-$BaSi_2$ and n-Si/p-$BaSi_2$ heterojunctions. Due to the different band gap between $BaSi_2$ (1.3 eV) and Si (1.1 eV), obvious band offsets are observed in both two heterojunctions. At the p-Si/n-$BaSi_2$ hetero-interface, the conduction band offset is $\Delta E_C \approx 0.9$ eV, and the valence band offset is $\Delta E_V \approx 0.7$ eV, which are predicted from electron affinities of $BaSi_2$ and Si. Obviously, the band offsets block the photocurrent flowing across the p-Si/n-$BaSi_2$ hetero-interface. To overcome

this issue, a n^+-$BaSi_2$/p^+-Si tunnel junction has been suggested [104, 105].

On the other hand, band offsets ΔE_C and ΔE_V at n-Si/p-$BaSi_2$, as shown in Figure 2.13b, promote the separation of photogenerated electrons and holes in p-$BaSi_2$, as well as those in n-Si, which leads to the operation of a solar cell [54]. By applying an a-Si passivation layer (also to avoid surface oxidation), an efficiency η = 9.9% is achieved by a n-Si/p-$BaSi_2$ (20 nm)/a-Si (3 nm) heterojunction solar cell [106]. It needs to be mentioned that n-Si wafer instead of $BaSi_2$ acts as absorber, which fails to take the best advantages of $BaSi_2$.

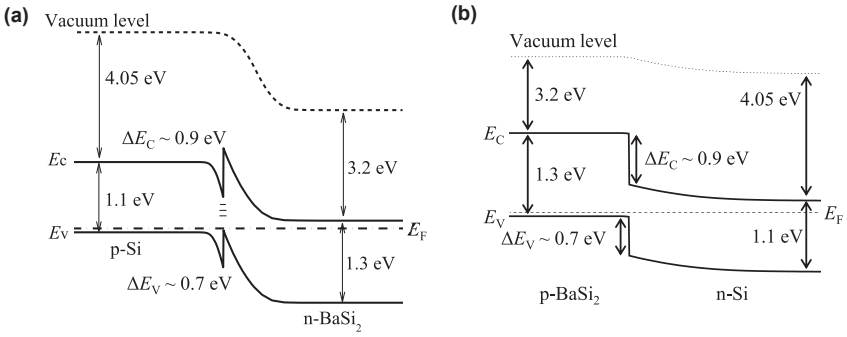

Figure 2.13: Schematic energy band diagrams of (a) p-Si/n-$BaSi_2$ heterojunction, adapted from Ref. [26], and (b) n-Si/p-$BaSi_2$ heterojunction, adapted from Ref. [54].

2.7.3. Homojunction solar cells

The potential of n-$BaSi_2$/p-$BaSi_2$ homojunction solar cells has been studied with a n^+-$BaSi_2$ (20 nm)/p-$BaSi_2$ (500 nm)/p^+-$BaSi_2$ (50 nm) homojunction diode on a heavily doped p^+-Si(111) substrate [107, 108]. The band diagram of this structure is presented in Figure 2.14. Band offsets at p-$BaSi_2$/p-Si interface can be observed. The homojunction solar cell n^+-$BaSi_2$/p-$BaSi_2$/p^+-$BaSi_2$ on the p-Si substrate exhibits η = 0.28%, V_{OC} = 0.11 V, and J_{SC} = 9.4 mA/cm^{-2} [108]. Indeed, efforts are still needed to achieve efficient $BaSi_2$ homojunction solar cells.

2.7.4. Multi-junction solar cells

In addition to the single-junction solar cells, $BaSi_2$-based multi-junction (tandem) solar cells have been proposed. A double-junction solar cell based on organometallic halide perovskite ($CH_3NH_3PbI_3$) as the top absorber and $BaSi_2$ as the bottom absorber has been proposed [21]. The resulting modelled ultra-thin double-junction $CH_3NH_3PbI_3$/$BaSi_2$ (< 2 µm) exhibits an implied total photo-current density equal to 38.65 mA/cm^2 (19.84 mA/cm^2 top cell, 18.81 mA/cm^2 bottom cell) and conversion efficiencies up to 28% [21]. Besides, the possibility of $BaSi_2$/c-Si tandem solar cells have been studied, targeting η > 30% [107].

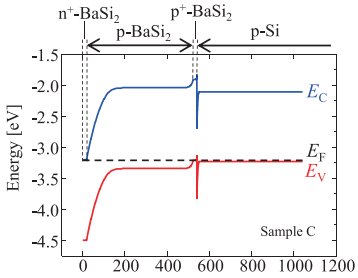

Figure 2.14: Schematic energy band diagrams of n-$BaSi_2$ / p-$BaSi_2$ homojunction on p-Si substrate, adapted from Ref. [108].

2.8. Conclusions

In this chapter, structures, properties, thin-film fabrication methods, and solar cell development of $BaSi_2$ have been discussed. Composed of earth-abundant and low-cost elements, $BaSi_2$ has demonstrated its good optical and electrical properties for thin-film solar cell applications. Towards the goal of high-efficiency $BaSi_2$ based solar cells, there still are plenty of work shall be done with the material development in aspects of material fabrications, characterizations, and solar cell development. Industrially applicable and low-cost material synthesis routines and the deeper understanding on material properties have been attributed to a prominent position in $BaSi_2$ development.

References

[1] H. Schäfer, K. H. Janzon, and A. Weiss, *$BaSi_2$, a phase with discrete Si_4 tetrahedra,* Angewandte Chemie International Edition in English **2**, 393 (1963).

[2] J. Evers and A. Weiss, *Electrical properties of alkaline earth disilicides and digermanides,* Materials Research Bulletin **9**, 549 (1974).

[3] J. Evers, G. Oehlinger, and A. Weiss, *Crystal structure of barium disilicide at high pressures,* Angewandte Chemie International Edition in English **16**, 659 (1977).

[4] M. Kumar, N. Umezawa, and M. Imai, *Recent advances in computational studies of thin-film solar cell material $BaSi_2$,* Japanese Journal of Applied Physics **59**, SF0803 (2020).

[5] H. Peng, C. Wang, J. Li, R. Zhang, M. Wang, H. Wang, Y. Sun, and M. Sheng, *Lattice dynamic properties of $BaSi_2$ and $BaGe_2$ from first principle calculations,* Physics Letters, Section A: General, Atomic and Solid State **374**, 3797 (2010).

[6] D. B. Migas, V. L. Shaposhnikov, and V. E. Borisenko, *Isostructural $BaSi_2$, $BaGe_2$ and $SrGe_2$: electronic and optical properties,* Physica Status Solidi **244**, 2611 (2007).

[7] J.-T. Wang, C. Chen, and Y. Kawazoe, *Phase stability and transition of $BaSi_2$-type disilicides and digermanides,* Physical Review B **91**, 054107 (2015).

[8] M. Kumar, N. Umezawa, and M. Imai, *$(Sr,Ba)(Si,Ge)_2$ for thin-film solar-cell applications: First-principles study,* Journal of Applied Physics **115**, 0 (2014).

[9] J. Evers, *Transformation of three-connected silicon in $BaSi_2$,* Journal of Solid State Chemistry **32**, 77 (1980).

[10] J. P. Perdew and Y. Wang, *Accurate and simple analytic representation of the electron-gas correlation energy,* Physical review B **45**, 13244 (1992).

[11] J. P. Perdew and A. Zunger, *Self-interaction correction to density-functional approximations for many-electron systems,* Physical Review B **23**, 5048 (1981).

[12] J. Heyd, G. E. Scuseria, and M. Ernzerhof, *Hybrid functionals based on a screened coulomb potential,* The Journal of Chemical Physics **118**, 8207 (2003).

[13] H. Hoshida, N. Murakoso, T. Suemasu, and Y. Terai, *Identification of vibrational modes in $BaSi_2$ epitaxial films by infrared and Raman spectroscopy,* in *Defect and Diffusion Forum*, Vol. 386 (Trans Tech Publ, 2018) pp. 43–47.

[14] M. Somer, *Vibrational spectra of the cluster anions $[E_4]^{4-}$ in Themetallic Sodium and Barium Compounds Na_4E_4 and Ba_2E_4 (E = Si, Ge),* Zeitschrift für anorganische und allgemeine Chemie **626**, 2478 (2000).

[15] H. Peng, C. Wang, J. Li, R. Zhang, M. Wang, H. Wang, Y. Sun, and M. Sheng, *Lattice dynamic properties of $BaSi_2$ and $BaGe_2$ from first principle calculations,* Physics Letters A **374**, 3797 (2010).

[16] M. Kumar, N. Umezawa, and M. Imai, *$BaSi_2$ as a promising low-cost, earth-abundant material with large optical activity for thin-film solar cells: A hybrid density functional study,* Applied Physics Express **7**, 071203 (2014).

[17] T. Nakamura, T. Suemasu, K.-i. Takakura, F. Hasegawa, A. Wakahara, and M. Imai, *Investigation of the energy band structure of orthorhombic $BaSi_2$ by optical and electrical measurements and theoretical calculations,* Applied Physics Letters **81**, 1032 (2002).

[18] K. Morita, Y. Inomata, and T. Suemasu, *Optical and electrical properties of semiconducting $BaSi_2$ thin films on Si substrates grown by molecular beam epitaxy,* Thin Solid Films **508**, 363 (2006).

[19] M. Imai, M. Kumar, and N. Umezawa, *Electronic states of Zintl-phase solar-cell material $BaSi_2$,* Scripta Materialia **172**, 43 (2019).

[20] K. Toh, T. Saito, and T. Suemasu, *Optical absorption properties of $BaSi_2$ epitaxial films grown on a transparent silicon-on-insulator substrate using molecular beam epitaxy,* Japanese Journal of Applied Physics **50**, 068001 (2011).

[21] R. Vismara, O. Isabella, and M. Zeman, *Organometallic halide perovskite/barium di-silicide thin-film double-junction solar cells,* in *Photonics for Solar Energy Systems VI*, Vol. 9898, edited by R. B. Wehrspohn and A. Gombert, International Society for Optics and Photonics (SPIE, 2016) pp. 54 – 62.

[22] S. Lany and A. Zunger, *Accurate prediction of defect properties in density functional supercell calculations,* Modelling and simulation in materials science and engineering **17**, 084002 (2009).

[23] C. G. Van de Walle and J. Neugebauer, *First-principles calculations for defects and impurities: Applications to III-nitrides,* Journal of Applied Physics **95**, 3851 (2004), https://doi.org/10.1063/1.1682673 .

[24] C. Freysoldt, B. Grabowski, T. Hickel, J. Neugebauer, G. Kresse, A. Janotti, and C. G. Van de Walle, *First-principles calculations for point defects in solids,* Rev. Mod. Phys. **86**, 253 (2014).

[25] M. Kumar, N. Umezawa, W. Zhou, and M. Imai, *Barium disilicide as a promising thin-film photovoltaic absorber: Structural, electronic, and defect properties,* Journal of Materials Chemistry A **5**, 25293 (2017).

[26] W. Du, M. Baba, K. Toko, K. O. Hara, K. Watanabe, T. Sekiguchi, N. Usami, and T. Suemasu, *Analysis of the electrical properties of Cr/n-$BaSi_2$ Schottky junction and n-$BaSi_2$/p-Si heterojunction diodes for solar cell applications,* Journal of Applied Physics **115**, 223701 (2014).

[27] H. Takeuchi, W. Du, M. Baba, R. Takabe, K. Toko, and T. Suemasu, *Characterization of defect levels in undoped n-$BaSi_2$ epitaxial films on Si(111) by deep-level transient spectroscopy,* Japanese Journal of Applied Physics **54** (2015), 10.7567/JJAP.54.07JE01.

[28] R. Takabe, T. Deng, K. Kodama, Y. Yamashita, T. Sato, K. Toko, and T. Suemasu, *Impact of Ba to Si deposition rate ratios during molecular beam epitaxy on carrier concentration and spectral response of $BaSi_2$ epitaxial films,* J. Appl. Phys. **123**, 2 (2018).

[29] Y. Yamashita, T. Sato, M. E. Bayu, K. Toko, and T. Suemasu, *Investigation of electrically active defects in undoped $BaSi_2$ light absorber layers using deep-level transient spectroscopy,* Japanese Journal of Applied Physics **57**, 075801 (2018).

[30] Y. Yamashita, T. Sato, N. Saitoh, N. Yoshizawa, K. Toko, and T. Suemasu, *Three-step growth of highly photoresponsive $BaSi_2$ light absorbing layers with uniform Ba to Si atomic ratios,* Journal of Applied Physics **126**, 215301 (2019).

[31] T. Sato, H. Hoshida, R. Takabe, K. Toko, Y. Terai, and T. Suemasu, *Detection of local vibrational modes induced by intrinsic defects in undoped $BaSi_2$ light absorber layers using Raman spectroscopy,* Journal of Applied Physics **124**, 025301 (2018).

[32] T. Sato, Y. Yamashita, Z. Xu, K. Toko, S. Gambarelli, M. Imai, and T. Suemasu, *Correlation of native defects between epitaxial films and polycrystalline $BaSi_2$ bulks based on photoluminescence spectra,* Applied Physics Express **12**, 111001 (2019).

[33] L. Benincasa, H. Hoshida, T. Deng, T. Sato, Z. Xu, K. Toko, Y. Terai, and T. Suemasu, *Investigation of defect levels in $BaSi_2$ epitaxial films by photoluminescence and the effect of atomic hydrogen passivation,* Journal of Physics Communications **3**, 075005 (2019).

[34] L. Benincasa, Z. Xu, T. Deng, T. Sato, K. Toko, and T. Suemasu, *Effects of boron and hydrogen doping on the enhancement of photoresponsivity and photoluminescence of $BaSi_2$ epitaxial films,* Japanese Journal of Applied Physics **59**, SFFA08 (2020).

[35] T. Sato, C. Lombard, Y. Yamashita, Z. Xu, L. Benincasa, K. Toko, S. Gambarelli, and T. Suemasu, *Investigation of native defects in $BaSi_2$ epitaxial films by electron paramagnetic resonance,* Applied Physics Express **12**, 025301 (2019).

[36] Y. Yamashita, Y. Takahara, T. Sato, K. Toko, A. Uedono, and T. Suemasu, *Simple way of finding Ba to Si deposition rate ratios for high photoresponsivity in $BaSi_2$ films by Raman spectroscopy,* Applied Physics Express **12**, 055506 (2019).

[37] A. Montes, S. W. H. Eijt, Y. Tian, R. Gram, H. Schut, T. Suemasu, N. Usami, M. Zeman, J. Serra, and O. Isabella, *Point defects in $BaSi_2$ thin films for photovoltaic applications studied by positron annihilation spectroscopy,* Journal of Applied Physics **127**, 085304 (2020).

[38] Y. Imai and A. Watanabe, *Energetic and the electronic structural consideration of the 13th group element (Ga and In) impurity doping to control the conductivity of $BaSi_2$,* Intermetallics **15**, 1291 (2007).

[39] M. Ajmal Khan, K. O. Hara, W. Du, M. Baba, K. Nakamura, M. Suzuno, K. Toko, N. Usami, and T. Suemasu, *In-situ heavily p-type doping of over 10^{20} cm^{-3} in semiconducting $BaSi_2$ thin films for solar cells applications,* Applied Physics Letters **102**, 112107 (2013).

[40] M. A. Khan, K. O. Hara, K. Nakamura, W. Du, M. Baba, K. Toh, M. Suzuno, K. Toko, N. Usami, and T. Suemasu, *Molecular beam epitaxy of boron doped p-type $BaSi_2$ epitaxial films on Si(111) substrates for thin-film solar cells,* Journal of Crystal Growth **378**, 201 (2013).

[41] M. Kobayashi, Y. Matsumoto, Y. Ichikawa, D. Tsukada, and T. Suemasu, *Control of electron and hole concentrations in semiconducting silicide $BaSi_2$ with impurities grown by molecular beam epitaxy,* Applied Physics Express **1**, 0514031 (2008).

[42] M. A. Khan, T. Saito, K. Nakamura, M. Baba, W. Du, K. Toh, K. Toko, and T. Suemasu, *Electrical characterization and conduction mechanism of impurity-doped $BaSi_2$ films grown on Si(111) by molecular beam epitaxy,* Thin Solid Films **522**, 95 (2012).

[43] M. Takeishi, Y. Matsumoto, R. Sasaki, T. Saito, and T. Suemasu, *Growth of Al-doped p-type $BaSi_2$ films by molecular beam epitaxy and the effect of high-temperature annealing on their electrical properties,* Physics Procedia **11**, 27 (2011).

[44] S. Aonuki, Y. Yamashita, K. Toko, and T. Suemasu, *Fabrication of As-doped n-type $BaSi_2$ epitaxial films grown by molecular beam epitaxy,* Japanese Journal of Applied Physics **59**, SFFA01 (2020).

[45] K. O. Hara, N. Usami, M. Baba, K. Toko, and T. Suemasu, *N-type doping of $BaSi_2$ epitaxial films by arsenic ion implantation through a dose-dependent carrier generation mechanism,* Thin Solid Films **567**, 105 (2014).

[46] K. O. Hara, Y. Hoshi, N. Usami, Y. Shiraki, K. Nakamura, K. Toko, and T. Suemasu, *N-type doping of $BaSi_2$ epitaxial films by phosphorus ion implantation and thermal annealing,* Thin Solid Films **557**, 90 (2014).

[47] K. O. Hara, W. Du, K. Arimoto, J. Yamanaka, K. Nakagawa, K. Toko, T. Suemasu, and N. Usami, *Control of electrical properties of $BaSi_2$ thin films by alkali-metal doping using alkali-metal fluorides,* Thin Solid Films **603**, 218 (2016).

[48] M. A. Khan, M. Takeishi, Y. Matsumoto, T. Saito, and T. Suemasu, *Al- and Cu-doped $BaSi_2$ films on Si(111) substrate by molecular beam epitaxy and evaluation of depth profiles of Al and Cu atoms,* Physics Procedia **11**, 11 (2011).

[49] M. Ajmal Khan, T. Saito, M. Takeishi, and T. Suemasu, *Molecular beam epitaxy of Cu-doped $BaSi_2$ films on Si(111) substrate and evaluation & qualification of depth profiles of Cu atoms for the formation of efficient solar cells,* Advanced Materials Research **326**, 139 (2011).

[50] R. Takabe, W. Du, K. Ito, H. Takeuchi, K. Toko, S. Ueda, A. Kimura, and T. Suemasu, *Measurement of valence-band offset at native oxide/$BaSi_2$ interfaces by hard X-ray photoelectron spectroscopy,* Journal of Applied Physics **119**, 165304 (2016).

[51] R. Takabe, K. O. Hara, M. Baba, W. Du, N. Shimada, K. Toko, N. Usami, and T. Suemasu, *Influence of grain size and surface condition on minority-carrier lifetime in undoped n -$BaSi_2$ on Si(111),* Journal of Applied Physics **115**, 0 (2014).

[52] N. Shaalan, K. Hara, C. Trinh, Y. Nakagawa, and N. Usami, *Simple method for significant improvement of minority-carrier lifetime of evaporated $BaSi_2$ thin film by sputtered-AlO_x passivation,* Materials Science in Semiconductor Processing **76**, 37 (2018).

[53] R. Takabe, H. Takeuchi, W. Du, K. Ito, K. Toko, S. Ueda, A. Kimura, and T. Suemasu, *Evaluation of band offset at amorphous-Si/$BaSi_2$ interfaces by hard X-ray photoelectron spectroscopy,* Journal of Applied Physics **119**, 165304 (2016).

[54] D. Tsukahara, S. Yachi, H. Takeuchi, R. Takabe, W. Du, M. Baba, Y. Li, K. Toko, N. Usami, and T. Suemasu, *P-$BaSi_2$/n-Si heterojunction solar cells with conversion efficiency reaching 9.0%,* Applied Physics Letters **108**, 0 (2016).

[55] S. Yachi, R. Takabe, K. Toko, and T. Suemasu, *Effect of p-$BaSi_2$ layer thickness on the solar cell performance of P-$BaSi_2$/n-Si heterojunction solar cells,* Japanese Journal of Applied Physics **56**, 6 (2017).

[56] Z. Xu, K. Gotoh, T. Deng, T. Sato, R. Takabe, K. Toko, N. Usami, and T. Suemasu, *Improving the photoresponse spectra of $BaSi_2$ layers by capping with hydrogenated amorphous Si layers prepared by radio-frequency hydrogen plasma,* AIP Advances **8**, 055306 (2018).

[57] Z. Xu, D. A. Shohonov, A. B. Filonov, K. Gotoh, T. Deng, S. Honda, K. Toko, N. Usami, D. B. Migas, V. E. Borisenko, and T. Suemasu, *Marked enhancement of the photoresponsivity and minority-carrier lifetime of $BaSi_2$ passivated with atomic hydrogen,* Physical Review Materials **3**, 065403 (2019).

[58] Z. Xu, T. Sato, L. Benincasa, Y. Yamashita, T. Deng, K. Gotoh, K. Toko, N. Usami, A. B. Filonov, D. B. Migas, D. A. Shohonov, and T. Suemasu, *Atomic hydrogen passivation for photoresponsivity enhancement of boron-doped p-$BaSi_2$ films and performance improvement of boron-doped p-$BaSi_2$/n-Si heterojunction solar cells,* Journal of Applied Physics **127**, 233104 (2020).

[59] R. A. McKee, F. J. Walker, J. R. Conner, E. D. Specht, and D. E. Zelmon, *Molecular beam epitaxy growth of epitaxial barium silicide, barium oxide, and barium titanate on silicon,* Applied Physics Letters **59**, 782 (1991).

[60] Y. Inomata, T. Nakamura, T. Suemasu, and F. Hasegawa, *Epitaxial growth of semiconducting $BaSi_2$ thin films on Si(111) substrates by reactive deposition epitaxy,* Japanese Journal of Applied Physics, Part 1: Regular Papers and Short Notes and Review Papers **43**, 4155 (2004).

[61] Y. Inomata, T. Nakamura, T. Suemasu, and F. Hasegawa, *Epitaxial growth of semiconducting $BaSi_2$ films on Si(111) substrates by molecular beam epitaxy,* Japanese Journal of Applied Physics, Part 2: Letters **43**, L478 (2004).

[62] Y. Matsumoto, D. Tsukada, R. Sasaki, M. Takeishi, and T. Suemasu, *Photoresponse properties of semiconducting $BaSi_2$ epitaxial films grown on Si(111) substrates by molecular beam epitaxy,* Applied Physics Express **2**, 021101 (2009).

[63] D. Tsukada, Y. Matsumoto, R. Sasaki, M. Takeishi, T. Saito, N. Usami, and T. Suemasu, *Fabrication of (111)-oriented Si layers on SiO_2 substrates by an aluminum-induced crystallization method and subsequent growth of semiconducting $BaSi_2$ layers for photovoltaic application,* Journal of Crystal Growth **311**, 3581 (2009).

[64] D. Tsukada, Y. Matsumoto, R. Sasaki, M. Takeishi, T. Saito, N. Usami, and T. Suemasu, *Photoresponse properties of polycrystalline $BaSi_2$ films grown on SiO_2 substrates using (111)-oriented Si layers by an aluminum-induced crystallization method,* Applied Physics Express **2**, 2 (2009).

[65] M. Baba, K. Toh, K. Toko, N. Saito, N. Yoshizawa, K. Jiptner, T. Sekiguchi, K. O. Hara, N. Usami, and T. Suemasu, *Investigation of grain boundaries in $BaSi_2$ epitaxial films on Si(111) substrates using transmission electron microscopy and electron-beam-induced current technique,* Journal of Crystal Growth **348**, 75 (2012).

[66] M. Baba, K. Nakamura, W. Du, M. A. Khan, S. Koike, K. Toko, N. Usami, N. Saito, N. Yoshizawa, and T. Suemasu, *Molecular beam epitaxy of $BaSi_2$ films with grain size over 4* micro*meter on Si(111),* Japanese Journal of Applied Physics **51** (2012), 10.1143/JJAP.51.098003.

[67] M. Baba, K. Toh, K. Toko, K. O. Hara, N. Usami, N. Saito, N. Yoshizawa, and T. Suemasu, *Formation of large-grain-sized $BaSi_2$ epitaxial layers grown on Si(111) by molecular beam epitaxy,* Journal of Crystal Growth **378**, 193 (2013).

[68] K. O. Hara, N. Usami, K. Nakamura, R. Takabe, M. Baba, K. Toko, and T. Suemasu, *Determination of bulk minority-carrier lifetime in $BaSi_2$ earth-abundant absorber films by utilizing a drastic enhancement of carrier lifetime by post-growth annealing,* Applied Physics Express **6**, 2 (2013).

[69] R. Takabe, K. Toko, K. O. Hara, N. Usami, and T. Suemasu, *Fabrication and characterization of $BaSi_2$ films on Ge(111) substrates by molecular beam epitaxy,* in *2015 IEEE 42nd Photovoltaic Specialist Conference (PVSC)*, 111 (IEEE, 2015) pp. 1–4.

[70] K. O. Hara, Y. Nakagawa, T. Suemasu, and N. Usami, *Realization of single-phase $BaSi_2$ films by vacuum evaporation with suitable optical properties and carrier lifetime for solar cell applications,* Japanese Journal of Applied Physics **54**, 07JE02 (2015).

[71] Y. Nakagawa, K. O. Hara, T. Suemasu, and N. Usami, *Fabrication of single-phase polycrystalline $BaSi_2$ thin films on silicon substrates by vacuum evaporation for solar cell applications,* Japanese Journal of Applied Physics **54**, 08KC03 (2015).

[72] T. Suhara, K. Murata, A. Navabi, K. O. Hara, Y. Nakagawa, C. T. Trinh, Y. Kurokawa, T. Suemasu, K. L. Wang, and N. Usami, *Postannealing effects on undoped $BaSi_2$ evaporated films grown on Si substrates,* Japanese Journal of Applied Physics **56**, 05DB05 (2017).

[73] C. T. Trinh, Y. Nakagawa, K. O. Hara, Y. Kurokawa, R. Takabe, T. Suemasu, and N. Usami, *Growth of $BaSi_2$ film on Ge(100) by vacuum evaporation and its photoresponse properties,* Japanese Journal of Applied Physics **56**, 05DB06 (2017).

[74] Z. Yang, Z. Hao, and Q. Xie, *Effects of annealing temperature on the structure and surface feature of $BaSi_2$ films grown on Si(111) substrates,* Physics Procedia **11**, 118 (2011).

[75] N. A. A. Latiff, T. Yoneyama, T. Shibutami, K. Matsumaru, K. Toko, and T. Suemasu, *Fabrication and characterization of polycrystalline $BaSi_2$ by RF sputtering,* Physica Status Solidi (C) Current Topics in Solid State Physics **10**, 1759 (2013).

[76] T. Yoneyama, A. Okada, M. Suzuno, T. Shibutami, K. Matsumaru, N. Saito, N. Yoshizawa, K. Toko, and T. Suemasu, *Formation of polycrystalline $BaSi_2$ films by radio-frequency magnetron sputtering for thin-film solar cell applications,* Thin Solid Films **534**, 116 (2013).

[77] S. Matsuno, R. Takabe, S. Yokoyama, K. Toko, M. Mesuda, H. Kuramochi, and T. Suemasu, *Significant photoresponsivity enhancement of polycrystalline $BaSi_2$ films formed on heated Si(111) substrates by sputtering,* Applied Physics Express **11**, 071401 (2018).

[78] R. Du, K. Yang, X. Gao, W. Shi, W. Du, Y. Zhang, and T. Suemasu, *Formation of polycrystalline $BaSi_2$ thin films by pulsed laser deposition for solar cell applications,* Materials Letters **260**, 126936 (2020).

[79] K. O. Hara, S. Takizawa, J. Yamanaka, N. Usami, and K. Arimoto, *Reactive deposition growth of highly (001)-oriented $BaSi_2$ films by close-spaced evaporation,* Materials Science in Semiconductor Processing **113**, 105044 (2020).

[80] N. G. Galkin, D. L. Goroshko, V. L. Dubov, D. V. Fomin, K. N. Galkin, E. A. Chusovitin, and S. V. Chusovitina, *SPE grown $BaSi_2$ on Si(111) substrates: Optical and photoelectric properties of films and diode heterostructures on their base,* Japanese Journal of Applied Physics **59**, SFFA11 (2020).

[81] S. Kishino, T. Iida, T. Kuji, and Y. Takanashi, *Crystal growth of orthorhombic $BaSi_2$ by the vertical bridgman method,* Thin Solid Films **461**, 90 (2004).

[82] A. Pokhrel, L. Samad, F. Meng, and S. Jin, *Synthesis and characterization of barium silicide ($BaSi_2$) nanowire arrays for potential solar applications,* Nanoscale **7**, 17450 (2015).

[83] A. Y. Cho and J. Arthur, *Molecular beam epitaxy,* Progress in solid state chemistry **10**, 157 (1975).

[84] J. R. Arthur, *Molecular beam epitaxy,* Surface Science **500**, 189 (2002).

[85] R. A. McKee, F. J. Walker, J. R. Conner, and R. Raj, *$BaSi_2$ and thin film alkaline earth silicides on silicon,* Applied Physics Letters **63**, 2818 (1993).

[86] T. Suemasu and N. Usami, *Exploring the potential of semiconducting $BaSi_2$ for thin-film solar cell applications,* Journal of Physics D: Applied Physics **50**, 023001 (2016).

[87] K. O. Hara, C. T. Trinh, K. Arimoto, J. Yamanaka, K. Nakagawa, Y. Kurokawa, T. Suemasu, and N. Usami, *Effects of deposition rate on the structure and electron density of evaporated $BaSi_2$ films,* Journal of Applied Physics **120**, 045103 (2016).

[88] Q. Deng, H. Chen, H. Liao, L. Chen, G. Wang, S. Wang, and Y. Shen, *Numerical simulation and optimization of Si/$BaSi_2$ heterojunction and $BaSi_2$ homojunction solar cells,* Journal of Physics D: Applied Physics **52**, 075501 (2019).

[89] J.-S. Huang, K.-W. Lee, and Y.-H. Tseng, *Analysis of the high conversion efficiencies β-$FeSi_2$ and $BaSi_2$ n-i-p thin film solar cells,* Journal of Nanomaterials **2014**, 1 (2014).

[90] K. Takahashi, Y. Nakagawa, K. O. Hara, Y. Kurokawa, and N. Usami, *Investigation of p-type emitter layer materials for heterojunction barium disilicide thin film solar cells,* Japanese Journal of Applied Physics **56**, 05DB04 (2017).

[91] H. Liao, Q. Deng, Y. Shen, G. Wang, S. Wang, and Y. Mao, *Theoretical analysis of doping concentration, layer thickness and barrier height effects on $BaSi_2$ based homojunction solar cells toward high efficiency,* Solar Energy **201**, 857 (2020).

[92] S. R. I. Biplab, M. H. Ali, M. M. A. Moon, M. F. Pervez, M. F. Rahman, and J. Hossain, *Performance enhancement of CIGS-based solar cells by incorporating an ultrathin $BaSi_2$ BSF layer,* Journal of Computational Electronics **19**, 342 (2020).

[93] M. M. A. Moon, M. H. Ali, M. F. Rahman, A. Kuddus, J. Hossain, and A. B. M. Ismail, *Investigation of thin-film p-$BaSi_2$/n-CdS heterostructure towards semiconducting silicide based high efficiency solar cell,* Physica Scripta **95**, 035506 (2020).

[94] A. Sasaki, Y. Kataoka, K. Aoki, S. Saito, K. Kobayashi, T. Ito, K. Kakushima, and H. Iwai, *Power generation characteristics of Schottky-type solar cells fabricated using barium silicide,* Japanese Journal of Applied Physics **54**, 031202 (2015).

[95] T. Suemasu, M. Sasase, Y. Ichikawa, M. Kobayashi, and D. Tsukada, *Semiconductor($BaSi_2$)/metal($CoSi_2$) Schottky-barrier structures epitaxially grown on Si(111) substrates by molecular beam epitaxy,* Journal of Crystal Growth **310**, 1250 (2008).

[96] Y. Ichikawa, M. Kobayashi, M. Sasase, and T. Suemasu, *Molecular beam epitaxy of semiconductor ($BaSi_2$)/metal ($CoSi_2$) hybrid structures on Si(111) substrates for photovoltaic application,* Applied Surface Science **254**, 7963 (2008).

[97] C. Pirri, J. C. Peruchetti, D. Bolmont, and G. Gewinner, *Surface structure of epitaxial $CoSi_2$ crystals grown on Si(111),* Physical Review B **33**, 4108 (1986).

[98] T. Suemasu, K. Morita, M. Kobayashi, M. Saida, and M. Sasaki, *Band diagrams of $BaSi_2$/Si structure by Kelvin probe and current-voltage characteristics,* Japanese Journal of Applied Physics **45**, L519 (2006).

[99] W. Du, R. Takabe, M. Baba, H. Takeuchi, K. O. Hara, K. Toko, N. Usami, and T. Suemasu, *Formation of $BaSi_2$ heterojunction solar cells using transparent MoO_x hole transport layers,* Applied Physics Letters **106**, 122104 (2015).

[100] K. O. Hara, K. Arimoto, J. Yamanaka, and K. Nakagawa, *Fabrication of SnS/$BaSi_2$ heterojunction by thermal evaporation for solar cell applications,* Japanese Journal of Applied Physics **58**, SBBF01 (2019).

[101] K. O. Hara, K. Arimoto, J. Yamanaka, and K. Nakagawa, *Interface reaction of the SnS/$BaSi_2$ heterojunction fabricated for solar cell applications,* Thin Solid Films **706**, 138064 (2020).

[102] S. Bhatia, I. M. Khorakiwala, P. R. Nair, and A. Antony, *Influence of post deposition fabrication steps and quantitative estimation of band diagram of Si/MoO_x heterojunction for carrier selective solar cells,* Solar Energy **194**, 141 (2019).

[103] J. Bullock, A. Cuevas, T. Allen, and C. Battaglia, *Molybdenum oxide MoO_x: A versatile hole contact for silicon solar cells,* Applied Physics Letters **105**, 232109 (2014).

[104] T. Saito, Y. Matsumoto, M. Suzuno, M. Takeishi, R. Sasaki, T. Suemasu, and N. Usami, *Fabrication of n^+-$BaSi_2$/p^+-Si tunnel junction on Si(111) surface by molecular beam epitaxy for photovoltaic applications,* Applied Physics Express **3**, 1 (2010).

[105] W. Du, M. Suzuno, M. A. Khan, K. Toh, M. Baba, K. Nakamura, K. Toko, N. Usami, and T. Suemasu, *Improved photoresponsivity of semiconducting $BaSi_2$ epitaxial films grown on a tunnel junction for thin-film solar cells,* Applied Physics Letters **100**, 98 (2012).

[106] S. Yachi, R. Takabe, H. Takeuchi, K. Toko, and T. Suemasu, *Effect of amorphous Si capping layer on the hole transport properties of $BaSi_2$ and improved conversion efficiency approaching 10% in p-$BaSi_2$/n-Si solar cells,* Applied Physics Letters **109**, 072103 (2016).

[107] K. Kodama, R. Takabe, T. Deng, K. Toko, and T. Suemasu, *Spectroscopic evidence of photogenerated carrier separation by built-in electric field in Sb-doped n-$BaSi_2$/B-doped p-$BaSi_2$ homojunction diodes,* Japanese Journal of Applied Physics **57**, 050310 (2018).

[108] K. Kodama, Y. Yamashita, K. Toko, and T. Suemasu, *Operation of $BaSi_2$ homojunction solar cells on p^+-Si(111) substrates and the effect of structure parameters on their performance,* Applied Physics Express **12**, 041005 (2019).

3

Experimental

3.1. Depositions

Typical physical and chemical deposition processes are shown in Figure 3.1. In the physical processes or (physical vapor deposition, PVD), the growth species is transferred from a source (or target) and deposited on a substrate to form a film. The process is essentially atomistic and no chemical reaction is involved. In this section, we majorly discuss the sputtering process applied for depositions of $BaSi_2$ and Si films, and the thermal evaporation process used for the deposition of metal contacts.

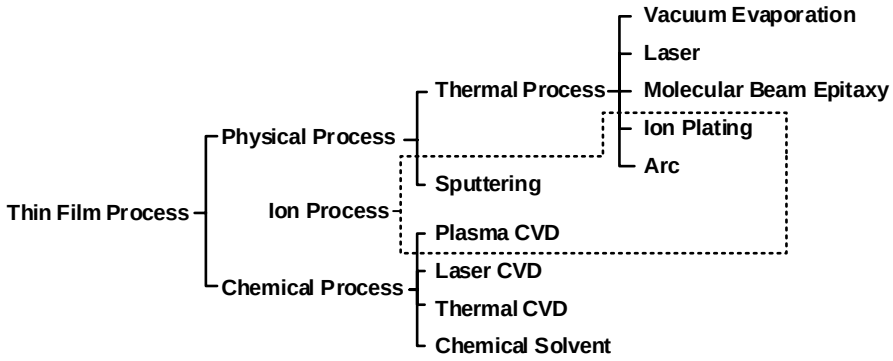

Figure 3.1: Thin-film deposition techniques

3.1.1. Sputtering

When a solid surface is bombarded with energetic particles such as accelerated ions, surface atoms of the solid are scattered backward due to collisions between the surface atoms and the energetic particle, as illustrated in Figure 3.2. This phenomenon is called back-sputtering, or simply sputtering. In a typical sputtering deposition chamber, the source and substrate are placed on the two electrodes facing each other. The target material electrode is the cathode, while the substrate is placed on the anode. An introduced gas such as argon at low pressure is used as the medium. When a high electric field is applied to initiate the glow discharge between the electrodes, free electrons are accelerated by the electric field and ionize the argon atoms. The Ar^+ ions thus generated are accelerated at the cathode fall (sheath) and sputter the target resulting in the ejection of target atoms. These target atoms pass through the glow discharge and deposit on the substrate electrode.

Several sputtering systems are proposed for thin-film deposition including direct-current (dc) diode, radio-frequency (rf) diode, and magnetron sputtering [1]. In the dc sputtering system, the target is composed of metal since the glow discharge (current flow) is maintained between the metallic electrodes. By simple substitution of an insulator for the metal target in the dc sputtering discharge system, the sputtering discharge cannot be sustained because of the immediate buildup of a surface charge of positive ions on the front side of the insulator. To sustain the glow discharge with the insulator target, rf voltage is supplied to the target. This system is called rf sputtering. In the rf-sputtering system, the thin films of the insulator are sputtered directly from the insulator

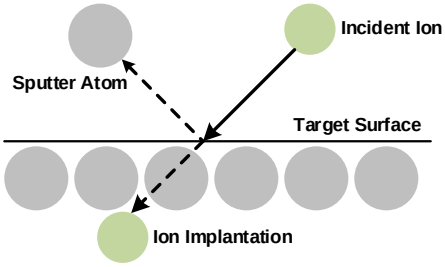

Figure 3.2: Physical sputtering process

target.

In magnetron sputtering, a magnetic field is superposed on the cathode and glow discharge, which is parallel to the cathode surface. The electrons in the glow discharge show cycloidal motion, and the center of the orbit presents a drift velocity of

$$\boldsymbol{V}_{\mathrm{E}} = \frac{\boldsymbol{E} \times \boldsymbol{b}}{|\boldsymbol{B}|}, \tag{3.1}$$

where $\boldsymbol{E}$ and $\boldsymbol{B}$ denote the electric field in the discharge and the superposed transverse magnetic field, respectively, $\boldsymbol{b}$ is the unit vector along magnetic field, $\boldsymbol{b} = \boldsymbol{B}/|\boldsymbol{B}|$ [2]. The magnetic field is oriented such that these drift paths for electrons form a closed loop. This electron trapping effect increases the collision rate between the electrons and the sputtering gas molecules. This enables one to lower the sputtering gas pressure. In the magnetron sputtering system, the magnetic field increases the plasma density which leads to increases in the current density at the cathode target, effectively increasing the sputtering rate at the target. Due to the low working pressure, the sputtered particles traverse the discharge space without collisions, which results in a high deposition rate [3].

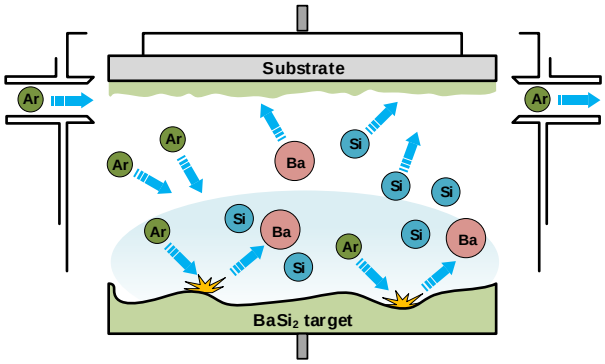

Figure 3.3: Schematic illustration of the sputtering process of $BaSi_2$ films

In this research, an rf-magnetron sputtering system is applied for the depositions of $BaSi_2$ and Si thin films. Figure 3.3 illustrates the sputtering process of $BaSi_2$ thin films.

A stoichiometric ceramic $BaSi_2$ target is used for depositions. Ar is the sputtering gas. Detailed sputtering parameters of $BaSi_2$ deposition is discussed in Chapter 4. As for the deposition of Si layers, the intrinsic crystalline Si target is used, and its deposition details are provided in Chapter 7. The targets information is summarised in Table 3.1.

Table 3.1: Information of $BaSi_2$ and Si targets.

Target	Purity	Size	Doping	Type	Main impurities
$BaSi_2$	-	3 inch	Undoped	Polycrystalline	Sr(0.3 wt%), Ca(200 ppm), O(0.5 wt%)
Si	99.999%	7 inch	Undoped	Monocrystalline	-

3.1.2. Vacuum evaporation

Evaporation is the simplest and the most widely used method for the preparation of thin films. One merely has to produce a vacuum environment in which a sufficient amount of heat is given to the evaporant to attain the vapor pressure necessary for evaporation, then the evaporated material is allowed to condense on a substrate kept at a suitable temperature. Vacuum evaporation consists of three distinguishable steps [4],

1. Transition of the condensed phase (solid or liquid) into the gaseous state.

2. Traversal by the vapor of the space between the vapor source and the substrate (i.e., transport of the vapor from the source to the substrate).

3. Condensation of the vapor upon arrival at the substrate (i.e., deposition of these particles on the substrate).

In this thesis, a Provac PRO500S evaporation system is applied for metallization. Both resistive thermal evaporation (with a tungsten boat) and electron-beam (e-beam) evaporation can be conducted in the system. In the case of thermal evaporation, the glowing tungsten boat melts the material with a relatively low melting point, for example, Ag which has a melting point of about 960 °C. In respect to e-beam evaporation, the electrons are generated normally by thermionic emission and accelerated to attain high kinetic energy. The electron beam is redirected by a magnetic field and impinges on the evaporation material in the crucible. Upon striking the material, the kinetic energy is converted to other forms of energy among which the thermal energy melts the material and generates the vapor flux. E-beam evaporation is originally designed for evaporating material with high melting points, for example, Cr with a melting point of 1907 °C.

3.2. Property and structure characterizations

3.2.1. Optical characterizations

Optical measurements enable non-contacting material characterizations with minimal sample preparations. Optical measurements fall into three broad categories [5],

i. photometric measurements (amplitude of reflected or transmitted light is measured),

ii. interference measurements (phase of reflected or transmitted light is measured),

iii. polarization measurements (ellipticity of reflected light is measured).

Figure 3.4 summaries main optical characterization techniques. Light is either reflected, absorbed, emitted, or transmitted by the specimen during the optical measurements. For this thesis, techniques including Raman spectroscopy, spectroscopic ellipsometry, transmission, and reflection are used for the thin-film structure and property characterizations.

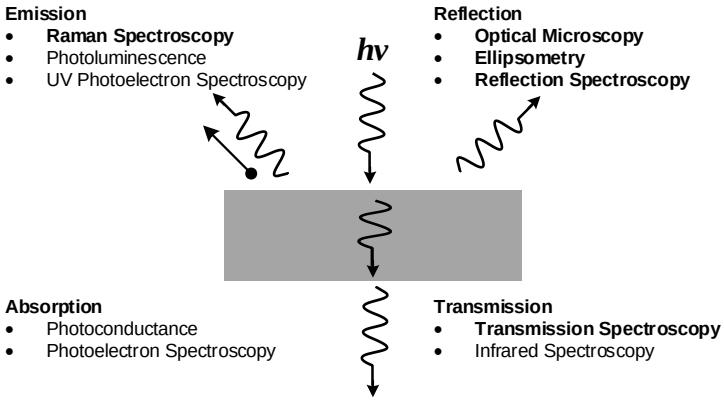

Figure 3.4: Optical characterization techniques, reproduced from Ref. [5].

Raman spectroscopy

Raman Spectroscopy is a non-destructive chemical analysis technique that provides detailed information about chemical structure, phase and polymorphy, crystallinity, and molecular interactions. It is based on the Raman effect first experimentally observed by Raman and Krishnan in 1928 [6].

When light interacts with the sample surface, light is mainly elastically scattered (i.e., the energy of the scattered photon is equal to that of the incident photon), which is often referred to as Rayleigh scattering. The inelastic scattering of light by matter (i.e., the energy of the scattered photon is not equal to that of the incident photon) is known as the Raman effect. If the incident photon imparts energy to the lattice in the form of a phonon (phonon emission), it emerges as a lower-energy photon. This down-converted frequency shift is known as Stokes-shifted scattering. In anti-Stokes-shifted scattering, the photon absorbs a phonon and emerges with higher energy [7]. They are shown in Figure 3.5. The anti-Stokes mode is much weaker than the Stokes mode and it is Stokes-mode that is usually monitored.

The shift in angular frequency of the scattered light can be described by the following equation:

$$\omega_{\text{scat}} = \omega_{\text{p}} \pm \omega_{\text{osc}}, \tag{3.2}$$

where ω_{osc} denotes the lattice or molecule vibration, ω_{p} denotes the incident photon (often referred to as the pump photon) and ω_{scat} denotes the scattered light [6, 8]. The bi-

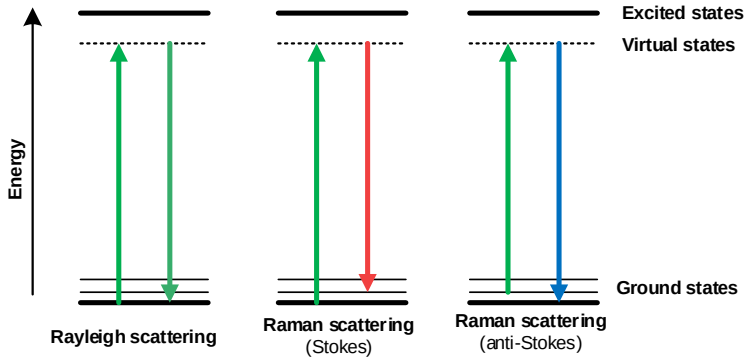

Figure 3.5: Diagram of Rayleigh and Raman scattering processes.

nary operator (±) is determined by energy decrease or increase of scattered light, which corresponds to Stokes and anti-Stokes Raman scattering, respectively.

During Raman spectroscopy measurements a laser pump beam is incident on the sample, as shown in Figure 3.6. Laser light is focused onto the sample surface by a microscope objective lens, which is also employed for the collection of the backscattered light. Notch or edge filters filter out Raman-shifted photons and they are finally fed into a grating spectrometer enabling the simultaneous detection of the wavenumbers in a selected spectral range by use of a charge-coupled device (CCD) detector [7, 9].

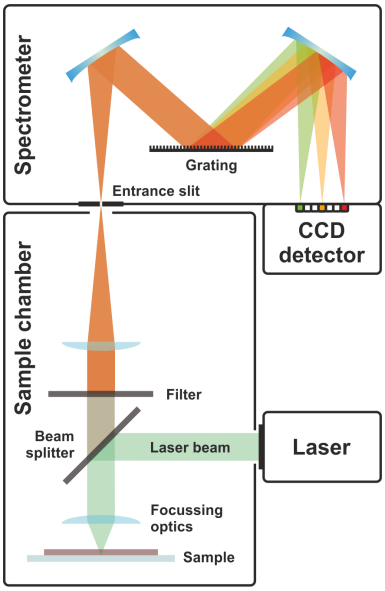

Figure 3.6: Schematic of Raman spectroscopy setup, adapted with Ref. [10].

Most semiconductors can be characterized by Raman spectroscopy. The wavelengths of the scattered light are analyzed and matched to known wavelengths for identification. In this research, Raman spectroscopy is employed to identify the crystalline $BaSi_2$, as well as its impurity compositions. By using lasers with various wavelengths and hence different penetration depths, profiling the sample to some depths is also possible [5]. Meanwhile, Raman mapping can also be realized by step-wise movement of the sample through the laser focus, while acquiring a Raman spectrum in every pixel of an image [9].

Spectroscopic ellipsometry (SE)

Ellipsometry is a contactless, non-invasive technique measuring changes in the polarization state of light reflected from a surface. Figure 3.7 explains the basic principle of ellipsometry. Considering plane-polarized incident on a plane surface, as illustrated in Figure 3.7, the incident polarized light can be resolved into a p-polarization component $\boldsymbol{E}_{f,ip}$ and a s-polarization component $\boldsymbol{E}_{f,is}$. The oscillatory direction of the p-polarization is parallel to the incident plane, while that of the s-polarization is perpendicular.

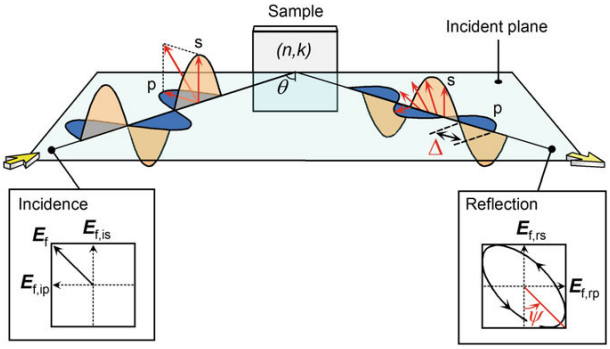

Figure 3.7: Basic principle of ellipsometry. The waves indicated as s and p represent s- and p-polarized light waves. The oscillatory direction of the p-polarization is parallel to the incident plane of samples.The $\boldsymbol{E}_f$ shows the electric field vector and the subscripts i, r, s, and p for $\boldsymbol{E}_f$ denote the incidence, reflection, s-polarization and p-polarization, respectively [11].

For zero absorption material, only the amplitude of the reflected wave is affected. Linearly polarized light is reflected as linearly polarized light. However, the two components experience different amplitudes and phase shifts upon reflection for absorbing materials and for multiple reflections in a thin layer between air and the substrate. In particular, the amplitude of the p- and s-polarized waves and the phase between these polarizations change depending on the optical constants (n, k) and film thickness. The name of the technique "ellipsometry" originates from the fact that polarized light often becomes "elliptical" upon light reflection, as depicted in Figure 3.7.

Ellipsometry measures the two values (Ψ, Δ), which represent the amplitude ratio Ψ and phase difference Δ between the p-polarization and s-polarization, respectively. The (Ψ, Δ) measured from ellipsometry are defined by

$$\rho = \tan(\Psi)\exp(i\Delta) = \frac{r_p}{r_s}, \tag{3.3}$$

where r_p and r_s are amplitude reflection coefficients for the p- and s-polarizations. They can be expressed as

$$r_p = \frac{\boldsymbol{E}_{\mathrm{f},rp}}{\boldsymbol{E}_{\mathrm{f},ip}} = |r_p|\exp(i\delta_p), \tag{3.4}$$

$$r_s = \frac{\boldsymbol{E}_{\mathrm{f},rs}}{\boldsymbol{E}_{\mathrm{f},is}} = |r_s|\exp(i\delta_s), \tag{3.5}$$

where $|r|$ and δ represent the amplitude ratio and phase difference between the incident and reflected waves, respectively. From Equation 3.3 - 3.5, it follws that

$$\tan\Psi = \frac{|r_p|}{|r_s|}, \tag{3.6}$$

$$\Delta = \delta_p - \delta_s. \tag{3.7}$$

For actual ellipsometry measurements, various optical elements, including a polarizer, analyzer, and compensator, are used. In conventional ellipsometry instruments, these optical parts are rotated, and the polarization state of the reflected light is determined based on the variation of the reflected light intensity with the rotation angle of the optical element. In spectroscopic ellipsometry (SE), white light generated by xenon, halogen, and/or deuterium lamps is used as a probe, and (Ψ, Δ) values for all the wavelengths are measured simultaneously using multichannel detectors.

The SE data analysis procedure is summarized in Figure 3.8. An optical mode is constructed for measured (Ψ, Δ). The model is normally defined by the thickness of component layers, surface roughness, optical constants, the substrate, etc. By employing the constructed optical model and the optical data, the SE spectra are calculated using Equation 3.3. The calculated SE spectra are fitted to the experimental spectra using some analytical parameters as fitting parameters. Finally, from the parameters that provide the best fitting, the optical constants and thin-film structure are determined. By analyzing the extracted optical spectrum, the absorption coefficient (α) and the band gap (E_g) of semiconductor materials can further be determined [11].

Transmission and reflection

When radiant flux is incident upon a surface or medium, three processes occur, i.e., transmission, absorption, and reflection.

Transmission is the term used to describe the process by which incident radiant flux leaves a surface or medium from a side other than the incident side, usually the opposite side. The spectral transmittance $T(\lambda)$ of a medium is the ratio of the transmitted spectral flux $\Phi_{\lambda t}$ to the incident spectral flux $\Phi_{\lambda i}$, or

$$T(\lambda) = \frac{\Phi_{\lambda t}}{\Phi_{\lambda i}}. \tag{3.8}$$

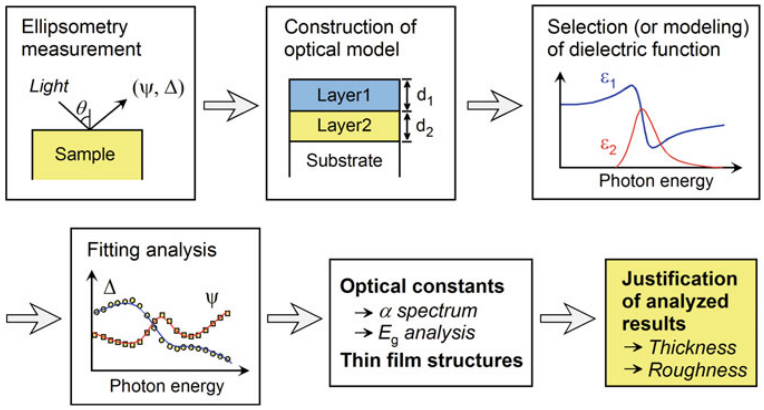

Figure 3.8: Data analysis procedure for spectroscopic ellipsometry measurements [11].

Reflection is the process where a fraction of the radiant flux incident on a surface is returned into the same hemisphere whose base is the surface and which contains the incident radiation. The reflection can be specular (in the mirror direction), diffuse (scattered into the entire hemisphere), or a combination of both. The most general definition for specular reflectance $R(\lambda)$ is the ratio of the radiant flux reflected $\Phi_{\lambda r}$ to the incident radiant flux $\Phi_{\lambda i}$, or

$$R(\lambda) = \frac{\Phi_{\lambda r}}{\Phi_{\lambda i}}. \tag{3.9}$$

Absorption is the process by which incident radiant flux is converted to another form of energy, usually heat. Absorptance is the fraction of incident flux that is absorbed. The specular absorptance $A(\lambda)$ is defined by

$$A(\lambda) = \frac{\Phi_{\lambda a}}{\Phi_{\lambda i}}, \tag{3.10}$$

where $\Phi_{\lambda a}$ is the absorbed radiant flux.

Radiant flux incident upon a surface or medium undergoes transmission, reflection, and absorption. Application of conservation of energy leads to the statement that the sum of the transmission, reflection, and absorption of the incident flux is equal to unity, or

$$A(\lambda) + T(\lambda) + R(\lambda) = 1. \tag{3.11}$$

In this thesis, specular transmittance and reflectance are measured with a LAMBDA UV-vis-NIR spectrometer equipped with a 150-mm integrating sphere as shown in Figure 3.9.

3.2.2. Electrical characterizations

Hall effect

The Hall effect was discovered by Edwin Hall in 1879, which originally was an investigation on the nature of force acting on a conductor carrying a current in a magnetic

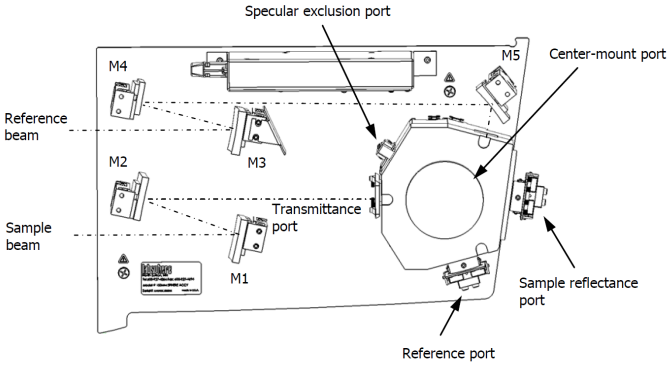

Figure 3.9: Top-view diagram of a 150-mm integrating sphere installed in LAMBDA spectrometer [12].

field [13]. It can be described as the production of a voltage difference (the Hall voltage, V_H) across an electrical conductor (or semiconductor), transverse to an electric current in the conductor and to an applied magnetic field perpendicular to the current. The Hall effect measurement technique has found wide application in the characterization of semiconductor materials because it gives the resistivity, carrier density, and mobility.

Considering a p-type semiconductor sample in Figure 3.10, an electric current (I) flows in the x-direction, indicated by the holes flowing to the right and a magnetic fiedl B is applied in the z direction. The current can be written as

$$I = qwdpv_x, \tag{3.12}$$

where wd is the area, q is the elementary charge, p is the hole concentration of the sample, and v_x is the hole velocity along the x-direction.

The voltage along the x-direction is given by

$$V_\rho = \frac{\rho s I}{wd}, \tag{3.13}$$

from which the resistivity is derived as

$$\rho = \frac{wd}{s}\frac{V_\rho}{I}. \tag{3.14}$$

When a magnetic field $\boldsymbol{B}$ with a perpendicular component is present, charges (here holes) experience a Lorentz force. The force on the holes can be expressed as

$$\boldsymbol{F} = q(\boldsymbol{E} + v \times \boldsymbol{B}). \tag{3.15}$$

The magnetic field in conjunction with the current deflects some holes to the bottom of the sample, as indicated in Figure 3.10. This leaves equal and opposite charges exposed on the other face and results in an asymmetric distribution of charge density across the sample. This caused a steady electric potential V_H.

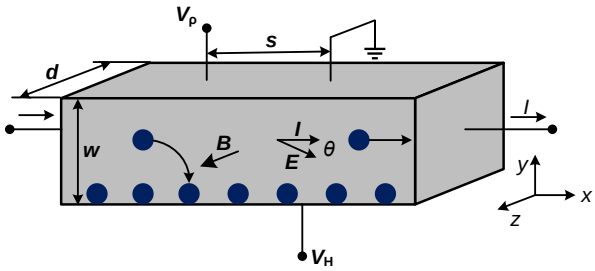

Figure 3.10: Schematic illustration of the Hall effect in a p-type semiconductor sample.

In the y-direction there is no net force on the holes since no current can flow in that direction and $\boldsymbol{F}_y = 0$, or

$$E_y = Bv_x = \frac{BI}{qwdp}. \tag{3.16}$$

The Hall voltage V_H is given by

$$V_H = \int_0^{V_H} \mathrm{d}V = -\int_w^0 E_y \mathrm{d}y = -\int_w^0 \frac{BI}{qwdp}\mathrm{d}y = \frac{BI}{qdp}. \tag{3.17}$$

The Hall coefficient R_H is defined as

$$R_H = \frac{dV_H}{BI}. \tag{3.18}$$

The Hall angle θ between the current and the net electric field is

$$\tan\theta = \frac{E_y}{E_x} = B\mu_p, \tag{3.19}$$

using $I = qp\mu_p E_x wd$, where μ_p is the hole mobility.

Combining Equation 3.17 and 3.18 results

$$p = \frac{1}{qR_H}, \tag{3.20}$$

for p-type semiconductors. Similarly, the electron concentration of n-type semiconductor can be written as

$$n = -\frac{1}{qR_H}. \tag{3.21}$$

Equation 3.20 and 3.21 are derived under simplifying assumptions of energy independent scattering mechanisms. With this assumption relaxed, the expressions for the hole and electron densities become [5],

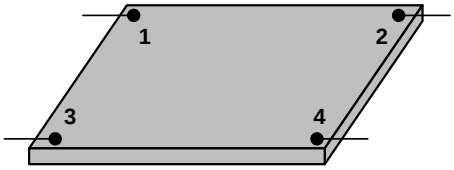

Figure 3.11: Resistivity and Hall effect measurement sample

$$p = \frac{r}{qR_{\mathrm{H}}}, \tag{3.22}$$

$$n = -\frac{r}{qR_{\mathrm{H}}}, \tag{3.23}$$

where r is the Hall scattering factor. The Hall mobility μ_H, defined by

$$\mu_H = \frac{|R_{\mathrm{H}}|}{\rho} \tag{3.24}$$

can be written as

$$\mu_{\mathrm{H}} = r\mu_p, \text{for } p\text{−type;} \tag{3.25}$$

$$\mu_{\mathrm{H}} = r\mu_n, \text{for } n\text{−type.} \tag{3.26}$$

Hall mobilities can differ significantly from conductivity mobilities since r is generally larger than unity. For most Hall-determined mobilities, r is taken as unity, but this assumption should be specified.

For resistivity and Hall effect measurements, the samples are prepared with a conformal mapping developed by van der Pauw [14]. Figure 3.11 shows a square van der Pauw sample. The resistivity the sample is given by

$$\rho = \frac{\pi d}{\ln 2} \frac{(R_{12,34} + R_{23,41})}{2}, \tag{3.27}$$

where $R_{12,34} = V_{34}/I$. The current I enters the sample through contact 1 and leaves through contact 2, and $V_{34} = V_3 - V_4$ is the voltage between contacts 3 and 4. $R_{23,41}$ is similarly defined. Current enters the sample through two adjacent terminals and the voltage is measured across the other two adjacent terminals.

Dark conductivity and activation energy

The conductivity (σ) is a function of the electron (n) and hole (p) concentrations and mobilities (μ_n and μ_p), which can be given as

$$\sigma = q(\mu_n n + \mu_p p). \tag{3.28}$$

Due to the mobility effects, the conductivity is not a linear function of n or p. Mobilities are functions of impurity concentrations, conductivity, then is a somewhat complicated function of impurity concentration [15].

If we consider, for example, a n-type semiconductor with a donor doping concentration N_d is significantly larger than acceptor doping concentration N_a, and if we assume that the electron and hole mobilities are of the same order of magnitude, then the conductivity becomes

$$\sigma \approx q\mu_n n. \tag{3.29}$$

The electron concentration can be expressed as

$$n = N_{\mathrm{C}} \exp \frac{-(E_{\mathrm{C}} - E_{\mathrm{F}})}{kT}, \tag{3.30}$$

where N_{C} is the effective density of the conduction band states, E_{F} is the Fermi energy, E_{C} is the minimum attainable conduction-band energy, and k is the Boltzmann constant. Combining Equation 3.29 and 3.30, the conductivity can be given as

$$\sigma \approx q\mu_n N_{\mathrm{C}} \exp \frac{-(E_{\mathrm{C}} - E_{\mathrm{F}})}{kT} = \sigma_0 \exp(\frac{-E_{\mathrm{a}}}{kT}). \tag{3.31}$$

where σ_0 is a pre-exponential factor, and E_{a} is the characteristic activation energy.

Figure 3.12 shows the schematic illustration of the sample lay-out for dark conductivity measurement. A pair of Al stripes are deposited on the tested film. The sample is mounted on a temperature-controlled stage. A constant voltage (V) is applied between two metal contacts and the current (I) is measured at different temperatures. The temperature-dependent conductivity can be measured by

$$\sigma(T) = \frac{I}{V} \frac{l}{wd}, \tag{3.32}$$

where l is the distance between two contacts, w is the length of contacts, d is the film thickness. Then, the activation energy (E_{a}) can be derived from Equation 3.31.

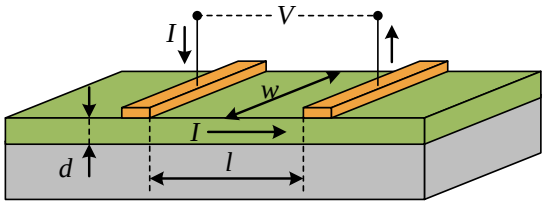

Figure 3.12: Schematic diagram of the dark conductivity and activation energy measurement.

3.2.3. Surface topography characterizations

Atomic force microscopy

Atomic force microscopy (AFM) operates by measuring the force between a probe and the sample. This force depends on the nature of the sample, the distance between the probe and the sample, the probe geometry, and sample surface contamination. AFM is suitable for conducting as well as insulating samples.

The working principle of AFM is illustrated in Figure 3.13. The instrument consists of a cantilever with a sharp tip mounted on its end that is used to scan the specimen surface. For topographic imaging, the tip is brought into continuous or intermittent contact with the sample and scanned across the sample surface. Forces between the tip and the sample lead to a deflection of the cantilever. The motion of the cantilever then is sensed by the photodiode.

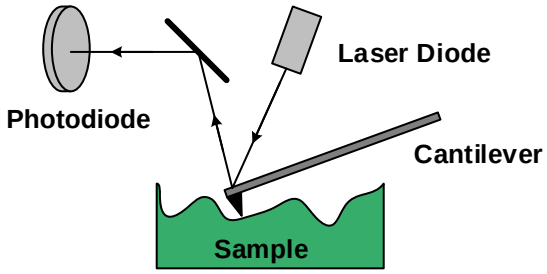

Figure 3.13: Schematic illustration of an atomic force microscope.

The AFM can operate in a number of modes including [5]:

- **Contact mode.** The probe tip is dragged across the surface and the resulting image is a topographical map of the sample surface. While this technique has been very successful for many samples, it has some drawbacks. The dragging motion of the probe tip, combined with adhesive forces between the tip and the surface, can damage both sample and probe and create artifacts in the data.
- **Tapping mode.** The tip is placed in contact with the surface to provide high resolution and then the tip is lifted off the surface to avoid dragging the tip across the surface. Tapping mode imaging allows high-resolution topographic imaging of sample surfaces that are easily damaged or otherwise difficult to image.
- **Non-contact mode.** The instrument senses van der Waal attractive forces between the surface and the probe tip held above the sample surface. Because, these forces are substantially weaker, non-contact mode provides lower resolution than either contact or tapping mode.

Laser scanning confocal microscope

The laser scanning confocal microscope (LSCM) is an essential tool for surface topographic imaging applications. The LSCM allows accurate nano-level measurements from

1 µm to 50 nm for both full-focus images and reliable 3D shape analysis. Observations can be made at room temperature without pre-processing of samples. These factors enable quick and accurate analysis of samples.

Figure 3.14 shows the structure of a laser scanning confocal microscope. The LSCM is built around a conventional light microscope and uses a laser rather than a lamp for a light source. As shown in Figure 3.14, light from one or more lasers passes through a pinhole, attenuated through an acousto-optic tunable filter (AOTF), bounces off a dichromatic mirror, and passes into the scanning unit. A scanned beam enters the back focal plane of the objective lens, which focuses the light at a point in the specimen. Any light coming back from the excitation of a fluorochrome at this point inside the specimen passes back through the objective lens and the scanning unit. Since this light is of longer wavelength than the excitation light, it passes through the dichromatic mirror, is further cleaned up by a barrier filter and it is eventually focused at the second pinhole. Any light that passes through the pinhole strikes a low noise photomultiplier detector, the signal from which subsequently passes to the computer imaging system of the confocal microscope [16, 17].

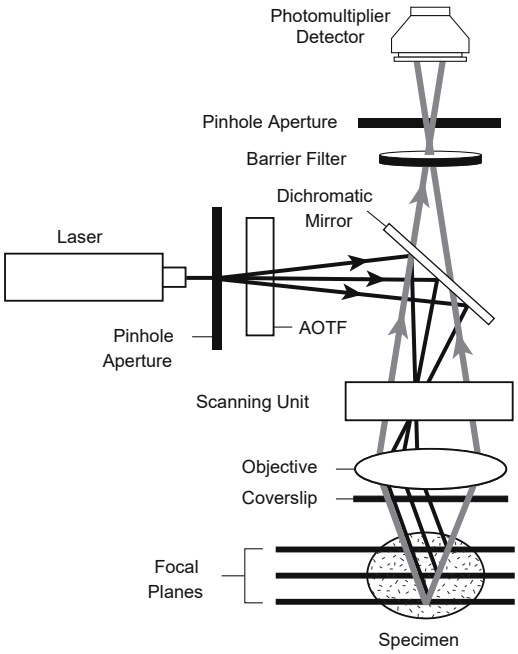

Figure 3.14: Schematic diagram of a laser scanning confocal microscope, adapted from Ref. [16].

3.3. Chemical and physical characterizations

Chemical and physical characterization techniques are based on similar principles: a primary electron, ion, or photon beam causes back-scattering or transmission of the in-

cident particles-waves or the emission of secondary particles/waves. The mass, energy, or wavelength of the emitted entities is characteristic of the target element or compound from which it originated. And their distribution can be mapped in the x-y plane and frequently also in the depth direction. Each of the techniques has particular strengths and weaknesses, and frequently more than one method must be used for unambiguous identification. Also, different techniques present various resolution capabilities. Electron beams can be focused to diameters as small as 0.1 nm. Ion beams cover the 1 to 100 μm range and X-rays typically have diameters of 100 μm and above. In this thesis, various analytical techniques, including electron-beam and X-ray techniques, are employed to investigate the structure and composition of samples.

3.3.1. Electron-beam techniques

Electron-beam techniques are summarized in Figure 3.15. Incident electrons are absorbed, emitted, reflected, or transmitted, and can, in turn, produce a variety of signals in forms of electrons, light, or X-ray. By registering these signals, we can obtain the structural and compositional information of the specimen. Herein, techniques including transmission electron microscopy (TEM), scanning electron microscopy (SEM), energy-dispersive X-ray spectroscopy (EDS), Auger electron spectroscopy (AES) are used in this thesis.

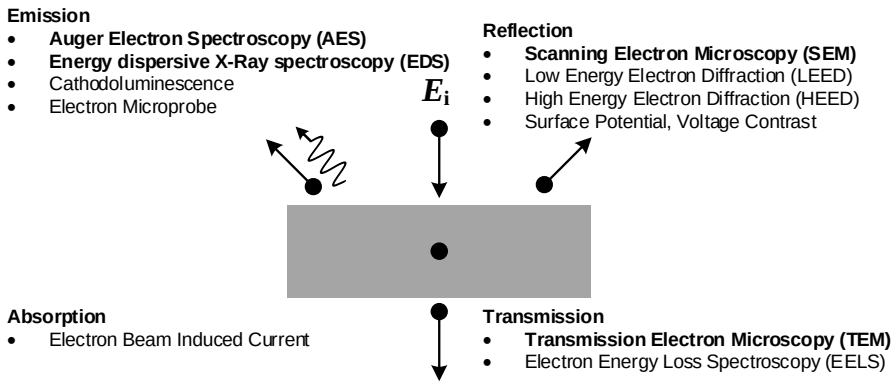

Figure 3.15: Electron-beam characterization techniques, reproduced from Ref. [5].

Transmission electron microscopy (TEM)

The shorter wavelength of electrons in electron microscopes which is about 10,000 times shorter than that of visible light, allows capabilities of electron microscopes to reveal ultra-fine details of material microstructure. The resolution of electron microscopes reaches the order of 0.1 nm if lens aberrations can be minimized. There are two main types of electron microscopes: transmission electron microscopes (TEM) and scanning electron microscopes (SEM). The optics of the TEM is similar to the conventional transmission light microscope, while that of SEM is more like that of scanning confocal laser microscopes. Here, the TEM technique is discussed.

Figure 3.16 shows the structure of a TEM, consisting of an electron gun, condenser lens, specimen stage, objective lens, and the projector lens. Electromagnetic lens for electron beam in the TEM. Electrons from an electron gun are accelerated to high voltages and focused on the specimen by the condenser lenses. The sample is placed on a small copper grid a few mm in diameter. The static beam has a diameter of a few microns. The sample must be sufficiently thin (a few tens to a few hundred nm) to be transparent to electrons.

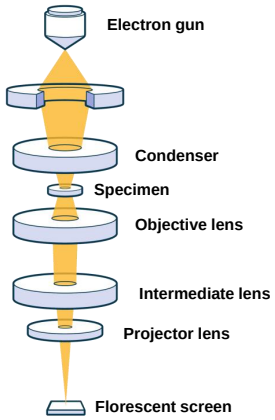

Figure 3.16: Structure of a transmission electron microscope, reproduced from Ref. [18].

The contrast in TEM relies on the deflection of electrons from their primary transmission direction when they pass through the specimen. The contrast is generated when there is a difference in the number of electrons being scattered away from the transmitted beam. There are two mechanisms by which electron scattering creates images:

- *Mass-density contrast.* The amount of electron scattering at any specific point in a specimen depends on the mass-density at that point. Thus, the difference in thickness and density in a specimen will generate variation in electron intensity received by an image screen in the TEM. Mass–density contrast is most important for non–crystalline, amorphous materials.
- *Diffraction contrast.* Electrons can be scattered collaboratively by parallel crystal planes. When the Bragg conditions are satisfied at certain angles between electron beams and crystal orientation, constructive diffraction occurs, and strong electron deflection in a specimen result. Hence, diffraction contrast is the primary mechanism of TEM image formation in crystalline specimens.

The diffraction contrast can generate bright-field (BF) and dark-field (DF) TEM images. Bright-field images are obtained by allowing only the transmitted beam to pass the objective aperture, while dark-field images are obtained by allowing one diffraction beam to pass the objective aperture.

Besides mass-density and diffraction contrasts which are amplitude contrast, the TEM can obtain phase contrast producing the highest resolution of lattice and structure images for crystalline materials. Phase contrast is often referred to as high-resolution transmission electron microscopy (HR-TEM). A crystalline specimen generates a phase difference between the transmitted and diffracted beams. An additional phase difference among the beams can be produced by the objective lens. Recombination of transmitted and diffracted beams will generate an interference pattern with periodic dark–bright changes on the image plane due to beam interference. And such an interference pattern is a fringe type revealing the periodic nature of a crystal [19].

Scanning electron microscopy (SEM)

The scanning electron microscope (SEM) examines micro-structure by scanning the surface of materials, similar to scanning confocal laser microscopes but with much higher resolution and much greater depth of field due to the employment of an electron beam. A scanning electron microscope consists of an electron gun and a series of electromagnetic lenses and apertures, as shown in Figure 3.17. An SEM image is formed by a focused electron beam that scans over the surface area of a specimen.

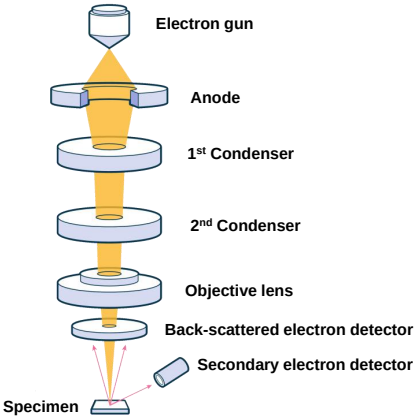

Figure 3.17: Structure of a scanning electron microscope, reproduced from Ref. [18].

In SEM, interactions between the electron beam and specimen at various depths can produce the various signal. Among them, back-scattered electrons (BSE) and secondary electrons (SE) are the two useful signal types for SEM. When electrons impinge on a solid, they lose energy by elastic scattering (change of direction with negligible energy loss) and inelastic scattering (energy loss with negligible change in direction). Elastic scattering is caused mainly by interactions of electrons with nuclei and is more probable in high atomic number materials and at low beam energies. Back-scattered electrons are produced by the elastic scattering. In contrast, inelastic scattering is caused mainly by scattering from valence and core electrons and produces the secondary electrons which

are electrons ejected from atoms in the specimen. The SEM images formed by back-scattered electrons and secondary electrons reveal different contrast of the specimen:

- *Topographic contrast.* Topographic contrast in an SEM refers to variation in signal levels that correspond to variation in geometric features on the specimen surface. Commonly, topographic images are obtained by operating an SEM in the SEI(secondary electron imaging) mode.

- *Compositional contrast.* Compositional contrast refers to the variation in gray levels in an SEM image that corresponds to variation in chemical composition in a specimen. Back-scattered electrons are mainly used to observe the compositional differences of the specimen. The origin of compositional contrast arises because the capability of back-scattered electrons to escape from the specimen depends on the atomic numbers of the specimen atoms. An area in a specimen containing chemical elements with a higher atomic number will generate more back-scattered electrons, which will be collected by a detector and produces a brighter area in the SEM image.

Energy dispersive X-Ray spectroscopy (EDS)

Besides back-scattered electrons and secondary electrons, the characteristic X-ray is also collected to reveal the specimen information by the technique of energy dispersive X-Ray spectroscopy (EDS). The EDS is commonly included as a part of SEM and TEM. And it allows elemental analysis while examining the microstructure of materials.

The EDS method consists of an electron bombardment of the sample and X-ray emission from the sample, as shown in Figure 3.18. A primary electron beam strikes the specimen. The characteristic X-ray is caused by the interaction of the primary electrons with inner-shell electrons. Incident electrons eject electrons from one of the inner atomic shells with electrons from higher-lying shells dropping into the vacancies created by the ejected electrons. It caused the emission of the characteristic X-ray with wavelengths practically independent of the physical or chemical state of the emitting atom. The number and energy of the characteristic X-rays emitted from a specimen can be measured by an energy-dispersive spectrometer. As the energies of the X-rays are characteristic of the difference in energy between the two shells and of the atomic structure of the emitting element, EDS allows the elemental composition of the specimen to be measured.

Auger electron spectroscopy (AES)

Besides characteristic X-ray, the electron-specimen interactions can also produce Auger electrons, as shown in Figure 3.19. When a high-energy electron (or X-ray photon) strikes an inner shell electron of an atom, the energy of the incident particle can be high enough to knock out the inner shell electron. Thus, the atom becomes ionized and in an excited state. The atom will quickly return to its normal state after refilling the inner electron vacancy with an outer shell electron. In the meantime, the energy difference between the outer shell electron and the inner shell may cause the emission of an Auger electron from an electron shell. The kinetic energy of an Auger electron is approximately equal to the energy difference between binding energies in the electron shells involved in the Auger process.

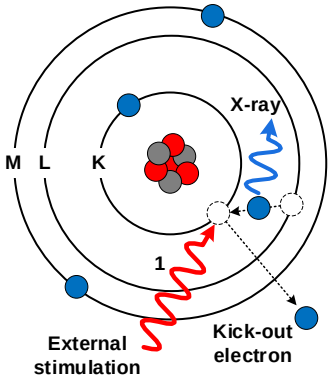

Figure 3.18: Electronic processes of energy dispersive X-Ray spectroscopy.

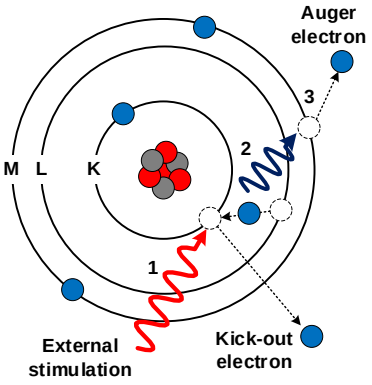

Figure 3.19: Principle of Auger electron spectroscopy. An illustration of *KLM* Auger transition, where *K* represents the core level hole, *L* is the relaxing electron's initial state, *M* represents the emitted electron's initial energy state.

Auger electron spectroscopy (AES) identifies chemical elements by measuring the kinetic energies of Auger electrons. In an AES spectrum, an individual kinetic energy peak from an Auger electron is marked with an elemental symbol and subscripts indicating the electron shells or sub-shells involved, for example, a *KLM* Auger transition illustrated in Figure 3.19. A typical AES spectrum is a plot of intensity (most commonly, the first derivative of intensity) versus kinetic energy. AES is widely used in measuring material composition. In addition, sputtering is sometimes used with AES to perform depth profiling measurements.

Figure 3.20 summaries the range and spatial resolution of back-scattered electrons, secondary electrons, characteristic X-rays, and Auger electrons for electrons incident on a solid. Commonly, more than one above-mentioned techniques are used to characterize the materials, in order to provide a comprehensive physical and chemical information of the materials.

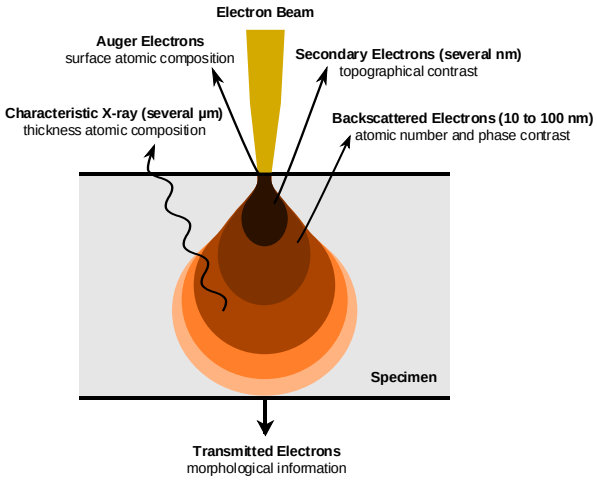

Figure 3.20: Depth of quantum emission and spatial resolution, reproduced from Ref. [20].

3.3.2. X-Ray diffraction techniques

Similar to the electron beam, X-ray interactions with the solid also provide useful information on the materials. Incident X-rays are absorbed, emitted, reflected, or transmitted and can, in turn, cause electron emission. In this thesis, we used X-ray diffractometry (XRD) to study crystal structures and phases of samples.

Consider a perfect crystal arranged to diffract monochromatic X-rays of wavelength λ from lattice planes spaced d, as shown in Figure 3.21. The X-rays are incident on the sample at an angle θ. Note that the θ angle is not the angle between the incident beam and specimen surface; rather it is the angle between the incident beam and the crystallographic plane that generates diffraction. The primary beam is absorbed by or transmitted through the sample. Only the diffracted beam is recorded on the film. The diffracted beam emerges in a few specific directions, determined by Bragg's law [5],

$$n\lambda = 2d\sin\theta, \tag{3.33}$$

where λ is the wavelength of the beam, n is any integer, d is the spacing between diffracting planes, and θ is the incident angle.

A diffractometer records changes of diffraction intensity with 2θ. The diffractometer records the diffraction intensity starting from a low 2θ and ending at a high 2θ. A number of intensity peaks located at different 2θ provide a fingerprint for the crystalline specimen. Each peak represents diffraction from a certain crystallographic plane. Matching an obtained peak spectrum with a standard spectrum enables the identification of the crystalline substances in a specimen [19].

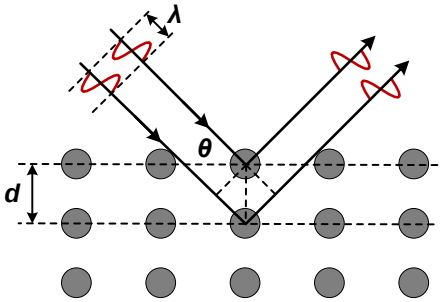

Figure 3.21: Principle of X-ray diffraction.

References

[1] K. Wasa, I. Kanno, and H. Kotera, *Handbook of sputter deposition technology: Fundamentals and applications for functional thin films, nano-materials and MEMS* (William Andrew, 2012).

[2] O. Chapurin and A. Smolyakov, *On the electron drift velocity in plasma devices with* $\boldsymbol{E} \times \boldsymbol{B}$ *drift,* Journal of Applied Physics **119**, 243306 (2016).

[3] K. Wasa, M. Kitabatake, and H. Adachi, *Thin film materials technology: Sputtering of control compound materials* (Springer Science & Business Media, 2004).

[4] J. George, *Preparation of thin films* (CRC Press, 1992).

[5] D. K. Schroder, *Semiconductor material and device characterization* (John Wiley & Sons, 2015).

[6] C. V. Raman and K. S. Krishnan, *A new type of secondary radiation,* Nature **121**, 501 (1928).

[7] E. Smith and G. Dent, *Modern Raman spectroscopy: A practical approach* (Wiley Online Library, 2005).

[8] R. R. Jones, D. C. Hooper, L. Zhang, D. Wolverson, and V. K. Valev, *Raman techniques: Fundamentals and frontiers,* Nanoscale research letters **14**, 1 (2019).

[9] T. Schmid and P. Dariz, *Raman microspectroscopic imaging of binder remnants in historical mortars reveals processing conditions,* Heritage **2**, 1662 (2019).

[10] Toommm, *Schematic of one possible dispersive raman spectroscopy setup,* (2019), `https://commons.wikimedia.org/w/index.php?curid=80885633`.

[11] H. Fujiwara and R. W. Collins, *Spectroscopic Ellipsometry for Photovoltaics: Volume 1: Fundamental Principles and Solar Cell Characterization*, Vol. 212 (Springer, 2019).

[12] F. Padera, *Measuring absorptance (k) and refractive index (n) of thin films with the Perkinelmer Lambda 950/1050 high performance UV-Vis/NIR spectrometers,* PerkinElmer, Inc (2013).

[13] E. H. Hall *et al.*, *On a new action of the magnet on electric currents,* American Journal of Mathematics **2**, 287 (1879).

[14] O. Philips'Gloeilampenfabrieken, *A method of measuring specific resistivity and hall effect of discs of arbitrary shape,* Philips Res. Rep **13**, 1 (1958).

[15] D. A. Neamen, *Semiconductor physics and devices: basic principles* (New York, NY: McGraw-Hill, 2012).

[16] S. W. Paddock and K. W. Eliceiri, *Laser scanning confocal microscopy: History, applications, and related optical sectioning techniques,* (Springer New York, New York, NY, 2014).

[17] S. W. Paddock, *Principles and practices of laser scanning confocal microscopy,* Molecular Biotechnology **16**, 127 (2000).

[18] N. Gleichmann, *SEM vs TEM,* (2020), https://www.technologynetworks.com/analysis/articles/sem-vs-tem-331262.

[19] Y. Leng, *Materials characterization: introduction to microscopic and spectroscopic methods* (John Wiley & Sons, 2009).

[20] Claudionico, *Electron interaction with matter,* (2015), https://commons.wikimedia.org/wiki/File:Electron_Interaction_with_Matter.svg.

4

Sputtered $BaSi_2$ Films

Abstract

In this chapter, $BaSi_2$ thin films is fabricated via an industrially applicable sputtering process and the mechanism of its structural transformation is studied. Poly-crystalline $BaSi_2$ thin films are obtained through the sputtering process followed by a post-growth annealing treatment. The crystalline quality and phase composition of sputtered $BaSi_2$ are characterized by Raman spectroscopy and X-ray diffraction. A higher annealing temperature can promote crystallization of $BaSi_2$, but also causes an intensive surface oxidation and $BaSi_2/SiO_2$ interfacial diffusion. As a consequence, an inhomogeneous and layered structure of $BaSi_2$ is revealed by Auger electron spectroscopy and transmission electron microscopy. The structural transformation process of sputtered $BaSi_2$ films then is studied by the Raman depth-profiling method, and all of the above observations come to an oxidation-induced structure transformation mechanism. It interprets interfacial phenomena including surface oxidation and $BaSi_2/SiO_2$ inter-diffusion, which lead to the inhomogeneous and layered structure of sputtered $BaSi_2$. The mechanism can also be extended to epitaxial and evaporated $BaSi_2$ films. Such fundamental knowledge on structural transformations and complex interfacial activities is significant for further quality control and interface engineering on $BaSi_2$ films toward high-efficiency solar cells.

Parts of this chapter have been published in ACS Applied Energy Materials, **1**, 3267 (2018) [1].

4.1. Introduction

Sustainability, industrial ecology, and cost efficiency are regarded as key criteria guiding the development of the next-generation photovoltaic materials [2–5]. Among a broad range of materials, the semiconducting barium disilicide ($BaSi_2$) has gained an increasing interest as a promising light-absorbing material toward high-performance thin-film solar cells [6, 7]. Despite the huge promise that $BaSi_2$ holds, the material is confronted with potential technological and scientific issues related to the material synthesis and quality control, hindering its deployments from the material to cost-effective solar cells.

Low-cost synthesis routes of $BaSi_2$ come to the forefront. In fact, high-quality $BaSi_2$ films, which achieves efficient solar cell device, have only been accomplished by the molecular beam epitaxy (MBE) technique [8, 9]. The distinct atomic-level film control advantage allows MBE a pioneering position in high-quality material development. However, such an advantage always involves prohibitively expensive processes and the consequently high manufacturing cost, inhibiting further practical applications. To this end, great efforts have been put into industrially applicable and commercially realistic processes for high-quality $BaSi_2$ fabrications. Besides the chemical vapor deposition (CVD) technique [10], more attention is focused on alternative low-cost physical vapor deposition (PVD) approaches, such as thermal evaporation and sputtering [11–15]. $BaSi_2$ thin films on various substrates with a high deposition rate up to 840 nm/min have been achieved via the thermal evaporation technique, presenting comparable quality to epitaxial films [11, 14, 16, 17]. Nevertheless, evaporation-source-related issues, including equilibrium vapor pressure difference and possible reactions with tungsten boat, increase difficulties in stoichiometry and further quality control of evaporated $BaSi_2$ [7]. In this regard, the sputtering technique, another feasible option for thin-film fabrications, is taken into consideration. Besides the high deposition rate and elimination of ultra-high vacuum (UHV) equipment, the sputtering process exhibits an excellent stoichiometry control for compound material depositions. However, limited knowledge on sputtered $BaSi_2$ films currently cannot support the further advancement from the material to practical PV devices [12, 13, 18, 19]. Fundamental researches on synthesis and characterizations of sputtered $BaSi_2$ films remain yet need to be carried out.

The other crucial issue is the material quality control of $BaSi_2$ (especially at interfacial regions). The reactivity with oxygen and moisture does add the difficulties to quality control at the air/$BaSi_2$ interface [7, 20–22]. The formed oxide layer consequently hinders the minority carrier (hole) transport with a barrier height of 3.9 eV [22]. The involved high-temperature conditions (Table S1) can further aggravate air/$BaSi_2$ interfacial oxidation. Besides the air/$BaSi_2$ interface, the $BaSi_2$/solid (substrate) interface also experiences the atomic inter-diffusion. Such inter-diffusion alters the stoichiometry, results in defective phases, and then degrades the film quality [23, 24]. In fact, those interfacial phenomena both at air/$BaSi_2$ and $BaSi_2$/substrate interfaces increase difficulties on material quality control. Even though some approaches of avoiding deleterious interfacial activities have been put forward [8, 25, 26], the concealed mechanisms of these interactions are still not well-documented, especially for the sputtering case. A better understanding of those interfacial activities is a key goal that helps in developing quality-optimization strategies [20, 27], and designing solar cell architectures [28, 29].

In this chapter, we present a $BaSi_2$ thin film synthesis route via industrially applicable sputtering technique and reveal the structure transformation mechanism of $BaSi_2$ at the high-temperature treatment. Poly-crystalline $BaSi_2$ thin films are obtained through the radio frequency (RF) sputtering process with a post-growth annealing treatment. Higher annealing temperatures can enhance the crystallization of $BaSi_2$, but also induces an inhomogeneous and layered structure. Toward this, an oxidation-induced structure transformation mechanism is proposed based on structural and interfacial observations and thermodynamic calculations. The knowledge regarding interfacial interactions and the structural transformation of $BaSi_2$ films serves as the foundation for future researches on quality-control and interface-engineering strategies of $BaSi_2$ films toward solar cell applications.

4.2. Experimental

4.2.1. Film synthesis

An RF magnetron sputtering set-up (Kurt J. Lesker) was applied for the growth of $BaSi_2$ films. A stoichiometric ceramic $BaSi_2$ target was installed. After the deposition chamber was pumped to less than 2×10^{-4} Pa, Ar gas flow was introduced into the chamber. The background pressure was maintained at 1 Pa during the whole growth process. The plasma power of 50 W was applied. Prior to the growth, a pre-sputtering process was carried out for 10 min. The samples were deposited either on glass or silicon wafer substrates. After the sputtering process, the deposited $BaSi_2$ films were subsequently annealed for 90 min in a nitrogen atmosphere. Annealing temperatures ranged from 550 to 750 °C with a step of 50 °C.

4.2.2. Characterizations

The thickness of the as-deposited sample was measured by spectroscopic ellipsometry (SE, J.A.Woollam Co.). Raman spectra were acquired by an InVia Raman Microscopy (Renishaw) with excitation wavelengths of 514 and 633 nm. The XRD patterns were obtained by an automatic powder X-ray diffractometer X'Pert Pro equipped with an ultrafast linear semiconductor detector PIXcel and on a point proportional detector. Cu Kα radiation (λ = 0.154 nm) was used as an X-rays source. The X-ray incidence angle θ was fixed at 0.5°. The wavelength-depended reflectance and transmittance were measured by PerkinElmer Lambda 950 spectrometer. Elemental composition analysis was carried out in Jeol JAMP 9510-F Auger Microprobe at 10 keV energy with a tilt angle of 30°. During sputtering cycles, 1000 eV Ar^+ ions were utilized. The cross-section images and electron diffraction patterns were acquired by a transmission electron microscope (TEM, JEOL JEM-2200FS).

4.3. Results and discussion

4.3.1. Fabrications of sputtered $BaSi_2$ thin films

$BaSi_2$ films are sputtered on $10 \times 10 cm^2$ alkali-free glass with target-substrate distances d_{T-S} ranging from 110 to 165 mm. Their thickness distribution are shown in Figure 4.1. The maximum film thickness deviation from center to edge is approximately 55% (d_{T-S}

= 110 nm). Enlarging the spacing between the target and substrate d_{T-S} guarantees a more thickness-uniform film. However, it would, on the other hand, pose a detrimental influence on the film deposition rate (R_d). The centric R_d of the samples deposited with d_{T-S} = 135 mm (6.6 nm) and 160 mm (4.4 nm/min) are nearly half and one third, respectively, of sample deposited with d_{T-S} = 110 mm (11.1 nm/min). A lower deposition rate means poorer product efficiency, lower target utility, and higher film cost. Therefore, the d_{T-S} = 135 mm was applied for the $BaSi_2$ sputtering process, ensuring both uniformity of thickness in centric area (~20 mm away from the center) and a relatively high deposition rate.

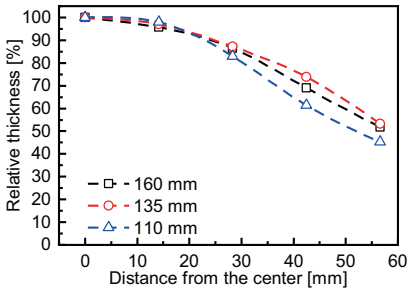

Figure 4.1: The relative film thickness normalized with the centric thickness of the film as the function of the distance from the substrate center. Distances from the target to the substrate (d_{T-S}), i.e., 160, 135 and 110 mm, were utilized.

The amorphous instead of preferably crystalline state of as-deposited $BaSi_2$ (see Raman spectrum in Figure 4.2) prohibits its direct employment into practical thin-film solar cells. Thus, a subsequent thermal crystallization process was implemented. As-deposited samples were annealed at temperatures (T_a) ranging from 550 to 750 °C. Fused silica substrates here were utilized due to the high T_a. Annealing duration (t_a) was fixed at 90 min to ensure full crystallization. Here, samples are denoted as $BaSi_2$-T_a/t_a, *e.g.*, $BaSi_2$-RT/0 (as-deposited), and $BaSi_2$-650/90 (T_a = 650 °C and t_a = 90 min).

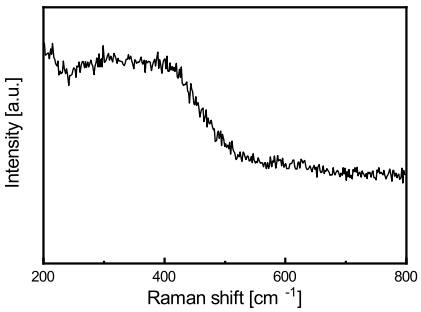

Figure 4.2: Raman spectrum of the as-deposited $BaSi_2$ film on the quartz substrate.

Figure 4.3 shows the Raman spectra of annealed $BaSi_2$ films acquired by a 633-nm red laser. Typically, there are five Raman bands corresponding to the vibration of $[Si_4]^{4-}$ cluster in $BaSi_2$, which are assigned to five vibrational modes, namely F_g at ~276 cm^{-1}, E_g at ~293 cm^{-1}, E_g + F_g at ~355 cm^{-1}, F_g at ~376 cm^{-1}, and A_g at ~486 cm^{-1} [30, 31]. As shown in Figure 4.3, only $BaSi_2$-650/90 and -700/90 display sharper bands with fairly strong intensities, while bands of other samples annealed at lower T_a ($BaSi_2$-550/90 and -600/90) present less distinguishable vibration bands.

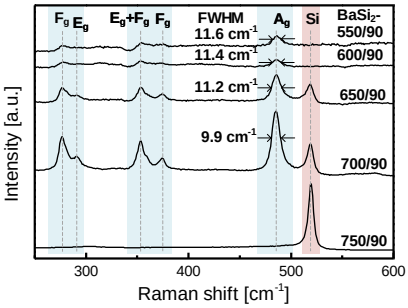

Figure 4.3: Raman spectra of annealed $BaSi_2$ (collected from the film side).

Full width at half-maximum (FWHM) values of the intensity-strongest A_g band (~486 cm^{-1}) are calculated to quantitatively study the crystalline quality. A lower FWHM value is referred to a better crystalline quality. As shown in Figure 4.3, FWHM values decreased from 11.6 to 9.9 cm^{-1} by increasing T_a from 550 to 700 °C. It implies an enhancement of crystallization degree at higher T_a (but lower than 750 °C). Nevertheless, the higher T_a (≥ 650 °C), on the other hand, causes the formation of Si nanocrystals (NCs), indicated by the band at ~519 cm^{-1} [32, 33]. Even worse is the sample $BaSi_2$-750/90, which only presents a Si NCs band.

It should be emphasized that Raman spectroscopy only reflects the superficial structure information due to the limited laser penetration depth. To obtain a deeper insight into sample structures, a Raman depth profiling method is then established by applying both red (633 nm) and green (514 nm) lasers to measure either from film or substrate side as shown in Figure 4.4.

Accordingly, an inhomogeneous structure of $BaSi_2$-650/90 is portrayed by Figure 4.5. An obvious change of Raman spectra, from the surface to bottom, can be observed. Intensity ratios between A_g and Si bands I(A_g)/I(Si) are calculated to roughly quantify concentrations ratio between $BaSi_2$ and Si NCs within detected regions. Here, we see an increase of I(A_g)/I(Si) from 0.64 at top-surface region to 2.46 at the buried bottom, implying a composition evolution. To be explicit, less $BaSi_2$ remains at the surface region, while Si NCs are inclined to form and accumulate at the surface.

Figure 4.6 presents the XRD patterns of annealed samples. Most of the strong diffraction peaks are related to orthorhombic $BaSi_2$, which is consistent with the Raman spectroscopy and further confirms $BaSi_2$ crystallization. Besides the orthorhombic phase, cubic and hexagonal $BaSi_2$ can also be observed. Cubic and hexagonal phases are reported to be metastable in ambient pressure, and form at high-temperature-pressure

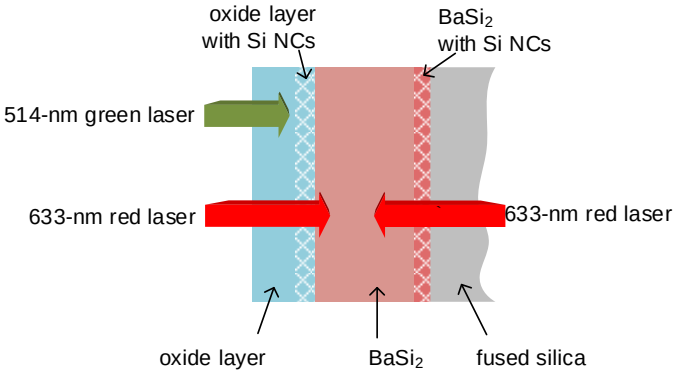

Figure 4.4: Schematic diagram of penetration depths 633- and 514-nm Raman lasers into the film.

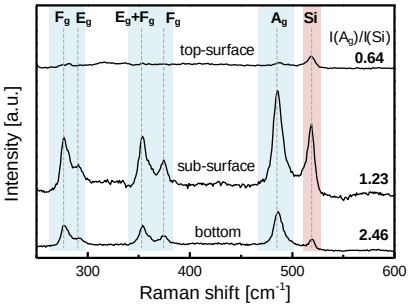

Figure 4.5: Raman depth profile of the sample $BaSi_2$-650/90.

conditions (up to 1000 °C and 1 GPa) [34–36]. The existence of those phases may result from the high energy of charged particles (Ba and Si) in the sputtering process. The existence of other low-concentration (less than 7% of the analyzed film) barium silicon-compounds such as Ba_3Si_3 can also be noticed, the diffraction peak intensities of which decreases with the increase of T_a. Formation mechanisms of those phases and compositions remain to be uncovered for the goal of obtaining single-phase orthorhombic $BaSi_2$.

It is worth to note that $BaSi_2$ diffraction peaks can also be observed in $BaSi_2$-750/90, in which sample $[Si_4]^{4-}$ Raman vibrational bands cannot be detected as shown in Figure 4.3. It suggests the existence of a $BaSi_2$ layer that is sandwiched between two thick non-$BaSi_2$ layers in the $BaSi_2$-750/90. The possible amorphous and/or micro-crystalline state of non-$BaSi_2$ layers prohibits their being detected by XRD nor Raman. Additionally, the absence of $[Si_4]^{4-}$ Raman bands indicates that the higher annealing is presumed to enhance the non-$BaSi_2$ layer growth.

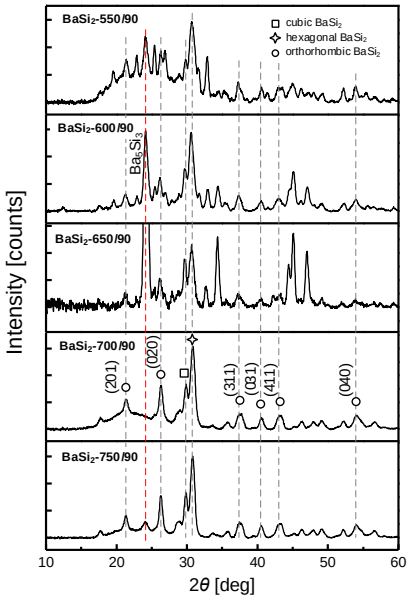

Figure 4.6: XRD patterns of annealed $BaSi_2$ films.

Auger electron spectroscopy (AES) was employed to determine the elemental composition and structure. Due to the requirement of conducting substrates for measurements, crystalline silicon (c-Si) wafers instead of fused silica substrates were utilized here. Prior to the $BaSi_2$ growth, c-Si substrates were coated with interlayers, including SiO_2, *p*-, and *n*-type poly-crystalline silicon (poly-Si) [37]. Employments of interlayer can avoid the influence of c-Si orientation on film growth, and make it possible to study the interactions at $BaSi_2$/poly-Si and $BaSi_2/SiO_2$ interfaces.

Figure 4.7 displays the depth elemental concentrations of the as-deposited $BaSi_2$ film with a structure of ($BaSi_2$-RT/0)/SiO_2/c-Si. The layer structure is quite distinguishable, including the native oxide layer (Layer I, *ca.* 5 nm), the $BaSi_2$ (Layer II, *ca.* 450nm), the SiO_2 interlayer (Layer III), and the c-Si substrate (Layer IV). A constant ratio of Ba:Si = 1:2 throughout the Layer II reflects the excellent stoichiometry control of the sputtering technique. Besides, no obvious inter-diffusion phenomenon can be observed within the $BaSi_2$-RT/0.

However, the existence of ~10% oxygen that uniformly distributes throughout the Layer II can also be observed. There are three potential sources of the oxygen, including oxygen diffusing from SiO_2, the native oxidation, and the residual oxygen in the chamber. Firstly, thermodynamic non-equilibrium states of atoms during the sputtering process can induce the oxygen diffusion at the $BaSi_2/SiO_2$ interface. On the other hand, the amorphous nature of the as-deposited film, containing a high density of defects and disorder structures, may enhance the chance for oxygen (in the air) bonding with Ba and Si during the sample storage. However, the absence of an oxygen concentration gradi-

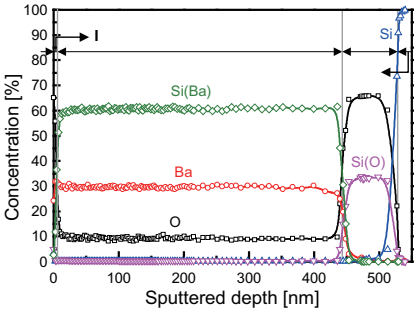

Figure 4.7: AES elemental concentration depth profiles of as-deposited $BaSi_2$ on the SiO_2/c-Si substrate.

ent near $BaSi_2/SiO_2$ and air/$BaSi_2$ interfaces suggests that oxygen is less likely to originate from the two above-discussed sources. Another possible source is the residual O_2 and moisture in the deposition chamber. Given that the base pressure of the deposition chamber is around 2×10^{-4} Pa, the O_2 partial pressure, as a result, is in the order of 10^{-5} Pa. It ensures a sufficient number of oxygen atoms for incorporation in $BaSi_2$ films. Due to its incorporation with $BaSi_2$ during deposition, the oxygen here is denoted as internal O. Not only in the case of sputtering, similar oxygen incorporation phenomena have also been reported with epitaxial and evaporated $BaSi_2$, which are executed at even lower pressures (on the order of 10^{-5} Pa) [26, 38, 39]. The existence of those internal O atoms does not alter the composition uniformity of sputtered $BaSi_2$. Nevertheless, it is currently hard to assert the effects of internal O on $BaSi_2$ properties, which need further study.

Figure 4.8 shows the elemental structure of the $BaSi_2$-650/90 on the same SiO_2/c-Si substrate. $BaSi_2$-650/90 exhibits an inhomogeneous structure in which a Si-rich $BaSi_2$ (Layer IV) is sandwiched between an oxide layer (Layers I-III) and an inter-diffusion layer (the interfacial region between Layers IV and V). Such a layered structure is consistent with Raman and XRD observations.

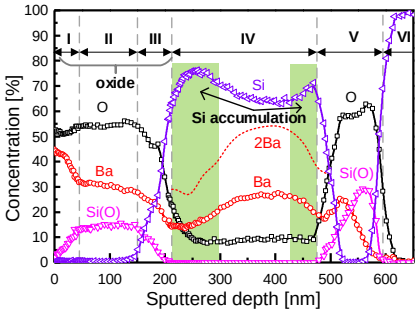

Figure 4.8: AES elemental concentration depth profiles of $BaSi_2$-650/90 on the SiO_2/c-Si substrate.Si atoms bonded with Ba or O are marked as Si(Ba) and Si(O), respectively.

A high concentration of O at the surface region is the outcome of intensive surface

oxidation. We denote the O here as external O to distinguished from the O incorporating to $BaSi_2$ during the deposition. The oxide layer (holding a high O concentration) can be further divided into three sub-layers illustrated in Figure 4.8. Within the Layers I and II, only Si(O), Ba, and O can be detected, indicating the composition of SiO_2 and BaO. The concentration of SiO_2 increases throughout the Layer I, and eventually reaches a BaO:SiO_2 ratio of 2:1 (Layer II). The composition transition starts from the Layer III (near the oxide/$BaSi_2$ interfacial region). Accompanying with the upward Si curve in the Layer III, both BaO and SiO_2 start to decrease while keeping BaO:SiO_2 = 2:1. The accumulation of Si in the Layer III results in the formation of Si NCs (Figure 4.8). Hence, the oxide layer (Layers I-III) presents a composition of BaO and SiO_2, together with Si NCs. For a higher annealing temperature, i.e., 750 ºC, can promote the surface oxidation inducing a thicker oxide layer containing higher-concentration Si NCs. It explains the Raman spectrum of $BaSi_2$-750/90 (Figure 4.3), which only holds a Si NCs peak.

The phenomena of Si accumulation can also be observed on the other side of the 'sandwich', indicated in Figure 4.8. It can be the consequence of the diffusion of Ba into the SiO_2 interlay (Layer V). Ba unveils a relatively high diffusivity into SiO_2 and distributes throughout the Layer V. Those accumulated Si also formed Si NCs, which is consistent with the Raman spectrum obtained from the substrate side (Figure 4.5). Such Ba diffusion can be effectively suppressed by poly-Si interlayers, as shown in Figure 4.9. No Ba presents in the *n*-type poly-Si layer (Layer VI in Figure 4.9). However, there is a relatively high concentration of O in the Layer V. The absence of Si(O) here implies that it is a Ba-Si-O complex oxide rather than a mixture of SiO_2 and BaO. O atoms here can also be the internal O, which may originate from the residual oxygen in the deposition chamber as well as O_2 and/or oxygen-containing groups adhering to the poly-Si surface. The case of *p*-type poly-Si (B-doped) is almost similar as presented in Figure 4.10, except for the disappearance of B within the poly-Si interlayer (and/or B concentration is under detection limit).

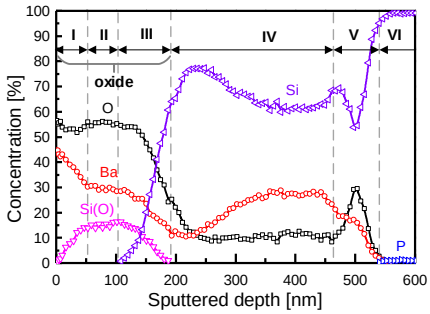

Figure 4.9: AES elemental concentration depth profiles of $BaSi_2$-650/90 on the *n*-type poly-Si/c-Si substrate.Si atoms bonded with Ba or O are marked as Si(Ba) and Si(O), respectively.

The surface oxidation together with interfacial diffusion phenomena leaves a Si-rich $BaSi_2$ layer in the center of the 'sandwich'. As illustrated in the Figure 4.8, Si atomic concentration is far more than twice that of Ba (2Ba curve), especially near the interfacial (oxide/$BaSi_2$ and $BaSi_2$/SiO_2) regions. Not only the Si accumulations but also the Ba

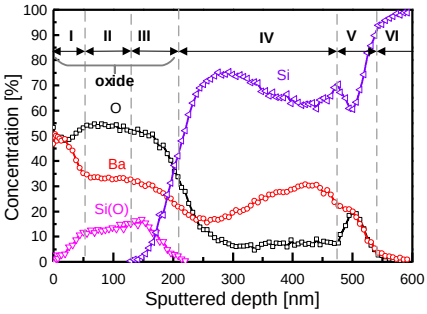

Figure 4.10: AES elemental concentration depth profiles of $BaSi_2$-650/90 on the *p*-type poly-Si/c-Si substrate. Si atoms bonded with Ba or O are marked as Si(Ba) and Si(O), respectively.

movement can be observed. Comparing the overall Ba distribution in Figure 4.7 and 4.8, the trend that Ba moves to the surface and substrate side after annealing is quite noticeable. Nevertheless, the internal oxygen still remains a constant concentration of nearly 10% after annealing throughout the core region of the Layer IV (250 – 450 nm). It suggests a stable structure of O-incorporated $BaSi_2$ in high temperatures. Besides, it needs to emphasize that it is external O (from annealing atmosphere and SiO_2 substrate) rather than internal O (from residual air in the deposition chamber) that alters the composition uniformity of sputtered $BaSi_2$. Further attempts to obtain uniform sputtered $BaSi_2$ should be focused on the anti-oxidation/diffusion layer development. And poly-Si (and/or a-Si) can be regarded as a potential candidate.

Another phenomenon that should not be neglected is the slight shift of the boundary between the Layers II and III (Figure 4.8, 4.9, and 4.10), while the thickness of the oxide layer keeps constant (~200 nm). The cross-section transmission electron microscopy (TEM) image in Figure 4.11a clues the variation. The Layer I shows a relatively distinguishable and flat boundary with a thickness of ~50 nm. However, Layers II and III almost merge together and are hard to be distinguished from the $BaSi_2$ layer. The variation in grayscale near the oxide/$BaSi_2$ interfacial region suggests the non-uniform composition and/or structure distribution in this region. Therefore, there is a high chance to collect AES depth profiles with different sub-layers thickness. Additionally, the high-resolution TEM (HR-TEM) image of $BaSi_2$ bulk (Figure 4.11c) together with the electron diffraction (ED) pattern (Figure 4.11b), reveal the poly-crystalline and multi-phase structure of $BaSi_2$-650/60.

Figure 4.12 present the wavelength-depended reflectance curves of $BaSi_2$-650/90, -700/90 and -750/90. Interference fringes in reflectance curves can result from the layered structure of high-temperature-annealed $BaSi_2$ films. Interference peak position shifts with the increase of T_a can also be observed. It can be caused by the oxide layer growth (bulk $BaSi_2$ thickness decreasing) at higher T_a. Besides, increasing T_a from 650 to 700 °C leads a drastic enhancement of the transmittance (Figure 4.13). It can be interpreted by the improvement of $BaSi_2$ crystalline quality at higher T_a (see Figure 4.3) and/or oxide layer (SiO_2 and BaO) growth.

Figure 4.14 shows absorptance curves. $BaSi_2$ films exhibit high absorptance compar-

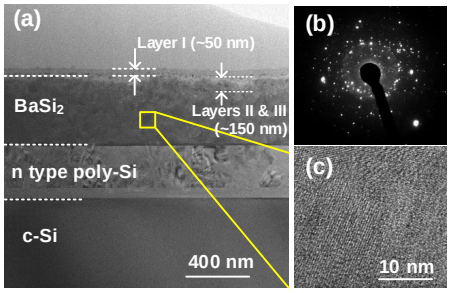

Figure 4.11: (a) TEM cross-section image, (b) ED pattern, and (c) HR-TEM image of the ($BaSi_2$-650/90)/*n*-type poly-Si/c-Si sample.

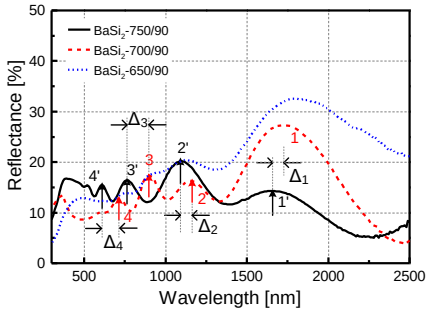

Figure 4.12: Wavelength-dependent reflectance curves of annealed $BaSi_2$ thin films. Interference peak position shifts, *i.e.*, Δ_1, Δ_2, Δ_3, and Δ_4, are illustrated.

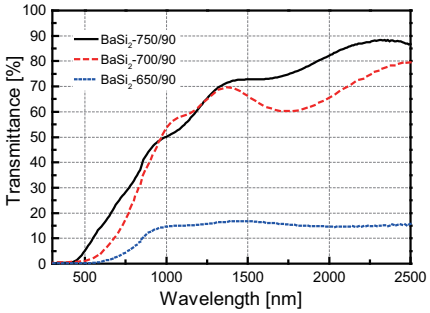

Figure 4.13: Wavelength-dependent transmittance curves of annealed $BaSi_2$ thin films.

ing to hydrogenated nanocrystalline silicon (nc-Si:H). However, metallic and/or defective phases (Figure 4.6) induce an absorptance tail in the long-wavelength range. And it can be attenuated by increasing T_a. $BaSi_2$-700/90 and -750/90 then present obvious absorption edges. However, higher T_a up 750 °C, in turn, reduces the absorptance in the visible wavelengths range. The absorptance difference between $BaSi_2$-700/90 and $BaSi_2$-750/90 reaches to a maximum at a wavelength around 500 nm, which is near the

absorptance peak of nc-Si:H (Figure 4.14). Hence, such absorptance difference can be a consequence of formations of higher-concentration of Si NCs and/or the thicker oxide layer at a higher T_a. Those optical properties are also consistent with the appearances of samples (Figure 4.15a-d), including the change of the transparency and brownish color (annealed samples).

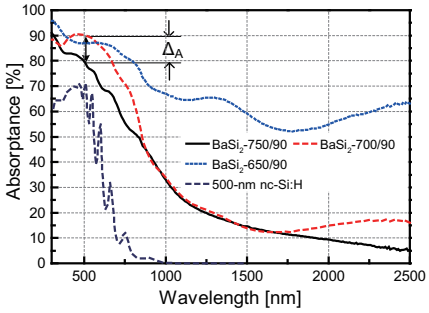

Figure 4.14: Wavelength-dependent absorptance curves of annealed $BaSi_2$ thin films. The absorptance was calculated as follows: absorptance(%) = 100% – reflectance(%) – transmittance(%). The simulated absorptance curve of 500 nm thick nc-Si:H film is presented as the reference.

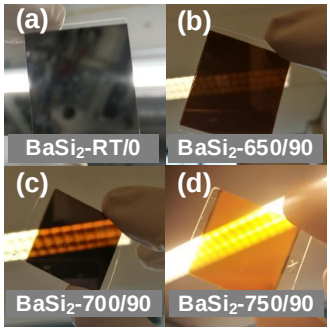

Figure 4.15: Photo images of (a) $BaSi_2$-RT/0, (b) $BaSi_2$-650/90, (c) $BaSi_2$-700/90, and (d) $BaSi_2$-750/90.

Even though optical characterizations provide some information of annealed samples, it is hard to obtain the exact optical properties of bulk $BaSi_2$ with the existence such layered structure (oxide and Si NCs). The same goes for the electrical properties. The thick oxide layer at the front side inhibits proper measurement due to high contact resistance.

4.3.2. Investigation on sputtered $BaSi_2$ annealing process

A deeper understanding on the mechanism of above-discussed structural transformation then is essential for sputtered $BaSi_2$ quality-optimization and further applications. Hence, the annealing process is temporally investigated by the established Raman depth-profiling method (only 633-nm laser is employed here). Raman depth profiles of $BaSi_2$-

650/1, -650/5, and -650/10 are presented in Figure 4.16a-c, respectively. Vibration bands of $[Si_4]^{4-}$ observed at all samples suggest the $BaSi_2$ crystallization. Prolonging the t_a sharpens the vibration bands, indicating the promotion of crystallization. It is additionally reflected by the decrease of absorptance (Figure 4.17c). The surface oxidation also happens, implicate by the oxide band ~315 cm^{-1} (Figure 4.16a and b) [40]. Besides, Raman spectra of some specific regions at $BaSi_2$-650/10 surface present a Si band (Figure 4.16c and Figure 4.17).

A more significant surface morphological change is observed with T_a = 700 °C (Figure 4.16g – 4.16i). Cracks at the sample $BaSi_2$-700/1, probably caused by the thermal expansion coefficient mismatch, disappear by prolonging the T_a. It can be the result of the surface composition variation, reflected by the surface color change (Figure 4.16g and 4.16h). Yet we cannot assert the situation of cracks below the surface region, which remains to be investigated.

Prolonging the t_a induces a non-uniform surface, including the appearance and composition. Accompanying the formation of blue and brow regions at surface of $BaSi_2$-700/5, the Si Raman band can be noticed in the surface region (Figure 4.16e). Though, the Si band in bottom region is less distinguishable. Further extending the t_a to 10 min results in area expansions of blue and brown regions (Figure 4.16i). Moreover, some regions, i.e., C and D regions in Figure 4.16i, only exhibit strong Si bands in Raman spectra (Figure 4.16f).

Accordingly, the annealing process of $BaSi_2$, in the respect of temporal structure and composition evolution, can be roughly divided into three phases: (i) Si NCs free and uniform surface oxidation, (ii) Si NCs formation involving non-uniform surface oxidation, and (iii) Si NCs formation in bottom region, as illustrated by the Figure 4.16j.

4.3.3. Oxidation-induced structural transformation

Previous researches have credited the $BaSi_2$ oxidation and Si NCs formation to the reaction:

$$2BaSi_2 + O_2 \rightarrow 2BaO + 4Si \quad \Delta_r G = -841.87\ \text{kJ/mol} \tag{4.1}$$

by which Si atoms (or $[Si_4]^{4-}$) are isolated and form Si NCs [40, 41]. $\Delta_r G$ is the change in Gibbs free energy of the reaction at the temperature of 650 °C (923 K). $\Delta_r G$ is calculated by the standard formation enthalpy and entropy of the reactant and resultant [21]. The thermodynamic properties of $BaSi_2$ powder here are utilized [42, 43].

Equation 4.1 can hardly explain the structural transformation of $BaSi_2$ in neither the depth nor time scale as described before. By such a single-stage reaction, Si NCs are supposed to distribute uniformly in the surface region, and should be formed in the initial oxidation phase. Herein, an oxidation-induced structure transformation mechanism is proposed and illustrated in the Figure 4.18, which is based on the above structure and interface investigations. The single-stage reaction (Equation 4.1) is elaborated to a multi-stage variation including three major phases.

Initial oxidation phase at the air/$BaSi_2$ interface. In this first-stage phase, the film surface is rapidly oxidized by the residual O_2 (as well as the moisture) in the N_2 annealing

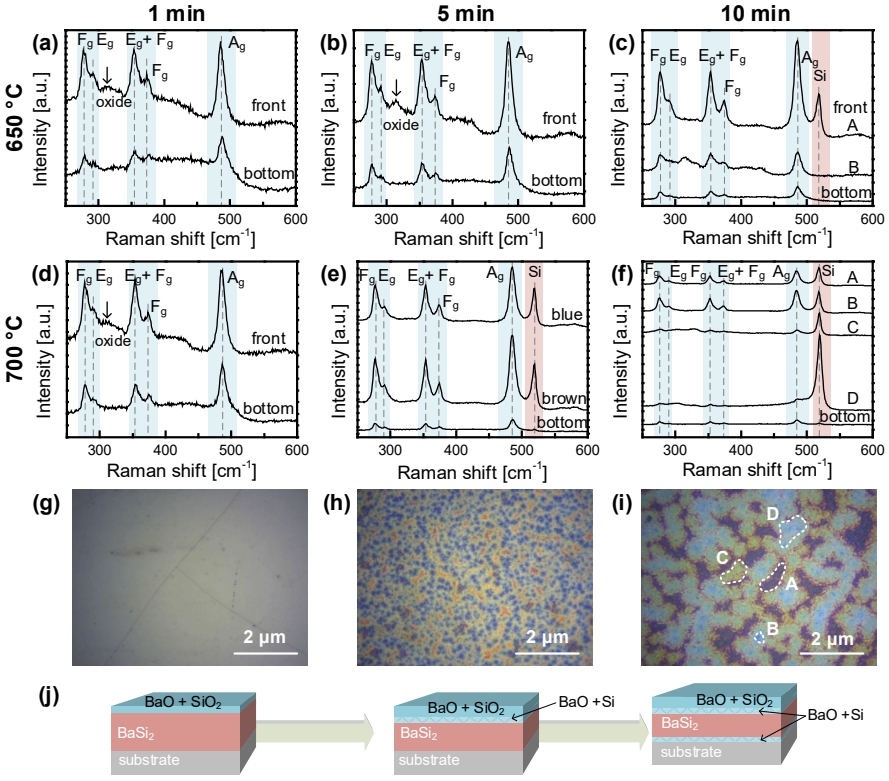

Figure 4.16: Raman spectra of (a) $BaSi_2$-650/1, (b) $BaSi_2$-650/5, (c) $BaSi_2$-650/10, (d) $BaSi_2$-700/1, (e) $BaSi_2$-700/5, and (f) $BaSi_2$-700/10. The vibrational band at ~315 cm^{-1}, indicated by arrows, refers to surface oxides. Optical microscope images of (g) $BaSi_2$-700/1, (h) $BaSi_2$-700/5, and (i) $BaSi_2$-700/10 were captured by the Raman setup. (j) Schematic representation of $BaSi_2$ structural evolution in the time scale.

ambient environment (process I in Figure 4.18),

$$2BaSi_2 + 3O_2 \rightarrow 2BaO + 4SiO_2 \quad \Delta_r G = -4189.53\ \text{kJ/mol} \tag{4.2}$$

Consequently, the film surface is covered with a thin oxide layer, mainly consisting of BaO and SiO_2. Additionally, the slight trace of C detected by AES (S12, Supporting Information) in the surface can be regarded as the outcome of the reaction (not indicated in Figure 4.18)

$$BaSi_2 + 5H_2O + CO_2 \rightarrow BaCO_3 + 2SiO_2 + 5H_2 \quad \Delta_r G = -505.09\ \text{kJ/mol} \tag{4.3}$$

The crystallization process of $BaSi_2$ does initiate at the same time. Hence, $BaSi_2$ vibrational bands together with an oxide band can be found in Raman spectra of $BaSi_2$-650/1, -650/5, and -700/1 (Figure 4.16a, 4.16b and 4.16d).

Oxide layer growth phase at the oxide/$BaSi_2$ interface. Besides the surface oxidation,

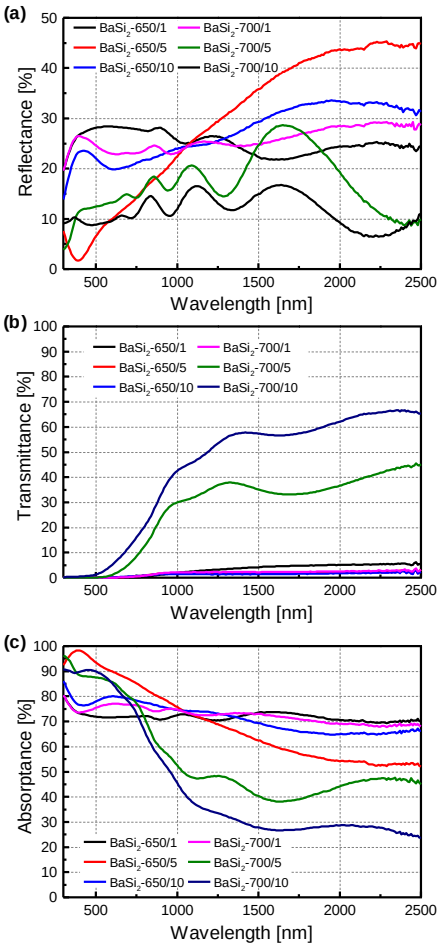

Figure 4.17: Wavelength-dependent (a) reflectance, (b) transmittance, and (c) absorptance curves of $BaSi_2$ thin films annealed at 650 and 700 °C for 1, 5, and 10 min, respectively.

the resultant SiO_2 also provides an additional path for oxide/$BaSi_2$ interfacial front advancing to the deeper region (process II in Figure 4.18), which is defined as

$$BaSi_2 + SiO_2 \rightarrow 2BaO + 5Si \quad \Delta_r G = -99.65\ \text{kJ/mol} \tag{4.4}$$

Actually, it is also an oxidation reaction of $BaSi_2$, due to the electron's loss of Si in $BaSi_2$. Indeed, the evolving oxide/$BaSi_2$ interfacial front can be roughly tracked with simultaneous recording of depth Raman spectroscopy. Extending the annealing duration increases the concentration of isolated Si atoms. Those Si atoms can either form Si NCs, verified by Si band in Raman spectra, or be oxidized to SiO_2 by the O_2 molecules that manage to penetrate through the thin oxide layer (process III in Figure 4.18), reflected by the Si(O) curve upward trend in Layer I of Figure 4.8.

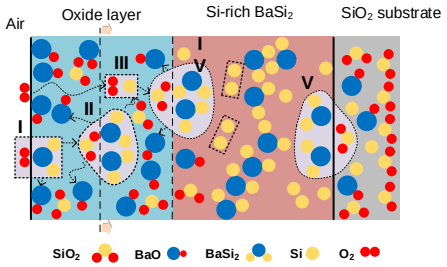

Figure 4.18: Schematic representation of oxidation-induced structure transformation of $BaSi_2$ films during the high-temperature annealing process (Note that the diagram does not represent the real microstructures of the materials)

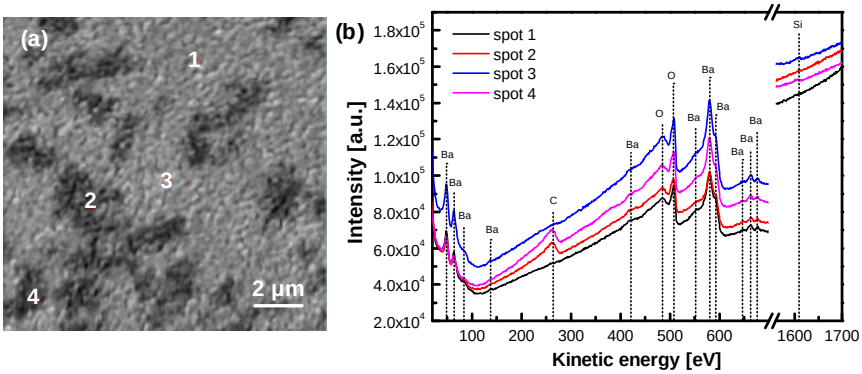

Figure 4.19: (a) Image of $BaSi_2$-650/60 surface, over which dark spots are randomly distributed. (b) Auger spectra of regions illustrate in (a). A C-rich composition (presumably $BaCO_3$) is detected with the dark spot.

More $BaSi_2$ is depleted by the process IV. Consequently, the oxide layer grows thicker, which inhibits the further penetration of O_2 as well as the subsequent formation of SiO_2. It is the reason of the SiO_2 concentration decrease within the Layer III (see Figure 4.8). In this way, Si atoms (in the form of SiO_2) in the oxide layer are gradually yet only partially replaced by Ba atoms (forming BaO) from the buried $BaSi_2$ layer. Figuratively speaking, the Ba atoms are dragged to the upper oxide layer by the oxidation reactions. Hence, a higher concentration of Ba in the surface region is detected by AES spectroscopy (Figure 4.8), while the Si atomic concentration can only reach nearly half of that of Ba. Note that the movement of Ba, in turn, leads to Si atom accumulation in the $BaSi_2$ layer, especially near the oxide/$BaSi_2$ interface. Moreover, such SiO_2-triggered oxide layer growth results in the boundary variation between Lay II and III (see Figure 4.8).

Oxygen-driven Ba diffusion at the $BaSi_2$/SiO_2 interface. With a longer t_a, Si vibration bands appear in the Raman spectra in the case of detection from the substrate side. In such condition, the Equation 5 is valid at $BaSi_2/SiO_2$ interface. Similarly, isolated Si atoms formed Si NCs, interpreting the Si atom accumulation near the $BaSi_2/SiO_2$ inter-

face (Figure 4.8) as well as the consequent Ba diffusion into SiO_2. In spite of the slight Ba diffusion within the thin oxide layer, no Ba atom can be detected throughout the n-type poly-Si interlayer in Figure 4.9. Hence, we can assert that it is the oxygen (in SiO_2) that drives the Ba diffusion.

The oxidation-induced structure transformation mechanism allows the interpretation of both composition and structure transitions of $BaSi_2$ thin films that occurred at higher T_a. i.e., 650, 700 and 750 °C. However, cases of lower T_a, such as 550 and 600 °C, are more challenging to explain. Equation 4.2 – 4.4 can theoretically occur at T_a = 550 and 600 °C. Nevertheless, no distinguishable layered structure or Si NCs can be observed in samples $BaSi_2$-550/90 and -650/90 (Figure 4.3). It may result from the low-degree crystallization of $BaSi_2$ (Figure 4.3) and the existence of impurities (Figure 4.6). One can speculate that the $BaSi_2$ crystal structure transition from amorphous to crystalline state also changes the thermodynamic properties of the material. Those property changes may consequently suppress the above-mentioned structure transformation process. Further researches remain to be conducted, which can lay an alternative path to enhance the thermodynamic stability of $BaSi_2$ for a wider processing temperature PV application.

4.4. Conclusions

In summary, our work established an oxidation-induced structure transformation mechanism, based on structural and interfacial investigations on sputtered $BaSi_2$ films. Polycrystalline $BaSi_2$ thin films are obtained via RF sputtering followed by a post-annealing process. An oxidation-induced structure transformation mechanism is proposed to interprets the transition from once homogenous and stoichiometric films to a layered and multi-phase structure. It is not limited to the sputtering case but can be extended to epitaxial and evaporated $BaSi_2$ thin films related to high-temperature processes. Besides, the established Raman spectroscopy depth profiling method provides a fast and facile path for structural analysis of $BaSi_2$ films. Even though the sputtering technique is proven to be a suitable method for $BaSi_2$ thin-film synthesis, more efforts still need to be put on quality improvement of sputtered $BaSi_2$, especially on the development of anti-oxidation/diffusion approaches. Those fundamental knowledge of structural transformations and complex interfacial activities are significant to further quality control and interface engineering on $BaSi_2$ films toward high-efficiency solar cells. With the respect to device developments, interfacial phenomena discussed in this research also provide important information for $BaSi_2$-based thin-film solar cell architecture design.

References

[1] Y. Tian, R. Vismara, S. Van Doorene, P. Šutta, Ľ. Vančo, M. Veselý, P. Vogrinčič, O. Isabella, and M. Zeman, *Oxidation-induced structure transformation: Thin-film synthesis and interface investigations of barium disilicide toward potential photovoltaic applications,* ACS Applied Energy Materials **1**, 3267 (2018).

[2] A. Goetzberger, C. Hebling, and H.-W. Schock, *Photovoltaic materials, history, status and outlook,* Materials Science and Engineering: R: Reports **40**, 1 (2003).

[3] C. Wadia, A. P. Alivisatos, and D. M. Kammen, *Materials availability expands the opportunity for large-scale photovoltaics deployment,* Environmental Science & Technology **43**, 2072 (2009).

[4] M. A. Green and S. P. Bremner, *Energy conversion approaches and materials for high-efficiency photovoltaics,* Nature Materials **16**, 23 (2016).

[5] S. Kurtz, N. Haegel, R. Sinton, and R. Margolis, *A new era for solar,* Nature Photonics **11**, 3 (2017).

[6] T. Suemasu, *Exploring the possibility of semiconducting $BaSi_2$ for thin-film solar cell applications,* Japanese Journal of Applied Physics **54**, 07JA01 (2015).

[7] T. Suemasu and N. Usami, *Exploring the potential of semiconducting $BaSi_2$ for thin-film solar cell applications,* Journal of Physics D: Applied Physics **50**, 023001 (2016).

[8] S. Yachi, R. Takabe, H. Takeuchi, K. Toko, and T. Suemasu, *Effect of amorphous Si capping layer on the hole transport properties of $BaSi_2$ and improved conversion efficiency approaching 10% in p-$BaSi_2$/n-Si solar cells,* Applied Physics Letters **109**, 072103 (2016).

[9] D. Tsukahara, S. Yachi, H. Takeuchi, R. Takabe, W. Du, M. Baba, Y. Li, K. Toko, N. Usami, and T. Suemasu, *p-$BaSi_2$/n-Si heterojunction solar cells with conversion efficiency reaching 9.0%,* Applied Physics Letters **108**, 152101 (2016).

[10] A. Pokhrel, L. Samad, F. Meng, and S. Jin, *Synthesis and characterization of barium silicide ($BaSi_2$) nanowire arrays for potential solar applications,* Nanoscale **7**, 17450 (2015).

[11] K. O. Hara, Y. Nakagawa, T. Suemasu, and N. Usami, *Realization of single-phase $BaSi_2$ films by vacuum evaporation with suitable optical properties and carrier lifetime for solar cell applications,* Japanese Journal of Applied Physics **54**, 07JE02 (2015).

[12] N. A. A. Latiff, T. Yoneyama, T. Shibutami, K. Matsumaru, K. Toko, and T. Suemasu, *Fabrication and characterization of polycrystalline $BaSi_2$ by RF sputtering,* Physica Status Solidi (c) **10**, 1759 (2013).

[13] T. Yoneyama, A. Okada, M. Suzuno, T. Shibutami, K. Matsumaru, N. Saito, N. Yoshizawa, K. Toko, and T. Suemasu, *Formation of polycrystalline $BaSi_2$ films by radio-frequency magnetron sputtering for thin-film solar cell applications,* Thin Solid Films **534**, 116 (2013).

[14] K. O. Hara, J. Yamanaka, K. Arimoto, K. Nakagawa, T. Suemasu, and N. Usami, *Structural and electrical characterizations of crack-free $BaSi_2$ thin films fabricated by thermal evaporation,* Thin Solid Films **595**, 68 (2015).

[15] Y. Nakagawa, K. O. Hara, T. Suemasu, and N. Usami, *Fabrication of single-phase polycrystalline $BaSi_2$ thin films on silicon substrates by vacuum evaporation for solar cell applications,* Japanese Journal of Applied Physics **54**, 08KC03 (2015).

[16] Y. Nakagawa, K. O. Hara, T. Suemasu, and N. Usami, *On the mechanism of $BaSi_2$ thin film formation on Si substrate by vacuum evaporation,* Procedia Engineering **141**, 23 (2016).

[17] K. O. Hara, C. T. Trinh, K. Arimoto, J. Yamanaka, K. Nakagawa, Y. Kurokawa, T. Suemasu, and N. Usami, *Effects of deposition rate on the structure and electron density of evaporated $BaSi_2$ films,* Journal of Applied Physics **120**, 045103 (2016).

[18] Z. Yang, Z. Hao, and Q. Xie, *Effects of annealing temperature on the structure and surface feature of $BaSi_2$ films grown on Si(111) substrates,* Physics Procedia **11**, 118 (2011).

[19] A. Sasaki, Y. Kataoka, K. Aoki, S. Saito, K. Kobayashi, T. Ito, K. Kakushima, and H. Iwai, *Power generation characteristics of Schottky-type solar cells fabricated using barium silicide,* Japanese Journal of Applied Physics **54**, 031202 (2015).

[20] T. Saito, D. Tsukada, Y. Matsumoto, R. Sasaki, M. Takeishi, T. Ootsuka, and T. Suemasu, *Wet chemical etching and X-ray photoelectron spectroscopy analysis of $BaSi_2$ epitaxial films grown by molecular beam epitaxy,* Japanese Journal of Applied Physics **48**, 106507 (2009).

[21] W. Haynes, *CRC handbook of chemistry and physics: A ready-reference book of chemical and physical data* (CRC Press, Boca Raton, Florida, 2014).

[22] R. Takabe, W. Du, K. Ito, H. Takeuchi, K. Toko, S. Ueda, A. Kimura, and T. Suemasu, *Measurement of valence-band offset at native oxide/$BaSi_2$ interfaces by hard X-ray photoelectron spectroscopy,* Journal of Applied Physics **119**, 025306 (2016).

[23] K. Morita, Y. Inomata, and T. Suemasu, *Optical and electrical properties of semiconducting $BaSi_2$ thin films on Si substrates grown by molecular beam epitaxy,* Thin Solid Films **508**, 363 (2006).

[24] K. O. Hara, N. Usami, M. Baba, K. Toko, and T. Suemasu, *N-type doping of $BaSi_2$ epitaxial films by arsenic ion implantation through a dose-dependent carrier generation mechanism,* Thin Solid Films **567**, 105 (2014).

[25] N. Shaalan, K. Hara, C. Trinh, Y. Nakagawa, and N. Usami, *Simple method for significant improvement of minority-carrier lifetime of evaporated $BaSi_2$ thin film by sputtered-AlO_x passivation,* Materials Science in Semiconductor Processing **76**, 37 (2018).

[26] K. O. Hara, C. T. Trinh, Y. Kurokawa, K. Arimoto, J. Yamanaka, K. Nakagawa, and N. Usami, *Fabrication of $BaSi_2$ thin films capped with amorphous Si using a single evaporation source,* Thin Solid Films **636**, 546 (2017).

[27] W. Du, R. Takabe, M. Baba, H. Takeuchi, K. O. Hara, K. Toko, N. Usami, and T. Suemasu, *Formation of $BaSi_2$ heterojunction solar cells using transparent MoO_x hole transport layers,* Applied Physics Letters **106**, 122104 (2015).

[28] K. Takahashi, Y. Nakagawa, K. O. Hara, Y. Kurokawa, and N. Usami, *Investigation of p-type emitter layer materials for heterojunction barium disilicide thin film solar cells,* Japanese Journal of Applied Physics **56**, 05DB04 (2017).

[29] R. Vismara, O. Isabella, and M. Zeman, *Back-contacted $BaSi_2$ solar cells: An optical study,* Optics Express (2017).

[30] M. Somer, *Vibrational spectra of the cluster anions $[E_4]^{4-}$ in Themetallic Sodium and Barium Compounds Na_4E_4 and Ba_2E_4 (E = Si, Ge),* Zeitschrift für anorganische und allgemeine Chemie **626**, 2478 (2000).

[31] Y. Terai, H. Yamaguchi, H. Tsukamoto, N. Murakoso, M. Iinuma, and T. Suemasu, *Polarized raman spectra of $BaSi_2$ epitaxial film grown by molecular beam epitaxy,* Japanese Journal of Applied Physics **56**, 05DD02 (2017).

[32] J. Zi, H. Büscher, C. Falter, W. Ludwig, K. Zhang, and X. Xie, *Raman shifts in Si nanocrystals,* Applied Physics Letters **69**, 200 (1996).

[33] L. Tsybeskov, K. D. Hirschman, S. P. Duttagupta, M. Zacharias, P. M. Fauchet, J. P. McCaffrey, and D. J. Lockwood, *Nanocrystalline-silicon superlattice produced by controlled recrystallization,* Applied Physics Letters **72**, 43 (1998).

[34] J. Evers, *Transformation of three-connected silicon in $BaSi_2$,* Journal of Solid State Chemistry **32**, 77 (1980).

[35] M. Imai, T. Hirano, T. Kikegawa, and O. Shimomura, *In situ measurements of the orthorhombic-to-trigonal transition in $BaSi_2$ sunder high-pressure and high-temperature conditions,* Physical Review B **55**, 132 (1997).

[36] J. Shi, W. Cui, J. A. Flores-Livas, A. San-Miguel, S. Botti, and M. A. L. Marques, *Investigation of new phases in the Ba–Si phase diagram under high pressure using ab initio structural search,* Physical Chemistry Chemical Physics **18**, 8108 (2016).

[37] G. Yang, Y. Zhang, P. Procel, A. Weeber, O. Isabella, and M. Zeman, *Poly-$Si(O)_x$ passivating contacts for high-efficiency c-Si IBC solar cells,* Energy Procedia **124**, 392 (2017).

[38] W. Du, R. Takabe, S. Yachi, K. Toko, and T. Suemasu, *Enhanced spectral response of semiconducting $BaSi_2$ films by oxygen incorporation,* Thin Solid Films **629**, 17 (2017).

[39] K. O. Hara, C. Yamamoto, J. Yamanaka, K. Arimoto, K. Nakagawa, and N. Usami, *Investigation on the origin of preferred a-axis orientation of $BaSi_2$ films deposited on Si(100) by thermal evaporation,* Materials Science in Semiconductor Processing **72**, 93 (2017).

[40] K. O. Hara, C. T. Trinh, Y. Kurokawa, K. Arimoto, J. Yamanaka, K. Nakagawa, and N. Usami, *Post-annealing effects on the surface structure and carrier lifetime of evaporated $BaSi_2$ films,* Japanese Journal of Applied Physics **56**, 04CS07 (2017).

[41] K. O. Hara, N. Usami, Y. Hoshi, Y. Shiraki, M. Suzuno, K. Toko, and T. Suemasu, *Structural study of BF_2 ion implantation and post annealing of $BaSi_2$ epitaxial films,* Japanese Journal of Applied Physics **50**, 121202 (2011).

[42] S. D. Gordienko, *Thermodynamic properties of silicides of alkaline-earth metals,* Powder Metallurgy and Metal Ceramics **36**, 502 (1997).

[43] G. Balducci, S. Brutti, A. Ciccioli, G. Trionfetti, A. Palenzona, and M. Pani, *Thermodynamic properties of barium silicides from vapor pressure measurements and density functional calculations,* Intermetallics **16**, 1006 (2008).

5

Vacuum-Annealed $BaSi_2$ Films

Abstract

As a potential absorber candidate for high-efficient solar cell applications, $BaSi_2$ films are confronted with issues of surface oxidation associated with the high-temperature annealing. Herein, $BaSi_2$ films are deposited by sputtering. A vacuum annealing process is subsequently carried out to crystallize sputtered $BaSi_2$ films. Raman spectroscopy is used to study surface structures and crystalline quality. The elemental depth profile is measured by Auger electron spectroscopy to understand the compositions of films. Optical and electrical properties are further investigated to reveal the effects of the annealing condition. Applying the vacuum annealing condition can effectively suppress diffusion of Ba and ensure a stochiometric $BaSi_2$ layer. However, surface oxidation still occurs even in the vacuum environment owing to the high reactivity of Ba.

Parts of this chapter have been published in Japanese Journal of Applied Physics, **59**, SFFA03 (2020) [1]

5.1. Introduction

The $BaSi_2$ films sputtered at room temperature are associated with high-temperature annealing for crystallization. And issues related to the high-temperature annealing, such as the surface oxidation and the associated Ba diffusion, hinder the development of sputtered $BaSi_2$ [2]. To alleviate those issues, some attempts can be tried, including $BaSi_2$ sample architecture redesign, oxide layer etching, and annealing condition controlling. Capping layer, such as a-Si, can be employed to change the sample architecture and to prevent surface oxidation [3–5]. However, reactions between the additional layer and $BaSi_2$ may introduce other issues and increase the difficulties of film quality control [4]. In respect to etching, the high reactivity of $BaSi_2$ definitely increases the complexity of both wet- and dry-etching method developments. Controlling the annealing condition is relatively a facile strategy. The $BaSi_2$ film, annealed at N_2 atmosphere with the existing of residual O_2, presents a thick oxide layer around 200 nm, and a Si-rich composition [2]. By reducing the oxygen content or introducing the reducing atmosphere, the surface oxidation and Ba diffusion may be effectively suppressed.

Herein, we present the effects of high-vacuum annealing conditions on the properties of $BaSi_2$ films. $BaSi_2$ thin films are deposited through sputtering processes and are subsequently annealed in a high-vacuum environment. Structural, optical, and electrical properties are characterized to investigate the influences of annealing conditions. Employing a high-vacuum annealing environment can effectively alleviate Ba diffusion and improve the stoichiometry of $BaSi_2$ layer. However, the surface oxidation cannot be effectively avoided, thus other anti-oxidation strategies need to be attempted. This research sheds light on the optimization of $BaSi_2$ annealing methods. Combining it with other anti-oxidation annealing strategies may help with developing high-quality $BaSi_2$ films and high-efficient solar cells [6–9].

5.2. Experimental

$BaSi_2$ films were deposited by RF magnetron sputtering. Subsequent annealing was conducted at temperatures ranging from 550 to 630 °C in a high vacuum ($< 10^{-4}$ Pa) environment. Raman spectra were recorded on a Renishaw InVia^{TM} confocal Raman microscope with 633-nm laser excitation. Elemental composition analysis was carried out in Jeol JAMP 9510-F Auger Microprobe at 10 keV energy with a tilt angle of 30°. During sputtering cycles, 1000 eV Ar^+ ions were utilized. Reflectance and transmittance were obtained on a Perkin Elmer Lambda 950 UV-Vis-NIR spectrometer single beam instrument over a range of 300 – 2500 nm. Resistivity and Hall effect measurements were conducted with van der Pauw geometry. Al contacts were deposited by vacuum evaporation (PRO500S, Provac). Samples were subsequently annealed at 130 °C for 30 min to ensure ohmic contacts.

5.3. Results and discussion

5.3.1. Surface structure

Figure 5.1 presents Raman spectra of $BaSi_2$ annealing *in vacuo* at different temperatures, namely 550, 575, 600, and 630 °C. Annealing durations are kept the same for 30 min.

Raman signatures of $BaSi_2$ can be observed in all spectra, suggesting the existence of the crystalline phase of $BaSi_2$ in all samples [10]. The crystallization of sputtered $BaSi_2$ can be achieved at lower annealing temperatures in vacuo than in N_2 atmosphere. Obvious $BaSi_2$ vibration bands can be observed even in the sample annealed at 550 °C, while no distinguishable peaks can be found with samples annealed at the same temperature in N_2. The vacuum condition can decrease the thermal budget for $BaSi_2$ crystallization [2]. And in this condition, the sample annealed at 600 °C has already exhibited a rather sharp Raman spectrum.

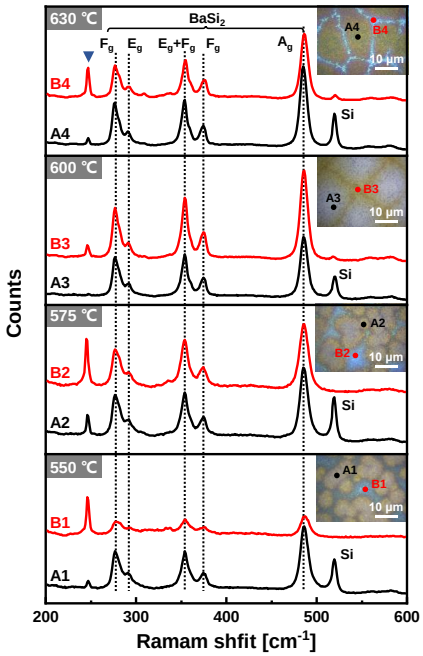

Figure 5.1: Raman spectra of $BaSi_2$ annealed *in vacuo* at temperatures of 550 °C, 575 °C, 600 °C, and 630 °C. Inserts are optical microscopy images captured by the Raman setup.

However, non-uniform surfaces are observed with all the samples, displayed by the optical microscopy images in Figure 5.1. At a lower annealing temperature, such as 550 °C, the brownish region (point A1) holds a Raman spectrum presenting strong $BaSi_2$ bands together with a peak at 519 cm^{-1} associated to Si nanocrystals (NCs). The existence of Si NCs is the consequence of surface oxidation [2]. Hence, the composition of region A1 can be a mixture of $BaSi_2$, Si NCs, and other oxidation by-products. It should be addressed that the surface oxidation still occurred during the annealing process of $BaSi_2$ even in the high vacuum condition. This can be due to the high reactivity between $BaSi_2$ with residual oxygen (extremely low content considering the pressure in the scale of 10^{-3} μbar) in the annealing chamber. Besides, a weak peak at around 245 cm^{-1} can also be noticed. The intensity of this peak is much higher in the Raman spectrum of point B1 of the other region. On the other hand, $BaSi_2$ peaks are less distinguishable in

the point B1. It suggests a low degree of crystallization of $BaSi_2$. Interestingly, no Si peak is detected in the B1 region, indicating it is less oxidized. Hence, the peak at 245 cm^{-1} may be attributed to other Ba-Si(-O) compounds, which are inclined to be formed rather than $BaSi_2$ at a lower temperature. In summary, $BaSi_2$ annealed at a lower temperature (550 °C) is partially oxidized, containing Si NCs and other Ba-Si(-O) compounds. And in such a condition, $BaSi_2$ is not fully crystallized, leaving some amorphous phase.

By increasing the temperature to 575 °C, two different regions on the surface can still be observed. Obvious $BaSi_2$ peaks can be noticed in both regions. This indicates an enhancement of $BaSi_2$ crystallization due to the increase of annealing temperature. In the case of 600 °C, the surface appearance changes a lot from cases of 550 and 575 °C. Larger grains (with a color of light blue) are formed, as shown by the microscopy images in Figure 5.1. In the grain region, the Raman spectrum of point A3 contains no peak at 245 cm^{-1}, while the spectrum of point B3 in the boundary region exhibits a pretty weak Si peak, together with a weaker peak at 245 cm^{-1} comparing to B1 and B2. The annealing temperature of 600 °C may either avoid the formation of other Ba-Si(-O) compounds or promote the transition of these compounds to other compositions, which cannot be detected by Raman. When further increasing the temperature to 630 °C, which is the limit of the annealing equipment, more distinguishable regions can be noticed in the microscopy images. And a stronger peak at 245 cm^{-1} is displayed by the spectrum of point B4 in the boundary region. Therefore, temperature around 600 °C can be enough to crystallize $BaSi_2$ at vacuum according to Raman spectroscopy.

The samples annealed for longer durations have also been investigated. Figure 5.2 exhibits Raman spectra of $BaSi_2$ films annealed at 600 °C for 30, 60, and 90 min. Prolonging the annealing duration from 30 min to 60 min leads to few differences in Raman spectra. However, an obvious surface morphology change can be noticed. Boundary regions (B3) disappears in the surface of the sample annealed for 60 min. Further extending the duration to 90 min results in a surface that is more uniform. And Raman spectra of all regions in the samples annealed for 90 min contain strong Si peaks as well as peaks at 245 cm^{-1}. Hence, such uniformity enhancement of the surface can be a consequence of deeper surface oxidation. Longer annealing duration allows residual oxygen to react at $BaSi_2$ film surface during annealing. In summary, prolonging annealing cannot significantly improve $BaSi_2$ quality, but rather promotes the surface oxidation.

5.3.2. Elemental analysis

Raman spectroscopy only reflects the surface structure information. Auger Electron Spectroscopy (AES) was employed to investigate the atomic concentration depth profiles. The atomic concentration depth profile of $BaSi_2$ annealed at 600 °C for 30 min is depicted in Figure 5.3. There is an oxide layer on the surface, which mainly consists of SiO_2 and BaO. A trace of carbon is also detected, which may originate from residual CO_2 in the annealing chamber. The surface oxidation of $BaSi_2$ at a high temperature can be hardly prevented even by employing a high-vacuum environment. The relatively high reactivity of barium enables interactions even with extremely low-concentration residual O_2 and CO_2 in the chamber. Nevertheless, the high-vacuum annealing reduces the oxide layer thickness from ~200 nm (annealed in N_2 atmosphere) to ~100 nm [2]. Meanwhile, the $BaSi_2$ layer holds a good stoichiometry, with a Ba:Si ratio of 1:2. Fewer Ba atoms dif-

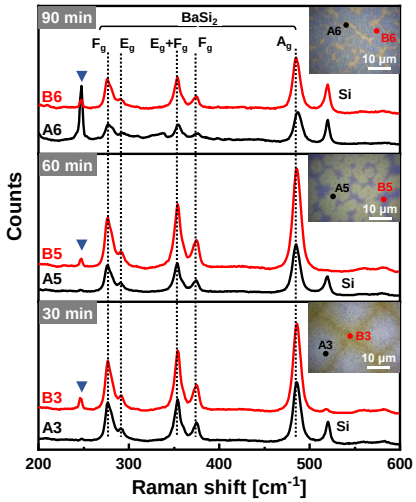

Figure 5.2: Raman spectra of $BaSi_2$ films annealed at 600 °C for 30, 60, and 90 min.

fuse to the surface or substrate. Oxygen is the cause of driving the diffusion of Ba. By reducing the content of oxygen, the diffusion of Ba is suppressed, preventing a drastic structural transformation of $BaSi_2$ films.

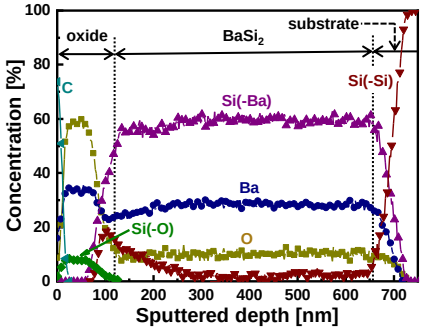

Figure 5.3: Elemental concentration depth profiles of $BaSi_2$ annealed at 600 °C for 30 min Si bonded with O, Ba, and Si are denoted as Si(–O), Si(–Ba), and Si(–Si), respectively.

5.3.3. Optical and electrical properties

The optical and electrical properties of $BaSi_2$ annealing *in vacuo* were further characterized. Figure 5.4 shows the absorptance curves of $BaSi_2$ annealed at 550 to 630 °C. A slight increase of ultraviolet-visible absorptance can be noticed with the increase of annealing temperature. However, all samples display strong infrared absorptance where the photon energy is lower than $BaSi_2$ band gap around 1.3 eV [11]. The infrared absorptance can be reduced by increasing the annealing temperature. When the annealing tempera-

ture reaches to 575 °C, the infrared absorptance does not significantly decrease. This is most likely related to the presence of band-gap states resulted from detective phases or impurities. Combining with Raman spectra, the lower temperature can hardly induce a full crystallization of $BaSi_2$. Defects in the film could cause the band gap states and result in this infrared absorptance. Higher annealing temperatures could reduce the defective phases and alleviate such absorptance below the band gap.

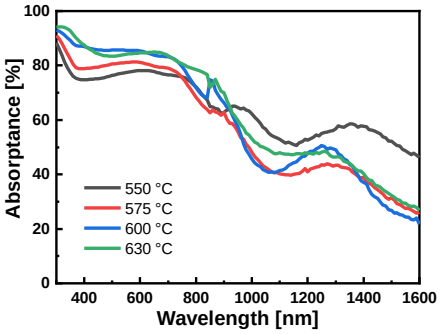

Figure 5.4: Absorptance curves of $BaSi_2$ annealed at temperatures ranging from 550 to 630 °C.

Hall effect measurements were conducted to determine carrier type and concentrations. As shown in Figure 5.5, $BaSi_2$ films annealed at lower temperatures, namely 550 and 575 °C, randomly present *n* or *p* carrier types. Owing to the presence of a high volume of impurities and amorphous phases, samples may not have a specific conduction type. By enhancing the annealing temperature, a constant sign of carrier type can be observed. The sample annealed at 600 °C exhibits an *n*-type nature, with an average electron carrier concentration of 3.01×10^{17} cm^{-3}. The sample annealed at 630 °C possesses an even lower average electron carrier concentration of 1.52×10^{17} cm^{-3}. A higher annealing temperature can improve the crystallinity and reduce the vacancy defects in the film. Consequently, the carrier concentration would decrease. Interestingly, for increasing annealing temperature, an overall decreasing trend of carrier concentration magnitude is observed, despite the unpredictable carrier type in cases of 550 and 575 °C.

5.4. Conclusions

In summary, this work investigated the effects of the vacuum annealing condition on the properties of sputtered $BaSi_2$ films. Employing the vacuum condition can alleviate the diffusion of Ba, thus ensuring a stoichiometric $BaSi_2$ layer. Despite the fact that surface oxidation still occurs during vacuum annealing, the thickness of the oxide layer is reduced as compared to the case of N_2 atmosphere annealing. Moreover, increasing annealing temperature can reduce the defective phases and enhance the crystalline quality of $BaSi_2$. The drop of infrared absorptance and decrease carrier concentration can be noticed as results of the defect decrease. The annealing temperature of 600 °C with a duration of 30 min is sufficient to promote the $BaSi_2$ crystallization in vacuo. Further research is still required to establish the method for achieving PV-grade sputtered $BaSi_2$

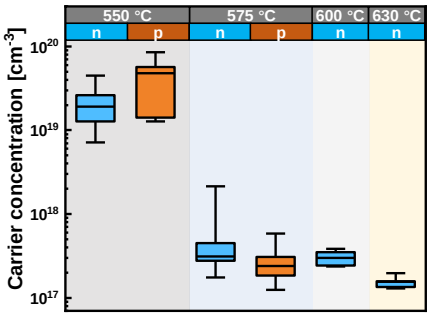

Figure 5.5: Carrier concentrations of $BaSi_2$ films annealed at temperatures ranging from 550 to 630 °C.

films, with limited surface oxidation and fewer defects or impurities.

References

[1] Y. Tian, A. R. Montes, Ľ. Vančo, O. Isabella, and M. Zeman, *Properties of sputtered $BaSi_2$ thin films annealed in vacuum condition,* Japanese Journal of Applied Physics **59**, SFFA03 (2020).

[2] Y. Tian, R. Vismara, S. Van Doorene, P. Šutta, Ľ. Vančo, M. Veselý, P. Vogrinčič, O. Isabella, and M. Zeman, *Oxidation-induced structure transformation: Thin-film synthesis and interface investigations of barium disilicide toward potential photovoltaic applications,* ACS Applied Energy Materials **1**, 3267 (2018).

[3] S. Yachi, R. Takabe, H. Takeuchi, K. Toko, and T. Suemasu, *Effect of amorphous Si capping layer on the hole transport properties of $BaSi_2$ and improved conversion efficiency approaching 10% in p-$BaSi_2$/n-Si solar cells,* Applied Physics Letters **109**, 072103 (2016).

[4] Y. Tian, A. Montes, O. Isabella, and M. Zeman, *Effects of amorphous Si capping layer on sputtered $BaSi_2$ film properties,* (2018).

[5] K. O. Hara, C. T. Trinh, Y. Kurokawa, K. Arimoto, J. Yamanaka, K. Nakagawa, and N. Usami, *Fabrication of $BaSi_2$ thin films capped with amorphous Si using a single evaporation source,* Thin Solid Films **636**, 546 (2017).

[6] T. Saito, D. Tsukada, Y. Matsumoto, R. Sasaki, M. Takeishi, T. Ootsuka, and T. Suemasu, *Wet chemical etching and X-ray photoelectron spectroscopy analysis of $BaSi_2$ epitaxial films grown by molecular beam epitaxy,* Japanese Journal of Applied Physics **48**, 106507 (2009).

[7] W. Du, R. Takabe, M. Baba, H. Takeuchi, K. O. Hara, K. Toko, N. Usami, and T. Suemasu, *Formation of $BaSi_2$ heterojunction solar cells using transparent MoO_x hole transport layers,* Applied Physics Letters **106**, 122104 (2015).

[8] K. Takahashi, Y. Nakagawa, K. O. Hara, Y. Kurokawa, and N. Usami, *Investigation of p-type emitter layer materials for heterojunction barium disilicide thin film solar cells,* Japanese Journal of Applied Physics **56**, 05DB04 (2017).

[9] R. Vismara, O. Isabella, and M. Zeman, *Back-contacted $BaSi_2$ solar cells: an optical study,* Optics Express **25**, A402 (2017).

[10] T. Sato, H. Hoshida, R. Takabe, K. Toko, Y. Terai, and T. Suemasu, *Detection of local vibrational modes induced by intrinsic defects in undoped $BaSi_2$ light absorber layers using raman spectroscopy,* Journal of Applied Physics **124**, 025301 (2018).

[11] K. Morita, Y. Inomata, and T. Suemasu, *Optical and electrical properties of semiconducting $BaSi_2$ thin films on Si substrates grown by molecular beam epitaxy,* Thin Solid Films **508**, 363 (2006).

6

Face-to-Face Annealing Method

Abstract

In this chapter, sputtered $BaSi_2$ thin films are annealed by a face-to-face annealing (FTFA) approach. The employment of the FTFA approach results in an improvement of surface homogeneity and crystal quality of sputtered $BaSi_2$. Various covers are applied in the FTFA, including $BaSi_2$/glass, glass, and Si, which causes the film electrical and optical properties alterations. These impacts of the FTFA method on sputtered $BaSi_2$ films stem from two aspects, i.e., heat re-distributions caused by the variation of heat-transfer networks, and interfacial interactions within the confined space between the cover and the film. The FTFA approach provides a facile strategy for minimizing the impacts of $BaSi_2$ surface oxidation during high-temperature processes. These results and findings can push forward the material development of $BaSi_2$ and its photovoltaic applications.

Parts of this chapter have been published in the Physical Review Materials, **4**, 12, 125403, (2020) [1]

6.1. Introduction

Theoretically, the conversion efficiency (η) of an n-p $BaSi_2$ homojunction solar cell can reach 22.5 – 25%, while a $BaSi_2$/Si and n-Si/$BaSi_2$/p-Si heterojunction solar cells possess potential η up to 22.7% and 30.4%, respectively [2–4]. However, the highest experimentally obtained was achieved by a p-$BaSi_2$/n-Si heterojunction solar cell with η = 10%, wherein it was n-Si wafer rather than n-$BaSi_2$ acting as the light absorber [5]. The n^+-$BaSi_2$/p-$BaSi_2$/p^+-$BaSi_2$ diode only exhibited an extremely low η of ~0.1%, which is caused by a high volume of defects within the $BaSi_2$ [6]. Defects within the $BaSi_2$ can originate either from thin-film depositions, for instance, synthesis techniques, conditions, source materials, etc., or from post-growth treatments, such as doping, subsequent depositions, etc. [7–12]. The post-deposition annealing was always employed to reduce the content of defects [7, 10, 12]. Besides, annealing treatment was used to enable the crystallization of amorphous $BaSi_2$, for instance, room-temperature deposited samples and ion-implantation doped $BaSi_2$ films [9, 10, 13].

However, the employment of high-temperature annealing, in turn, can induce other issues such as surface oxidation and induced atomic inter-diffusion [8, 9], which plays a rather significant role in the quality control of sputtered $BaSi_2$ films. The annealing process is essential for the crystallization of room-temperature sputtered film. As a consequence of surface oxidation, an inhomogeneous surface of annealed samples can always be observed, which consists of high-volume and non-uniformly-distributed impurities such as BaO, Si nanocrystals (NCs), amorphous Si (a-Si), $FeSi_2$, $BaCO_3$, etc. [9, 14, 15]. Vacuum annealing conditions have been applied to suppress surface oxidation [14], which only made a limited contribution to the alleviation of surface oxidation. Additionally, a-Si anti-oxidation layers were deposited on the $BaSi_2$ surface before the annealing, in which a thick a-Si layer around 50 nm was needed to effectively suppress surface oxidation [15]. The thick anti-oxidation layer would be retained at the film surface in the form of a multi-phase Si (a-Si and Si NCs) layer, introducing additional issues into the sputtered $BaSi_2$ film applications. To obtain a film surface with fewer impurities and defects caused by oxidation and diffusion during annealing is crucial for the development of sputtered $BaSi_2$.

A face-to-face annealing (FTFA) approach is frequently used for GaAs semiconductors to prevent the out-diffusion of arsenic, in which the GaAs wafer is placed between a bottom Si wafer and a top GaAs wafer during the annealing [16]. Besides, the FTFA approach has been applied to suppress surface oxidation of thin-film materials, such as ZnO, AlN, Ga_2O_3, etc. [17–19]. As compared to the conventional annealing method, in which the film surface is exposed to the annealing ambient, the FTFA approach improves the thin-film properties due to a confined surface condition of the films and complicated solid-phase reactions [16]. A similar method has also been employed in evaporated $BaSi_2$ films, in which the FTFA method was applied to suppress the film surface oxidation for the sake of understanding the post-annealing effects on film property improvement [20, 21]. Nevertheless, the effects of the FTFA method on the properties of $BaSi_2$ and its underlying mechanism have not yet been systematically studied.

Herein, amorphous $BaSi_2$ thin films were deposited on glass substrates by radio frequency magnetron sputtering and were crystallized by applying the FTFA approach. The employment of the FTFA approach drastically enhances the sputtered $BaSi_2$ film surface

homogeneity in terms of structure and composition. Applying various FTFA cover materials demonstrates the potential of controlling the electrical and optical properties of $BaSi_2$. The mechanism of the FTFA approach is discussed from thermodynamic views on heat transfer and chemical physic perspectives of interfacial interactions. These results and finds shed a light on the application and optimization of the FTFA for $BaSi_2$ film fabrications and offer contributions to the development of the $BaSi_2$ material improvement methods.

6.2. Experimental

$BaSi_2$ films were deposited by RF magnetron sputtering equipment using a stoichiometric ceramic $BaSi_2$ target. Corning Eagle XG^{TM} glass was used as substrates. Ar was used for sputtering.Depositions were carried out at room temperature. The thickness of $BaSi_2$ was kept at around 500 nm. The subsequent annealing processes were carried out in a high vacuum (HV) environment ($< 10^{-4}$ Pa) with a temperature of 600 °C. The annealing duration is 30 min. Surface topology was analyzed by a 3-dimension (3D) Laser scanning microscope (Keyence VK-X250). Raman spectra were recorded on a Renishaw InVia^{TM} Raman microscope with 633-nm laser excitation. Acquisition times of Raman mapping and single spectral collection were set as 20 s and 100 s, respectively, due to the consideration of time consumption. Raman spectra were fitted with Renishaw WiRE^{TM} by using broadened Gaussian/Lorentzian line shapes. Majority carrier type and concentration were determined through resistivity and Hall effect measurements with van der Pauw geometry. Al contacts were deposited by vacuum evaporation (PRO500S, Provac), and were subsequently annealed at 130 °C for 30 min to ensure ohmic contact. Wavelength-dependent reflectance and transmittance were obtained on a Perkin Elmer Lambda 1050 UV-Vis-NIR spectrometer.

6.3. Results and discussion

6.3.1. FTFA approach and effects on surface homogeneity

The FTFA approach is illustrated in Figure 6.1a, in which two $BaSi_2$ films on the glass substrate ($BaSi_2$/glass) are placed together, the film surface to the film surface. The upper one functions as the cover for the FTFA approach, while the lower one is the obtained sample. The FTFA sample shows a metallic-grey appearance different from the blackish-blue surface of the conventionally annealed sample (exposed to the vacuum annealing ambient), as displayed by Figure 6.1b and 6.1c. The tiny blackish-blue area indicated in Figure 6.1b is the result of the partially-overlapped FTFA as illustrated in Figure 6.1d.

The optical microscopy image of the boundary region between the covered (blackish-blue) and the exposed (metallic-grey) areas is shown in Figure 6.1e. A clear transition from a heterogeneous surface in the exposed area to a quite homogeneous surface in the covered area. As shown in Figure 6.1e, the exposed area shows a non-uniform surface, where two distinct regions are observed. This surface heterogeneity in the exposed area can be ascribed to the surface oxidation of $BaSi_2$ due to the residual oxidants in the annealing ambient [9]. An enhancement in surface homogeneity is clearly shown in the covered area. The variation of surface appearance is normally related to its composition or geometry.

Figure 6.1f shows the reconstructed 3D image of the boundary region. In fact, the exposed area and the covered area demonstrate quite a smooth surface with a similar height. This suggests that the differences in surface appearance and homogeneity are likely stimulated by the composition variation rather than the geometrical change. Meanwhile, we can notice a rougher surface of the transition area between the exposed and covered areas. The transition region contains randomly distributed hills with heights of tens to hundreds of nanometers. This likely results from the lateral elemental diffusion between exposed and covered areas. The surface oxidation occurring at the exposed area can lead to an atomic movement from the covered area to the oxidation sites. Such atomic movements can lead to mass accumulations in the transition region and formations of those hills.

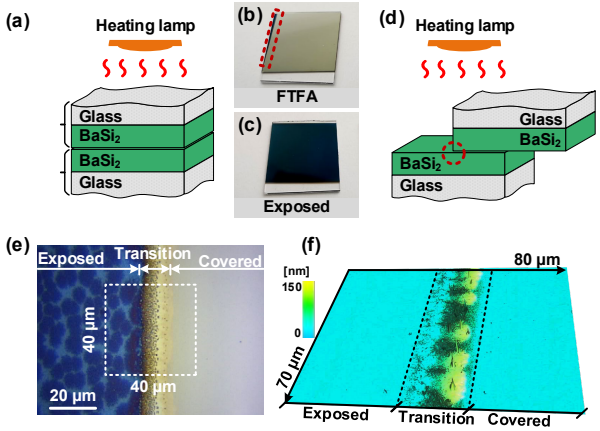

Figure 6.1: Schematic illustrations of (a) fully- and (d) partially-overlapped FTFA configurations for $BaSi_2$ annealing. Photographs of $BaSi_2$ samples (b) annealed by FTFA methods, and (c) exposed to annealing ambient. (e) Optical and (f) 3D-laser micrographs of the red-dashed boundary region between the exposed and covered areas in (b).

To understand the link between the variation of surface-appearance homogeneity with the film composition, Raman mapping measurements are carried out at the area indicated by the dash-line box Figure 6.1e. Besides the strongest A_g peak of $BaSi_2$ located at ~486 cm^{-1}, maps of the often-observed impurities $FeSi_2$ and Si nanocrystals (NCs) of sputtered $BaSi_2$ films with the Raman peaks at ~247 cm^{-1} and ~519 cm^{-1} [22–25], respectively, are profiled in Figure 6.2 . Figure 6.2a – 6.2c show the Raman peak-intensity maps of $FeSi_2$, Si NCs, and the A_g peak of $BaSi_2$, respectively. The peak-intensity maps can indicate the phase-content distribution within the detected depth of the film surface that is around 100 – 200 nm for $BaSi_2$ films [9]. Indeed, their Raman maps demonstrate three areas with different phase-distribution patterns, i.e., i) $X < -5$ μm, ii) -5 μm $< X <$ 10 μm and iii) $X > 10$ μm. These areas are precisely corresponded to i) the exposed area, ii) the transition area, and iii) the covered area in Figure 6.1e, respectively.

In the exposed area ($X < -5$ μm), Raman peak-intensity images demonstrate the phase distributions in a good agreement of the optical micrograph color pattern in Figure 6.1e. Although all compositions show inhomogeneous distributions, we can notice

that the distribution of Si NCs is the reverse of those of $FeSi_2$ and $BaSi_2$ in the exposed area. This is understandable considering that Si NCs are formed as the outcome of $BaSi_2$ oxidation and induced atomic diffusion within the films [7, 9, 26, 27]. The formation of $FeSi_2$ can be ascribed to the impurities from the sputtering target, and it thus shows a similar distribution to that of $BaSi_2$.

A dramatic change in compositions can be noticed in the transition area. Limited sites at the transition area show the Raman trace of $FeSi_2$. And we can observe the sudden drop of $FeSi_2$ peak intensity at the boundary between the covered and transition area ($X \approx -5$ µm). Differently, Si NCs show an increase of peak intensity when approaching the transition area, which reaches to the maximum near the boundary between the exposed and transition areas (-8 µm $< X < -2$ µm). And it then decreases gradually when X > -2 µm. Meanwhile, some sites near the boundary of transition and covered areas show an abnormally high Si NCs Raman signal, for instance, points (8,0) and (8,10) indicated in Figure 6.2b, which may correspond to hills observed in 6.1f. The peak-intensity profile of $BaSi_2$ (A_g) shows a similar trend to that of Si NCs at the exposed/transition boundary region, while it shows an intensity dip in the middle of the transition area. It is noteworthy that $BaSi_2$ (A_g) peak intensities at shows similar values at two boundary regions, i.e., the exposed/transition and the transition/covered boundaries.

When it goes to the covered area, the signal of $FeSi_2$ and Si NCs can no longer be collected. Only the $BaSi_2$ (A_g) is detected, which shows a relatively homogeneous peak-intensity distribution. We may speculate that the FTFA approach can alleviate the formation/crystallization of $FeSi_2$ and Si-NCs within the $BaSi_2$ film. However, the $BaSi_2$ (A_g) peak intensity at the covered area is quite lower than that at the exposed area. Although this can imply a lower of $BaSi_2$ content at the covered area within the detected depth, we cannot yet assert that the FTFA method reduces the concentration of $BaSi_2$ at the dimension of the entire thickness, considering that the surface compositional and structural difference between these two areas may alter the Raman-laser penetration depth, leading to the peak-intensity variations.

The full width at half maximum (FWHM) of the A_g peak is further extracted as an indicator for $BaSi_2$ crystal quality, and its mapping result is profiled in Figure 6.2d. An improvement of $BaSi_2$ crystal quality at the covered area is suggested by the decrease of FWHM values, though this area shows a lower $BaSi_2$ (A_g) peak intensity. The suppression of the impurity formations may keep the stoichiometry between Ba and Si within the sputtered films, and then results in better $BaSi_2$ crystal quality.

Based on these Raman mapping results together with microscopic results shown in Figure 6.1, we can deduce that the FTFA approach effectively improves the surface compositional homogeneity of $BaSi_2$ by suppressing the formations of $FeSi_2$ and Si NCs, which also leads to a better $BaSi_2$ crystal quality, as compared to the conventional annealing method.

6.3.2. Influence of FTFA cover materials

Besides the $BaSi_2$/glass cover, other covers including glass and silicon wafer are also employed for FTFA. These FTFA-annealed samples with covers of $BaSi_2$/glass, glass, and silicon wafer, herein denoted as $BaSi_2$-B, $BaSi_2$-G, and $BaSi_2$-S, respectively, as expected, demonstrate homogeneous surfaces, while the sample exposed to annealing ambient

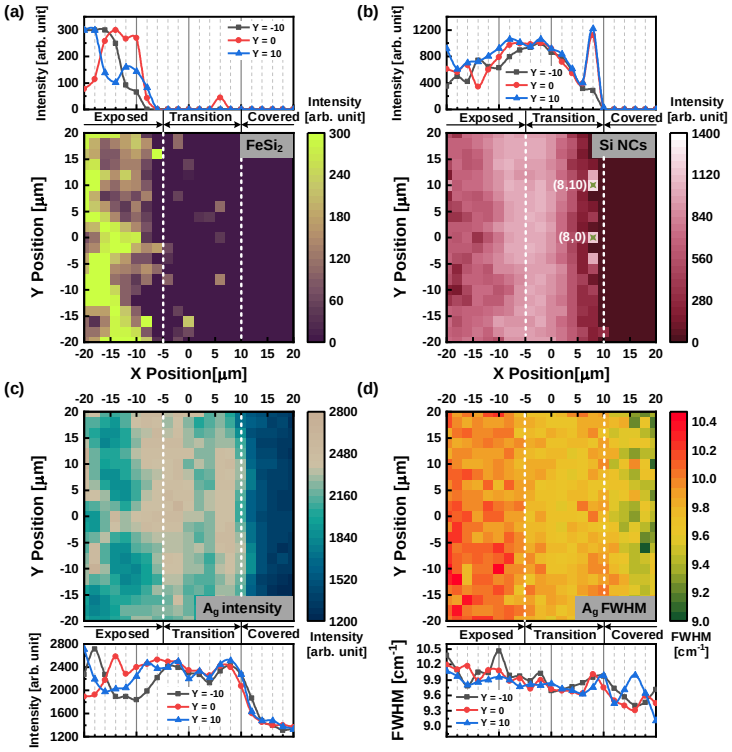

Figure 6.2: Raman peak intensity maps and horizontal profiles (Y = −10, 0, and 10 μm) of (a) $FeSi_2$ (~247 cm^{-1}), (b) Si NCs (~519 cm^{-1}), and (c) $BaSi_2$ A_g (~486 cm^{-1}). (d) FWHM distribution of $BaSi_2$ A_g peak and its horizontal profiles.

(named $BaSi_2$-E) exhibits a non-uniform surface including two distinct regions, i.e., dark grain and light bright filling regions, as shown in Figure 6.3. Their Raman spectra are presented in Figure 6.4. In agreement with Raman mapping results, the dark grain area of $BaSi_2$-E exhibits an obvious $FeSi_2$ peak with a weak Si-NCs peak, while the bright filling area demonstrates a stronger Si NCs without the $FeSi_2$ peak. On the contrary, FTFA samples only present Raman peaks originating from the $BaSi_2$, regardless of types of the cover.

Despite the same Raman spectral shapes of FTFA samples, it is worthwhile to address the slight peak-position shift among these samples. The Raman peak-position shift is normally related to defects within the $BaSi_2$ crystal. Herein, the A_g peak position of $BaSi_2$ is taken for discussions. As compared to the calculated results (A_g peak at 493 cm^{-1}), all samples display a blue shift (towards lower wavenumber), which is caused by the existence of defects, including Ba substituted for Si antisites (Ba_{Si}), Si vacancies (V_{Si}), and Si interstitials (Si_i) [16, 28]. The larger wavenumber of the A_g peak suggests a lower volume of these defects. All FTFA-annealed samples hold larger A_g position wavenumbers than that of $BaSi_2$-E, which implicates a diminution of the defect content owing to the FTFA

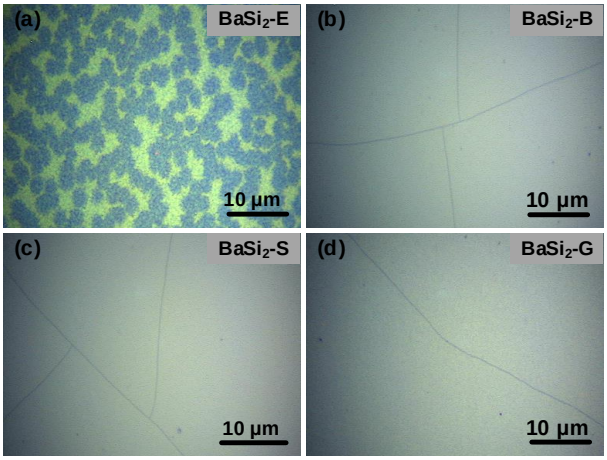

Figure 6.3: Optical microscopy images of (a) $BaSi_2$-E, (b) $BaSi_2$-B, (c) $BaSi_2$-S, and (d) $BaSi_2$-G.

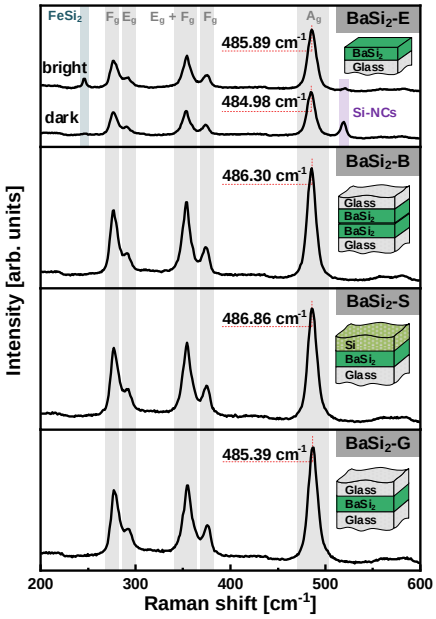

Figure 6.4: Raman spectra of $BaSi_2$-E, $BaSi_2$-B, $BaSi_2$-S, and $BaSi_2$-G.

method. Among them, $BaSi_2$-S exhibits the highest A_g position wavenumber of 486.86 cm^{-1}, indicating its lower content of those above-mentioned defects. $BaSi_2$-B and $BaSi_2$-G possess slightly lower values of 486.30 cm^{-1} and 485.39 cm^{-1}, respectively. Detailed Raman-peak information of sputtered $BaSi_2$ films, together with samples fabricated via

Table 6.1: Raman peak position information of $BaSi_2$.

Samples	$FeSi_2$	$BaSi_2$					Si NCs	Reference
	F_g	E_g	E_g+F_g	F_g	A_g		
	[cm^{-1}]	[cm^{-1}]	[cm^{-1}]	[cm^{-1}]	[cm^{-1}]	[cm^{-1}]	[cm^{-1}]	
$BaSi_2$-E (Dark)	-	276.76	288.99	353.32	373.68	484.98	518.86	This work
$BaSi_2$-E (Light)	246.13	277.17	290.07	354.1	374.6	485.89	521.08	This work
$BaSi_2$-B	-	277.34	289.47	354.28	374.58	486.3	-	This work
$BaSi_2$-S	-	277.79	290.01	354.92	375.25	486.86	-	This work
$BaSi_2$-G	-	276.99	289.37	353.59	373.74	485.39	-	This work
Sputtering [a]	-	279* [b]	291*	351*	373*	483*	518.5*	Ref. [26]
MBE [c]	-	277*	292*	355.5*	378*	487*	-	Ref. [29]
TE [d]	-	272*	287*	351*	373*	482*	-	Ref. [8]
$BaSi_2$ Powder	-	276	293	355	376	486	-	Ref. [22]
Calculation [e]		282*	294.5*	365*	380*	493	-	Ref. [28]

[a] $BaSi_2$ target with addition Ba source for sputtering, substrate temperature T_{sub} = 600 °C; [b] Data extracted from reported Raman spectra curves are marked with a '*'; [c] T_{sub} = 650 °C, deposition ratio between Ba and Si R_{Ba}/R_{Si} = 2.2; [d] $BaSi_2$ granules the evaporation source, T_{sub} = 700 °C; [e] Phonon density of states (DOS) calculations.

other techniques, is summarized in Table 6.1.

Figure 6.5a shows the carrier concentrations of sputtered $BaSi_2$ film with different cover materials during the FTFA. A transition of conductivity type from *n*-type to *p*-type is observed. $BaSi_2$-E exhibits an *n*-type conductivity, while $BaSi_2$-G presents a *p*-type conductivity. During the repeated measurements of majority carrier type, $BaSi_2$-B and $BaSi_2$-S randomly demonstrate *n*- or *p*-type conductivity with similar frequencies. We speculate a comparable electron and hole concentrations of these samples. Besides the variation of conductivity type, an increase of the magnitude of carrier concentration, as well as a decrease of the film resistivity (see Figure 6.5b), can be observed when applying the FTFA method. The FTFA samples exhibit carrier density on the scale of 10^{19} cm^{-3}, which is much higher than that of $BaSi_2$-E ($\sim 4.5 \times 10^{17}$ cm^{-3}).

Given that $BaSi_2$ films here are undoped, their *n*- and *p*-type conductivities can be attributed to the existence of V_{Si} that function as donors, and Ba vacancies (V_{Ba}) that behave as acceptors, respectively [6, 21, 30]. Indicated by the blue shift of Raman peaks, we can expect the reduction of V_{Si} in the film after applying FTFA. And the conductivity transition can be regarded as a result of the reduction of V_{Si} or donors. Meanwhile, the employment of FTFA may trigger the generation of other types of defects, such as V_{Ba} defects. Together with the reduction of V_{Si}, they can lead to a *p*-type conductivity of $BaSi_2$-G. The increase of the magnitude of carrier density can be related to a high-volume of metallic/defective phase within the film, which is indicated by their optical properties.

The wavelength-dependent reflectance, transmittance, and absorptance curves are shown in Figure 6.6. Although the FTFA approach can enhance $BaSi_2$ crystal quality, it does not significantly improve the $BaSi_2$ optical absorption properties. Conversely, we can notice that FTFA samples show a decrease of absorptance at UV and visible wavelength window, and pretty high absorptance tails at the near-infrared (NIR) wavelength range. Such optical properties degrading is normally related to defective and/or metallic impurities/phases within the films, which may generate free carriers and cause the

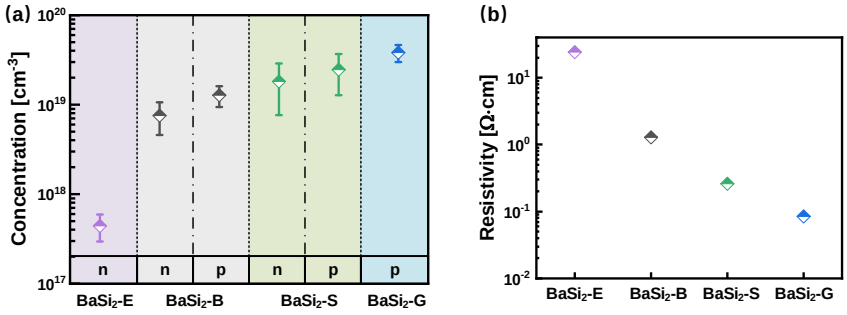

Figure 6.5: (a) Carrier concentrations and (b) resistivities of $BaSi_2$ films annealed with different cover materials.

increase of carrier density as mentioned above.

6.3.3. Mechanisms of the FTFA approach

The employment of the FTFA approach in the crystallization of sputtered $BaSi_2$ leads to significantly surface homogeneity improvement as compared to the conventional annealing approach. The electrical and optical properties can be altered by applying various cover materials in the FTFA. These effects of the FTFA method can be explained from considerations of heat transfer and surface reactions.

Heat transfer in the FTFA system

Halogen heating lamps were applied for heating the sample through radiation, whose main emitting wavelength ranges from 1 to 1.6 µm (NIR). The introduction of additional cover material between the heat source and the sample would alter the heat transfer system and change the way the sample is heated. Figure 6.7a illustrated the heat transfer process during the FTFA. Heat flux can reach the sample by two routes, i.e., through the cover or the holder, as shown in Figure 6.7a, which can be described below.

Heat transfer through the cover:

Process 1: Radiative heat transfer from the heater to the cover surface.

Process 2: Absorption and transmission in the cover. The process of radiation traversing the medium (herein the cover) can be described by the radiative transfer equation (RTE) [31]. It is complicated to solve such a five-dimensional integro-differential equation. For simplicity, we only make a qualitative description of the process and ignored the scattering and emission processes. The absorption of the radiant flux can heat the cover and leads to the heat transfer via the conduction through the cover. Meanwhile, part of the radiant flux travels through the cover and reaches the sample surface.

Process 3: The behaviors of radiant flux in the $BaSi_2$ film is similar to that in the cover. Thanks to the high absorption of the amorphous $BaSi_2$ at IR and NIR window [9], radiant flux can be effectively absorbed within the $BaSi_2$ layer, enabling its crystallization.

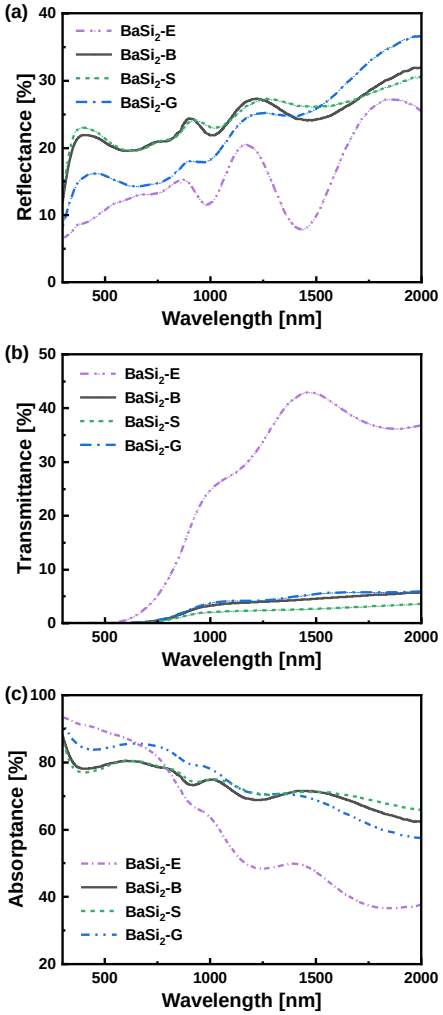

Figure 6.6: (a)Reflectance, (b)transmittance, and (c)absorptance curves of $BaSi_2$ films annealed with different configurations.

Heat transfer through the holder:

Process 4: Radiative heat transfer from the heater to the titanium sample holder, effectively heating the holder.

Process 5: Conduction heat transfer within the holder.

Process 6: Conduction heat transfer through the glass substrate towards the film bottom.

The thermal resistance (R_{th}) network model of the whole process is illustrated in Figure 6.7b. The thermal resistance is defined by [32],

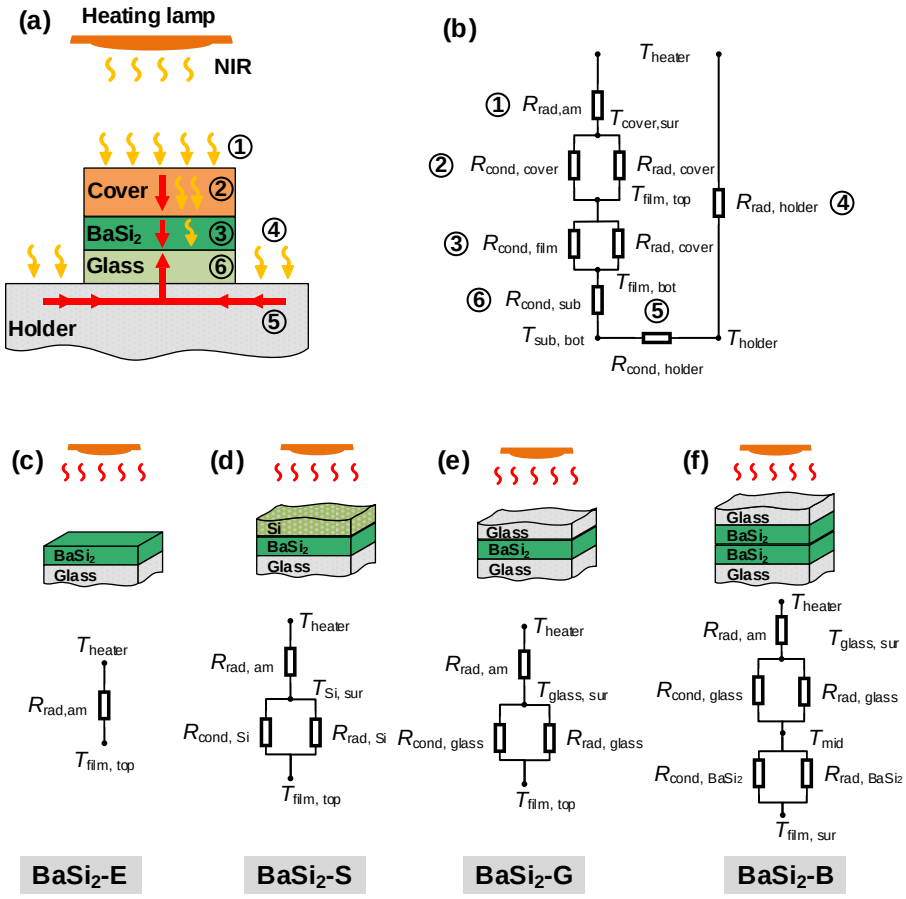

Figure 6.7: (a) Schematic illustration of the heat transfer process in the FTFA sample and (b) the heat transfer thermal resistance network model (rad = radiation, am = ambient, sur = surface, cond = conduction, sub = substrate). Thermal resistance network of heat transfer from the heater to film surface in (c) $BaSi_2$-E, (d) $BaSi_2$-S, and (e) $BaSi_2$-G, and (f) $BaSi_2$-B

$$R_{\text{th}} = \frac{\Delta T}{q} \tag{6.1}$$

where ΔT is the temperature difference, q is the heat flux passing through the resistance. The metal holder, being a good NIR radiant flux absorber, is rapidly heated up and the resulting heat is transferred to the film through the glass substrate. We may assume that amount of heat transferred through the holder is similar among all samples, due to the same substrate and holder in all cases. We focus on the analysis of heat transfer from the heater to the film surface. i.e., **Process 1** and **2**.

Figure 6.7c – 6.7f show the thermal resistance network models of the heat transfer from the heater (T_{heater}) to the film top surface ($T_{\text{film,top}}$) in the exposed and FTFA sam-

ples. Radiative and conductive heat transfer mechanisms are involved, which can be described by radiative (R_{rad}) and conductive (R_{cond}) thermals resistance [32]. Given the high vacuum ambient, the radiant flux can arrive at the sample surface with limited energy loss, which indicates a low thermal resistance of the ambient ($R_{rad,am}$). We can assume all samples share a similar and low $R_{rad,am}$.

In $BaSi_2$-E, the exposed amorphous $BaSi_2$ film directly absorbs the radiant flux. Note that the amorphous $BaSi_2$ presents a high absorption at the NIR window [9]. The absorption of radiant flux increases the temperature of the film. Together with the heat from the holder, it enables the crystallization of the film. The crystallization of $BaSi_2$ decreases its NIR absorption, letting the radiant flux to propagate deeper into the layer and thus promoting its crystallization.

Placing the covers of silicon and glass does not substantially change the $BaSi_2$ film heating mechanism. Considering that the both silicon and glass covers are transparent to the heater emitted NIR radiant flux (1 to 1.6 μm), most of the radiant flux can pass through the cover, then be absorbed by the $BaSi_2$ film, which is similar to that in $BaSi_2$-E. This implies the low radiative thermal resistance of Si ($R_{rad,Si}$) and glass 0($R_{rad,glass}$). As shown in Fig 4(d) and 4(e), the covers also hold the conductive thermal resistance $R_{cond,Si}$, and $R_{cond,glass}$, which can be determined by [32],

$$R_{cond} = \frac{d}{k_c A} \tag{6.2}$$

where d is the thickness of the layer, k_c is the thermal conductivity (a material property), A is the area normal to the heat flow. The thermal conductivity of Si ($k_{c,Si} = 0.4\ Wcm^{-1}K^{-1}$, when $T > 800$ K) is much larger than that of glass ($k_{c,glass} = 0.0142\ Wcm^{-1}K^{-1}$, when $T = 773$ K) [33, 34]. Their conduction resistances are $R_{cond,Si} = 0.01\ KW^{-1}$, and $R_{cond,glass} = 0.657\ KW^{-1}$, respectively. The significantly lower conduction resistance of the Si cover enhances its conductive heat transfer as compared to the case of the glass cover. Note that most radiant flux is absorbed by the $BaSi_2$ film, the temperature of the film surface ($T_{film,top}$) is assumed to be higher than the cover temperature. Heat can be transferred from the film to the cover through thermal conduction. The lower thermal resistance of Si cover would promote this conductive heat transfer, and decrease the temperature of the film. On the contrary, the high thermal resistance of glass can preserve the heat in the $BaSi_2$ film. This leads to a higher film temperature of $BaSi_2$-G than that of $BaSi_2$-S.

The situation of $BaSi_2$-B is more complicated, due to the absorption of the amorphous $BaSi_2$ layer in the cover. To describe this radiative heat transfer through the $BaSi_2$ layer, the Rosseland approximation of RTE can be used [35, 36], given that amorphous $BaSi_2$ is optically thick in the NIR range [9]. The equivalent radiative thermal conductivity (k_r) is introduced, which is defined as [37],

$$k_r = \frac{16n^2\sigma}{3\alpha_R} T^3 \tag{6.3}$$

where n is the refractive index of the medium, σ is the Stefan-Boltzmann constant, T is the temperature in K, and α_R is the Rosseland mean absorption coefficient, which is essentially a weighted average of the measured absorption coefficient with weighting function of temperature derivative of the Planck emission function [37]. The decrease

of the absorption results in the increase of k_r, suggesting the lower radiative thermal resistance (e.g., Si and glass). It needs to be mentioned that the quantitative analysis through Equation 6.3 is not applicable for Si and glass, as they are transparent at the heater peak-radiation window.

The effective thermal (k_{eff}) conductivity is given by,

$$k_{eff} = k_c + k_r \tag{6.4}$$

and the total thermal resistance can be expressed as,

$$R_{th,BaSi_2} = \frac{d}{k_{eff} A} \tag{6.5}$$

which is illustrated by the parallel thermal resistances $R_{cond,BaSi_2}$, and $R_{rad,BaSi_2}$ in Figure 6.7f. As the thermal parameters of amorphous $BaSi_2$ is unavailable, we can only give a qualitative analysis.

$BaSi_2$ layer in the cover absorbs the radiant flux resulting in its temperature increase (T_{mid}). The higher temperature of the $BaSi_2$ layer allows the conductive heat transfer to the deep bottom layer and the $BaSi_2$ film. The crystallization of $BaSi_2$ cover decreases its metallic phase concentration, in turn, decreases its absorption in the NIR window. This leads to the increase of radiative thermal conductivity (k_{rmr}) according to Equation 6.3. More heat propagates through the cover by radiation and arrives at the film surface. The $BaSi_2$ film then is heated as the same as the cases of other samples. Here, both conduction and radiation contribute to the crystallization of the film, which is different from other cases. And the cover is speculated to hold a higher temperature as compared to the film at the early phase of annealing. After the full crystallization of the $BaSi_2$ cover and the efficient heat conduction through the glass substrate, the film temperature can be similar or even higher as compared to the $BaSi_2$ cover. The glass in the cover functions the same as the glass cover in $BaSi_2$-G, decreasing the heat conduction through the cover.

Based on the analysis of the thermal resistance network, we can conclude that the $BaSi_2$ film temperature during the annealing is in the order of $BaSi_2$-E > $BaSi_2$ -G > $BaSi_2$-B > $BaSi_2$-S. This is in agreement with the absorptance tail in Figure 6.6c. The lower temperature may decrease the degree of the film crystallization and results in a higher concentration of metallic phases within the film [9], which causes the absorptance tail in Figure 6.6c. These metallic phases may also contribute to the increase of the free carrier concentration in Figure 6.5a. Although the film temperatures decrease in FTFA samples, the introduction of the cover in the FTFA can contribute to the formation of their homogeneous surfaces. The lateral thermal conduction in the cover can lead to the heat redistribution at the film surface, especially with Si and $BaSi_2$ cover that hold the higher thermal conductivities, enabling a uniformly surface heating process. Meanwhile, the existence of the cover can slow down the film surface temperature decrease during the cooling process due to their higher thermal resistance as compared to the exposed sample ($BaSi_2$-E), which also benefits for stress relieving of the films.

Interactions in the confined space

Besides the influence on the heat transfer during the annealing and cooling processes, placing the cover on the film provides a confined surface that hinders the gaseous dif-

fusion of residual oxidants in the annealing ambient, for instance, O_2, H_2O, and CO_2, toward the $BaSi_2$ sample surface and suppresses the surface oxidation. These residual oxidants in the vacuum ambient lead to the surface oxidation on $BaSi_2$-E, of which the oxide layer can be up to 100-nm thick [14, 15]. Consequently, the inhomogeneous surface is formed after annealing. The suppression of surface oxidation benefits the surface homogeneity of FTFA samples.

Besides, the solid-phase and solid-gas within the confined space also play an important role in the FTFA. We first look into the most complicated case $BaSi_2$-B. The $BaSi_2$ cover shows a higher reactivity at high temperatures compared to Si and glass covers. In the early stage of annealing, the $BaSi_2$ cover exhibits a higher temperature than that of the $BaSi_2$ film. Consequently, the residual oxidants are inclined to react with $BaSi_2$ cover, as illustrated in Figure 6.8, including the following reactions [9],

$$2BaSi_2 + 5O_2 \rightarrow 2BaO + 4SiO_2, \tag{6.6}$$

$$2BaSi_2 + 2CO_2 + 3O_2 \rightarrow 2BaCO_3 + 4SiO_2, \tag{6.7}$$

$$BaSi_2 + 5H_2O \rightarrow BaO + 2SiO_2 + 5H_2(g), \tag{6.8}$$

$$2BaSi_2 + SiO_2 \rightarrow 2BaO + 5Si. \tag{6.9}$$

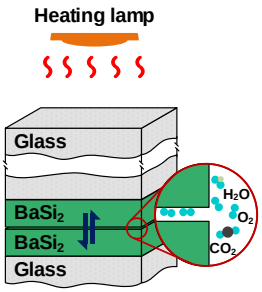

Figure 6.8: Schematic illustration of interaction at the interface between the cover and the film.

Surface oxidation of $BaSi_2$ can be attributed to Equation 6.6 – 6.9, while the formation of Si NCs is the outcome of the reaction between $BaSi_2$ and oxide demonstrated by Equation 6.9. The $BaSi_2$ cover functions as the sacrificial protection layer consuming the oxidants within the confined space. This is proved by the formation of Si NCs at the $BaSi_2$ cover surface. $BaSi_2$ cover demonstrates an inhomogeneous surface with dark and bright areas, as shown in Figure 6.9a. A weak Raman peak of Si NCs at ~519 cm^{-1} can be observed in the spectrum of the dark area, as shown in Figure 6.9b. Meanwhile, more cracks can be noticed at the surface of $BaSi_2$ cover than that of $BaSi_2$ films, suggesting

the non-uniform heat distribution within the cover. This can be ascribed to the surface oxidation and cover surface roughness that alters the radiant flux absorption.

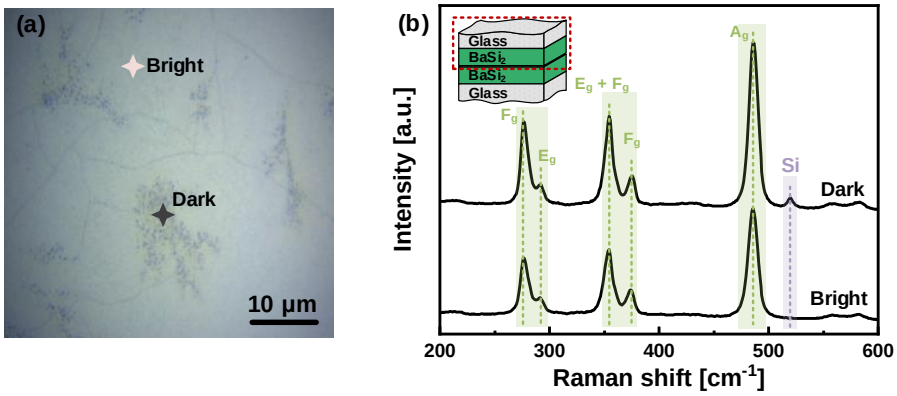

Figure 6.9: (a) Optical microscopy image and (b) Raman spectra collected from the dark and bright areas indicated in (a) of the cover for $BaSi_2$-B.

No obvious change can be noticed at the surface of Si and glass cover, whose temperatures are lower than that of $BaSi_2$ cover. Among them, Si cover may consume part of the oxidants, while the glass cannot decrease the oxidant content. Meanwhile, the rather smooth surface of glass and silicon wafer can reduce the volume of the confined space as well as the content of oxidants. Hence, we can speculate that $BaSi_2$ film surface oxidation degree from severe to mild is in the order of $BaSi_2$ -E $\gg$ $BaSi_2$-G > $BaSi_2$-S $\approx$ $BaSi_2$-B. The suppression of surface oxidation also alleviates the Fe accumulation at the surface layer and the formation of $FeSi_2$ in the FTFA samples.

Besides, the atomic inter-diffusion may also occur during the FTFA, similar to the case of GaAs [16]. Our previous research has revealed the phenomenon of elemental inter-diffusion between $BaSi_2$ and substrates (SiO_x and Si) [9, 15]. Given the lower temperature of the glass cover, we may assume that limited inter-diffusion, majorly Ba diffusion into the glass, occurs at the glass/$BaSi_2$ interface in $BaSi_2$-G [9]. Si and Ba inter-diffusion can occur instead at the interface of Si/$BaSi_2$ in the $BaSi_2$-S. Movements of Si into $BaSi_2$ film and Ba into Si cover can result in a Si-rich composition at the $BaSi_2$ film surface, which can improve its crystallinity [30, 38]. The inter-diffusion at $BaSi_2$/$BaSi_2$ interface in $BaSi_2$-S is hard to be predicted, in which various diffusions may happen due to their high reactivities and higher temperatures.

Owing to the severe surface oxidation, $BaSi_2$-E shows the worst surface crystallinity. The suppression of the oxidation improves the surface crystallinity of the FTFA samples. Additionally, the inter-diffusion at the cover/$BaSi_2$ interface (especially in $BaSi_2$-S and $BaSi_2$-B) may further improve their film surface quality. These results are also in good agreement with the position shift of the A_g Raman peak presented in Figure 6.4.

The oxidation and inter-diffusion at the confined space at the cover/$BaSi_2$ interface (i) significantly alter the properties of the $BaSi_2$ surface, including surface homogeneity, composition, and crystallinity; (ii) may influence the longitudinal elemental diffusion

within the film, which may affect other properties of the film, such as the conduction type and carrier concentration as shown in Figure 6.5a. However, further investigations on bulk properties as well as the optimizations on FTFA parameters, such as temperature, duration, board-range cover materials, heating source (emission wavelength), etc., are needed for a comprehensive understanding of the FTFA mechanism and its effects on $BaSi_2$ films.

6.4. Conclusions

The FTFA approach, with various covers including $BaSi_2$, Si, and glass, is introduced in the post-growth treatment of sputtered $BaSi_2$ films for the material crystallization and thin-film properties improvement from perspectives of surface homogeneity and crystal quality. Impacts of FTFA on sputtered $BaSi_2$ film properties majorly originate from two aspects: i) the employment of the covers in the FTFA alters the heating mechanism of the film from radiation to a combination of radiation and conduction, which results in the lateral and longitudinal heat redistribution within the sample and covers; ii) the confined space produced by the covers and the film grants lower-content residual gaseous oxidants at the film surface and causes the elemental inter-diffusions between the cover and the film, which tailors the film surface properties. These thermal processes and interfacial interactions coordinatively determine the film properties. Optimizations of the FTFA method, including temperature, duration, cover materials, heating source, ambient, etc., are needed for the further improvement and control of the $BaSi_2$ film properties.

References

[1] Y. Tian, M. Zeman, and O. Isabella, *Face-to-face annealed sputtered $BaSi_2$: Investigations on surface homogeneity, film properties, and annealing mechanisms,* Phys. Rev. Materials **4**, 125403 (2020).

[2] T. Suemasu, *Exploring the possibility of semiconducting $BaSi_2$ for thin-film solar cell applications,* Japanese Journal of Applied Physics **54**, 07JA01 (2015).

[3] Q. Deng, H. Chen, H. Liao, L. Chen, G. Wang, S. Wang, and Y. Shen, *Numerical simulation and optimization of Si/$BaSi_2$ heterojunction and $BaSi_2$ homojunction solar cells,* Journal of Physics D: Applied Physics **52**, 075501 (2018).

[4] J.-S. Huang, K.-W. Lee, and Y.-H. Tseng, *Analysis of the high conversion efficiencies $BaSi_2$ and $BaSi_2$ n-i-p thin film solar cells,* Journal of Nanomaterials **2014**, 1 (2014).

[5] S. Yachi, R. Takabe, H. Takeuchi, K. Toko, and T. Suemasu, *Effect of amorphous Si capping layer on the hole transport properties of $BaSi_2$ and improved conversion efficiency approaching 10% in p-$BaSi_2$/n-Si solar cells,* Applied Physics Letters **109**, 072103 (2016).

[6] K. Kodama, R. Takabe, T. Deng, K. Toko, and T. Suemasu, *Spectroscopic evidence of photogenerated carrier separation by built-in electric field in Sb-doped n-$BaSi_2$/B-doped p-$BaSi_2$ homojunction diodes,* Japanese Journal of Applied Physics **57**, 050310 (2018).

[7] K. O. Hara, N. Usami, Y. Hoshi, Y. Shiraki, M. Suzuno, K. Toko, and T. Suemasu, *Structural study of BF_2 ion implantation and post annealing of $BaSi_2$ epitaxial films,* Japanese Journal of Applied Physics **50**, 121202 (2011).

[8] K. O. Hara, K. Arimoto, J. Yamanaka, and K. Nakagawa, *Diffusion process in $BaSi_2$ film formation by thermal evaporation and its relation to electrical properties,* Journal of Materials Research **33**, 2297 (2018).

[9] Y. Tian, R. Vismara, S. Van Doorene, P. Šutta, Ľ. Vančo, M. Veselý, P. Vogrinčič, O. Isabella, and M. Zeman, *Oxidation-induced structure transformation: Thin-film synthesis and interface investigations of barium disilicide toward potential photovoltaic applications,* ACS Applied Energy Materials **1**, 3267 (2018).

[10] K. O. Hara, Y. Hoshi, N. Usami, Y. Shiraki, K. Nakamura, K. Toko, and T. Suemasu, *N-type doping of $BaSi_2$ epitaxial films by phosphorus ion implantation and thermal annealing,* Thin Solid Films **557**, 90 (2014).

[11] M. A. Khan, M. Takeishi, Y. Matsumoto, T. Saito, and T. Suemasu, *Al- and Cu-doped $BaSi_2$ films on Si(111) substrate by molecular beam epitaxy and evaluation of depth profiles of Al and Cu atoms,* Physics Procedia **11**, 11 (2011).

[12] M. Takeishi, Y. Matsumoto, R. Sasaki, T. Saito, and T. Suemasu, *Growth of Al-doped p-type $BaSi_2$ films by molecular beam epitaxy and the effect of high-temperature annealing on their electrical properties,* Physics Procedia **11**, 27 (2011).

[13] K. Hara, Y. Hoshi, N. Usami, Y. Shiraki, K. Nakamura, K. Toko, and T. Suemasu, *Structural study on phosphorus doping of $BaSi_2$ epitaxial films by ion implantation,* Thin Solid Films **534**, 470 (2013).

[14] Y. Tian, A. R. Montes, Ľ. Vančo, O. Isabella, and M. Zeman, *Properties of sputtered $BaSi_2$ thin films annealed in vacuum condition,* Japanese Journal of Applied Physics **59**, SFFA03 (2020).

[15] Y. Tian, A. R. Bento Montes, Ľ. Vančo, M. Čaplovičová, P. Vogrinčič, P. Šutta, L. Satrapinskyy, M. Zeman, and O. Isabella, *Toward $BaSi_2$/Si heterojunction thin-film solar cells: Insights into heterointerface investigation, barium depletion, and silicide-mediated silicon crystallization,* Advanced Materials Interfaces **7**, 2000887 (2020).

[16] H. Kanber, R. J. Cipolli, W. B. Henderson, and J. M. Whelan, *A comparison of rapid thermal annealing and controlled atmosphere annealing of Si-implanted GaAs,* Journal of Applied Physics **57**, 4732 (1985).

[17] G. Nam, Y. Park, I. Ji, B. Kim, S. heon Lee, D. Y. Kim, S. Kim, S.-O. Kim, and J.-Y. Leem, *Facile synthesis and enhanced ultraviolet emission of ZnO nanorods prepared by vapor-confined face-to-face annealing,* ACS Applied Materials & Interfaces **7**, 873 (2014).

[18] H. Miyake, C.-H. Lin, K. Tokoro, and K. Hiramatsu, *Preparation of high-quality AlN on sapphire by high-temperature face-to-face annealing,* Journal of Crystal Growth **456**, 155 (2016).

[19] J. Wang, W. Li, H. Zhang, Y. Xiong, L. Ye, H. Ruan, G. Qin, and C. Kong, *Improved structural and optical properties of β-Ga_2O_3 films by face-to-face annealing,* Applied Physics A **126**, 235 (2020).

[20] T. Suhara, K. Murata, A. Navabi, K. O. Hara, Y. Nakagawa, C. T. Trinh, Y. Kurokawa, T. Suemasu, K. L. Wang, and N. Usami, *Postannealing effects on undoped $BaSi_2$ evaporated films grown on Si substrates,* Japanese Journal of Applied Physics **56**, 05DB05 (2017).

[21] Y. Kimura, M. Fujiwara, Y. Nakagawa, K. Gotoh, Y. Kurokawa, and N. Usami, *Effects of evaporation vapor composition and post-annealing conditions on carrier density of undoped $BaSi_2$ evaporated films,* Japanese Journal of Applied Physics **59**, SFFA05 (2020).

[22] M. Somer, *Vibrational spectra of the cluster anions $[E_4]^{4-}$ in Themetallic Sodium and Barium Compounds Na_4E_4 and Ba_2E_4 (E = Si, Ge),* Zeitschrift für anorganische und allgemeine Chemie **626**, 2478 (2000).

[23] A. G. Birdwell, R. Glosser, D. N. Leong, and K. P. Homewood, *Raman investigation of ion beam synthesized β-$FeSi_2$,* Journal of Applied Physics **89**, 965 (2001).

[24] T. Yoshitake, T. Nagamoto, and K. Nagayama, *Microstructure of β-$FeSi_2$ thin films prepared by pulsed laser deposition,* Thin Solid Films **381**, 236 (2001).

[25] G. Faraci, S. Gibilisco, P. Russo, A. R. Pennisi, and S. L. Rosa, *Modified Raman confinement model for Si nanocrystals,* Physical Review B **73** (2006), 10.1103/physrevb.73.033307.

[26] S. Matsuno, R. Takabe, S. Yokoyama, K. Toko, M. Mesuda, H. Kuramochi, and T. Suemasu, *Significant photoresponsivity enhancement of polycrystalline $BaSi_2$ films formed on heated Si(111) substrates by sputtering,* Applied Physics Express **11**, 071401 (2018).

[27] K. O. Hara, C. T. Trinh, Y. Kurokawa, K. Arimoto, J. Yamanaka, K. Nakagawa, and N. Usami, *Post-annealing effects on the surface structure and carrier lifetime of evaporated $BaSi_2$ films,* Japanese Journal of Applied Physics **56**, 04CS07 (2017).

[28] H. Peng, C. Wang, J. Li, R. Zhang, M. Wang, H. Wang, Y. Sun, and M. Sheng, *Lattice dynamic properties of $BaSi_2$ and $BaGe_2$ from first principle calculations,* Physics Letters A **374**, 3797 (2010).

[29] T. Sato, Y. Yamashita, Z. Xu, K. Toko, S. Gambarelli, M. Imai, and T. Suemasu, *Correlation of native defects between epitaxial films and polycrystalline $BaSi_2$ bulks based on photoluminescence spectra,* Applied Physics Express **12**, 111001 (2019).

[30] R. Takabe, T. Deng, K. Kodama, Y. Yamashita, T. Sato, K. Toko, and T. Suemasu, *Impact of Ba to Si deposition rate ratios during molecular beam epitaxy on carrier concentration and spectral response of $BaSi_2$ epitaxial films,* Journal of Applied Physics **123**, 045703 (2018).

[31] M. F. Modest, *Radiative heat transfer* (Academic press, 2013).

[32] F. Kreith, R. M. Manglik, and M. S. Bohn, *Principles of heat transfer* (Cengage learning, 2012).

[33] H. Shanks, P. Maycock, P. Sidles, and G. Danielson, *Thermal conductivity of silicon from 300 to 1400 K,* Physical Review **130**, 1743 (1963).

[34] Corning Inc., *Corning® EAGLE XG® slim glass substrates for LCD displays,* `https://www.corning.com/worldwide/en/products/display-glass/products/eagle-xg-slim.html`.

[35] E. Magyari and A. Pantokratoras, *Note on the effect of thermal radiation in the linearized rosseland approximation on the heat transfer characteristics of various boundary layer flows,* International Communications in Heat and Mass Transfer **38**, 554 (2011).

[36] S. Rosseland, *Astrophysik: Auf atomtheoretischer grundlage*, Vol. 11 (Springer-Verlag, 2013).

[37] H. Keppler, L. S. Dubrovinsky, O. Narygina, and I. Kantor, *Optical absorption and radiative thermal conductivity of silicate perovskite to 125 Gigapascals,* Science **322**, 1529 (2008).

[38] Y. Yamashita, Y. Takahara, T. Sato, K. Toko, A. Uedono, and T. Suemasu, *Simple way of finding Ba to Si deposition rate ratios for high photoresponsivity in $BaSi_2$ films by raman spectroscopy,* Applied Physics Express **12**, 055506 (2019).

7

Investigations on $Si/BaSi_2/Si$ Structures

Abstract

Knowledge of the structure and composition of $Si/BaSi_2/Si$ heterostructure annealed under high-temperature conditions is a prerequisite for the development of $BaSi_2/Si$ heterojunction thin-film solar cells. For this purpose, $Si/BaSi_2/Si$ heterostructures deposited by magnetron sputtering with different Si layer thickness are submitted to systematic structure and composition characterizations. Results reveal a $BaSi_2/Si$ hetero-interfacial variation caused by surface oxidation and Ba diffusion at the high temperature. Its effects on the optical and electrical properties of $Si/BaSi_2/Si$ heterostructure are presented. The outcomes of this work can be extended to $BaSi_2$ deposited by other techniques, and generate substantial advantages in $BaSi_2$ development ranging from improvement on material qualities and eventual deployment in thin-film solar cells.

Parts of this chapter have been published in Advanced Materials Interfaces, 2000887 (2020) [1].

7.1. Introduction

Preliminary theoretical researches have established various $BaSi_2$ homojunction and heterojunction solar cell architectures. Despite its intrinsically moderate n-type nature (electron concentration $n = 10^{15} - 10^{17}$ cm^{-3}), the conductivity of $BaSi_2$ can be modified by external doping. Dopants, such as P, Sb, Ga, Cu, and As, can enhance the electron concentration to the range of $10^{19} - 10^{20}$ cm^{-3}, while B, Al, Ag, In, etc., would alter it to a p-type conductivity [2–9]. Such bipolar conductivity of $BaSi_2$ facilitates homojunction architectures. Theoretically, the conversion efficiency (η) of an n-p $BaSi_2$ homojunction solar cell can reach 22.5 – 25% [10, 11]. However, controllable $BaSi_2$ doping processes were currently carried out only by Molecular Beam Epitaxy (MBE) with in-situ co-evaporation or ex-situ ion-implantation of dopants [5, 7]. Regardless of expensive and complex equipment involved in processes as well as a restriction of c-Si substrate for depositions, additional high-temperature annealing was needed after the doping process, which caused issues such as the segregation of dopants [5]. In the attempt to obtain $BaSi_2$ homojunction solar cells, n^+-$BaSi_2$ (20 nm)/p-$BaSi_2$ (500 nm)/p^+-$BaSi_2$ (50 nm) diodes experimentally exhibited an extremely low η of 0.1 – 0.28% that could be caused by high-volume of defects [12, 13].

To this end, heterojunction architectures, which have an inherent advantage of being free from doping, exhibit a great promise for $BaSi_2$ solar cell development. The low lattice mismatch between $BaSi_2$ and Si promotes the development of the $BaSi_2$/Si heterojunction [14]. Indeed, the highest experimentally obtained $BaSi_2$-based solar cell with η = 10% was based on a p-$BaSi_2$/n-Si heterojunction configuration [15]. It needs to be addressed that the n-Si wafer instead of p-$BaSi_2$ functioned as the light absorber in the solar cell, which failed to take the full advantage of $BaSi_2$. To release the vast potential of $BaSi_2$, various heterojunction thin-film solar cell architectures based on well-established Si solar cell technology have been proposed, wherein $BaSi_2$ is employed for light absorption [16]. Simulations on the device level have revealed the great promise of $BaSi_2$/Si solar cells, for instance, a p^+-Si (100 nm)/$BaSi_2$ (2000 nm) solar cell can achieve a η = 22.7%, and an n-Si/$BaSi_2$/p-Si architecture possesses a potential efficiency up to 30.4% [11, 17]. Heterojunction architectures allow state-of-the-art photovoltaic techniques, such as tandem solar cells, bandgap engineering, and light management, to experimentally obtain these attractive efficiencies [18]. Meanwhile, industrially applicable techniques for $BaSi_2$ absorber layer deposition, for instance, vacuum evaporation and sputtering, can be feasibly adopted in $BaSi_2$/Si solar cell manufacturing [19–22]. However, the high-temperature condition involved either in film growth or post-growth annealing processes can result in issues such as elemental inter-diffusion and thermal-stress mismatch, which would generally degrade the device performance or, even worse, lead to an inoperative solar cell. To reach the goal of efficient $BaSi_2$/Si heterojunction thin-film solar cells, it is of significant necessity and urgency to uncover the $BaSi_2$/Si hetero-interface behaviors during the high-temperature process and their effects on film properties.

Herein, we present a hetero-interfacial investigation of Si/$BaSi_2$/Si architectures prepared by room-temperature sputtering with post-annealing treatments. Comprehensive analyses on structural and compositional variations of Si/$BaSi_2$/Si architectures can reveal substantial physical and chemical reactions between Si and $BaSi_2$. The influence of the Si layer thickness on $BaSi_2$ properties also serves as a guide for material devel-

opment. These pieces of knowledge would contribute to the development of $BaSi_2$/Si heterojunction solar cells.

7.2. Experimental

7.2.1. Fabrications of Si/$BaSi_2$/Si structures

$BaSi_2$ and Si layers were deposited by a radio-frequency magnetron sputtering setup with a stoichiometric $BaSi_2$ target and an intrinsic Si target (99.999 %, Kurt J. Lesker), respectively. The sputtering chamber was pumped down to a pressure lower than 5×10^{-4} Pa after placing the substrate inside. An Ar gas flow was introduced for sputtering. Prior to the deposition, targets were pre-sputtered for cleaning. The plasma power density and deposition pressure of $BaSi_2$ and Si were set as 0.617 W/cm^2 and 1 Pa, and 0.601 W/cm^2 and 0.3 Pa, respectively. All films were deposited at room temperature. Depositions of $BaSi_2$ and Si were carried out in the same chamber without breaking the system vacuum to diminish the impact of surface oxidation. Two Si layers with the same thickness (d_{Si}) ranging from 0 to 50 nm, were deposited to sandwich a $BaSi_2$ layer. Thus, samples with the architecture of Si/$BaSi_2$/Si/Substrate were obtained. Subsequent annealing processes were carried out at 600 °C in a high vacuum environment ($p < 10^{-4}$ Pa) enabling the $BaSi_2$ crystallization. The thickness of the $BaSi_2$ layer was kept constant at around 700 nm. That was considered sufficiently thick to isolate surface reactions from bulk crystallization upon high-temperature annealing.

Corning glass and c-Si wafer substrates were employed for depositions. To eliminate the influence of wafer crystalline orientation on the film growth, c-Si substrates were covered with a 200-nm intrinsic polycrystalline Si (poly-Si) layer that was deposited by low-pressure chemical vapor deposition (LP-CVD) with high-temperature annealing at N_2 atmosphere. Native oxide on the poly-Si layer was removed by a short dip in 5 vol% HF solution before the depositions.

7.2.2. Characterizations

The X-Ray diffraction (XRD) patterns were obtained by an automatic powder X-ray diffractometer X'Pert Pro equipped with an ultrafast linear semiconductor detector PIXcel and on a point proportional detector. Cu Kα radiation (λ = 0.154 nm) was used as an X-ray source. The X-ray incidence angle of ω was fixed at 0.5°. Raman spectra were recorded on a Renishaw InVia^{TM} confocal Raman microscope with 633-nm laser excitation. Raman mapping was done in Streamline mode using a 50× objective with a scan area of 20 × 20 μm^2. The acquisition time per scan was 10 s. The Raman spectra were fitted with Renishaw WiRE^{TM} by using broadened Gaussian/Lorentzian line shapes, and corresponding Raman intensity maps were created from fitted results. Elemental compositions were analyzed by a Jeol JAMP 9510-F Auger microprobe at 10 keV energy with a tilt angle of 30°and 65°take-off angle. Depth profiling was conducted by sputtering with 1000 eV Ar^+ ions. Secondary electron images (SEI) and back-scattered electron images (BEI) were also recorded in topographic and compositional regimes using the same device. Root mean square roughness was measured by an atomic force microscope (AFM, NT-MDT nTegra). Nano-structural characterization of the cross-sectional samples was done using a double corrected JEOL JEM ARM200cF scanning transmission electron microscope

(STEM) equipped with a cold field emission gun operated at 200 kV. All data were processed with Digital Micrograph GMS 3.21 (Gatan). Energy dispersive X-Ray spectroscopy (EDS) spectral images were acquired using a JEOL JED-2300 CENTURIO silicon drift detector (SDD) collecting X-rays with an effective solid angle 0.98 sr and a detection area of 100 mm^2. EDS measurements were performed using a probe current of 200 pA. The EDS energy range was 20 keV (10 eV/channel). EDS atomic maps with 256 × 256 pixels were acquired with 200 frames and a 0.1 ms dwell time.

For electrical characterizations, Al contacts were deposited by vacuum evaporation (PRO500S, Provac), and were subsequently annealed at 130 °C for 30 min to ensure ohmic contact. Resistivity and Hall effect measurements were conducted with van der Pauw geometry to determine the majority carrier type and concentration. A temperature-dependent current-voltage (I-V) setup was employed to measure the film conductivity. Wavelength dependent reflectance and transmittance were obtained on a Perkin Elmer Lambda 950 UV-Vis-NIR spectrometer single beam instrument over a range of 300-2500 nm.

7.3. Results and discussion

7.3.1. Bulk composition analysis

Figure 7.1 shows XRD patterns of Si/$BaSi_2$/Si structures with Si layer thickness (d_{Si}) ranging from 0 to 50 nm. For notation simplicity, samples were denoted as $BaSi_2$/Si-d_{Si}, e.g., $BaSi_2$/Si-20 represented a $BaSi_2$ layer that was sandwiched by two 20-nm Si layers. XRD signatures of $BaSi_2$ can be observed in all samples, confirming the presence of crystalline $BaSi_2$ in the Si/$BaSi_2$/Si structures. All samples exhibit similar XRD peak profiles regardless of peak intensity difference. This suggests that the employment of Si layers does not lead to a substantially compositional variation of Si/$BaSi_2$/Si structures. Besides signals from $BaSi_2$, traces of β-$FeSi_2$ are also captured [23]. The origin of Fe can be from contamination in targets or deposition environments.

Despite being annealed *in vacuo*, samples still experience surface oxidation owing to vacuum contaminations, i.e., residual O_2 and CO_2 [22, 24]. It results in surface heterogeneity of samples, as depicted by optical microscopic images in Figure 7.2. Raman spectra collected from different positions indicated in Figure 7.2 are presented in Figure 7.3. In a good agreement with XRD results, Raman spectra also reveal the mixed composition of samples. Along with the typical $BaSi_2$ Raman peaks, namely F_g (~276 cm^{-1}), E_g (~293 cm^{-1}), E_g+F_g (~355 cm^{-1}), F_g (~376 cm^{-1}), and A_g (~486 cm^{-1}), peaks of β-$FeSi_2$ at 247 cm^{-1} and Si nanocrystals (NCs) at 519 cm^{-1} are observed as well [25–27].

In $BaSi_2$/Si-0, positions (−3, 7) and (0, 0), which hold different appearances (see Figure 7.2a), present the same Raman spectra shape, consisting of strong signals from $BaSi_2$, β-$FeSi_2$, and a week peak of Si NCs, as shown in Figure 7.3a. By introducing Si layers, $BaSi_2$/Si-10 and -20 present sharper color contrast in microscopic images displayed in Figure 7.2b and 7.2c, respectively. Such contrast is also reflected by Raman spectra. As shown in Figure 7.3c and 7.3d, position (−5, −2) of $BaSi_2$/Si-10 shows a spectrum without an obvious Si-NCs peak, while the spectrum of position (−2, 2) at $BaSi_2$/Si-20 surface does not contain the peak of β-$FeSi_2$. Further increasing d_{Si} to 50 nm, $BaSi_2$/Si-50 exhibits a lower color contrast of the surface (see Figure 7.2d). And different positions at

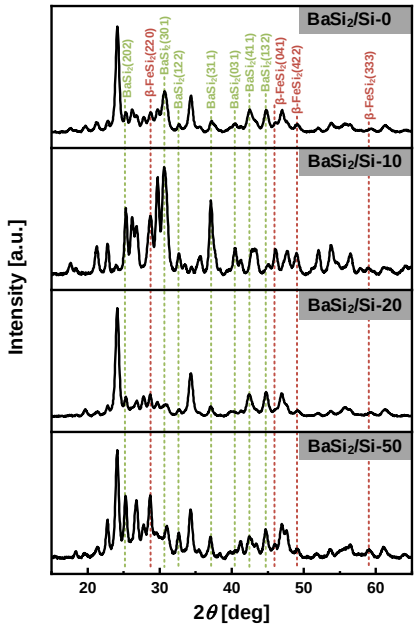

Figure 7.1: XRD patterns of Si/$BaSi_2$/Si samples. Typical peaks from $BaSi_2$ and β-$FeSi_2$ are marked.

the surface possess the same Raman spectrum shape, which contains a stronger Si-NCs peak but without the β-$FeSi_2$ peak compared to that of $BaSi_2$/Si-0.

Raman micro-spectroscopic mapping is carried out at the areas indicated in Figure 7.2, to analyze the surface heterogeneity of samples. Intensities of the characteristic vibrational peaks from $BaSi_2$ (A_g, ~486 cm^{-1}), β-$FeSi_2$ (~247 cm^{-1}), and Si NCs (~519 cm^{-1}) are extracted from the fitted spectra. Figure 7.4 visualizes their spatial dependencies in the format of pixel-based images.

As shown in Figure 7.4, Raman peak intensity maps are consistent, as expected, with the color patterns in optical microscopic images (see Figure 7.2). $BaSi_2$/Si-0 presents relatively low peak-intensity difference over the measured area, corresponding to the same Raman spectrum shape of different positions in Figure 7.3a. Conversely, two distinct areas, i.e., a Si-rich grain area and a Ba-rich filling area, are shown in maps of $BaSi_2$/Si-10. The Si-rich area displays strong Si NCs signal as illustrated by the lighter area in Figure 7.4j, while the Ba-rich area is more yellowish or reddish in Figure 7.4b reflecting the higher content of $BaSi_2$. Meanwhile, the peak intensity distributions of $BaSi_2$ (depicted by Figure 7.4b) and β-$FeSi_2$ (presented in Figure 7.4f) are the reverses of that found for Si NCs (displayed in Figure 7.4j). Understandably, less Si NCs means more Si atoms would be bounded with Ba and Fe. Such co-variation of peak intensity between Si NCs with $BaSi_2$ and β-$FeSi_2$ is also observed in $BaSi_2$/Si-0 and -20. On the contrary, in $BaSi_2$/Si-50, the area that presents a stronger intensity of Si NCs also exhibits higher intensities of $BaSi_2$ and β-$FeSi_2$. One can assert that the compositional and structural alteration of

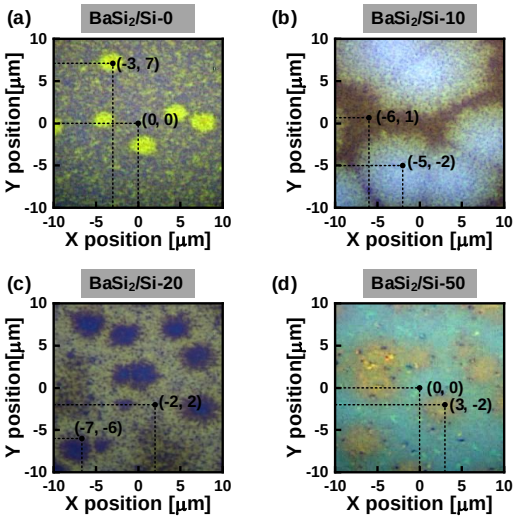

Figure 7.2: Optical microscopic image of mapping areas from samples (a) BaSi2/Si-0, b) $BaSi_2$/Si-10, c) $BaSi_2$/Si-20, and d) $BaSi_2$/Si-50.

Si/$BaSi_2$/Si structure is closely tied up to the thickness of the Si layer.

The detailed statistical distributions of Raman peak intensity are shown in Figure 7.5. With the increase of d_{Si}, we note an obvious increase of Si NCs average intensity, which is understandable given a thicker deposited Si layer. On the other hand, the β-$FeSi_2$ intensity drastically declines, which is almost down to zero in $BaSi_2$/Si-50. Thus, the thicker Si layer can efficiently suppress the formation of β-$FeSi_2$ at the surface region. It needs to be addressed that d_{Si} does not significantly influence the $BaSi_2$ peak intensity.

Figure 7.6 shows backscattered electron composition mode (BEI-Compo) and secondary electron images (SEI) micrographs of $BaSi_2$/Si-0, -10, and -50. In the BEI-Compo images, dark areas hold the lower mean atomic number that herein corresponds to the Si-rich composition with a depth of around 100 nm, which is consistent with the Auger depth profiles in Figure 7.7. While light areas are Si-depleted and therefore present the Ba-rich composition. As presented in Figure 7.6a, the surface of $BaSi_2$/Si-10 consists of Si-rich grain areas and Ba-rich filling areas, which also perfectly coincides with the results of Raman mapping (see Figure 7.4b and 7.4j). With the increase of d_{Si}, Ba releases from the prepared structure during annealing, not only in-between the Si-rich grains but also in their centers, as shown in Figure 7.6b. In Figure 7.6c related to sample $BaSi_2$/Si-50, Ba is distributed over the majority of the surface.

The Ba diffusion also induced an obvious change of surface morphology. Compared to the surface of $BaSi_2$/Si-10 (see Figure 7.6d), Ba-rich islands are distributed in the surface of $BaSi_2$/Si-20, illustrated by the light dots in Figure 7.6e. The size of Ba-rich islands becomes smaller at the surface of $BaSi_2$/Si-50 shown in Figure 7.6f. This also resulted in different surface roughness. $BaSi_2$/Si-10, $BaSi_2$/Si-20, and $BaSi_2$/Si-50 hold Rq values

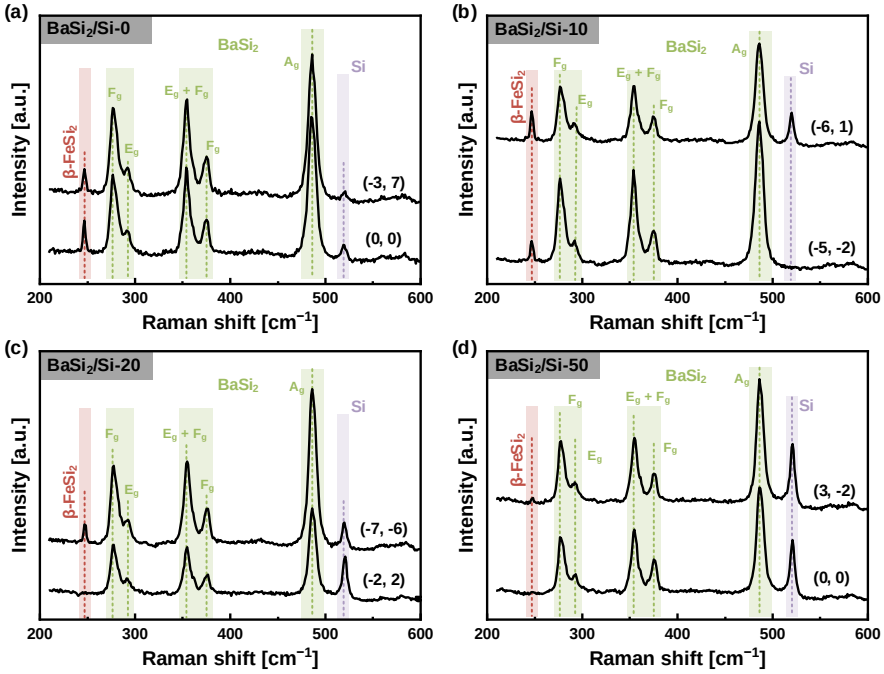

Figure 7.3: Raman spectra of (a) $BaSi_2$/Si-0, (b) $BaSi_2$/Si-10, (c) $BaSi_2$/Si-20, and (d) $BaSi_2$/Si-50. Raman spectra were collected from different areas at the surface of samples.

of 38.27 nm, 167.5 nm, and 52.08 nm, respectively. The wide distribution of small-size Ba-rich islands at $BaSi_2$/Si-50 surface decreases its surface roughness compared to that of $BaSi_2$/Si-20.

Figure 7.7a and 7.7b depict the Auger electron spectroscopy (AES) compositional depth profiles of the Ba-rich and Si-rich areas from $BaSi_2$/Si-10 presented in Figure 7.6a, respectively. A surface oxide layer, majorly composed of BaO and SiO_2, can be noticed in both two areas. Differently, a Si layer that is buried under the oxide layer, here denoted as sup-Si, can be observed in Figure 7.7b. The presence of the sup-Si layer leads to the Si-rich composition of that area. Additionally, the Si-rich area presents a thinner surface oxide layer compared to that of the Ba-rich area. This is related to the existence of the sup-Si layer that hinders the growth of the oxide layer.

Indeed, the surface oxide layer thickness decreases with the increase of d_{Si}, which is reasonable given the thicker sup-Si layer resulting from the growing supply of Si atoms. Eventually, $BaSi_2$/Si-50 exhibits an extremely thin surface oxide layer (less than10-nm thick), as presented in Figure 7.7d. Thicker deposited Si layer can effectively alleviate surface oxidation of the Si/$BaSi_2$/Si structure. Owing to the rough surface morphology, it is difficult to carry out AES analysis at different areas of samples $BaSi_2$/Si-20 and -50 shown in Figure 7.6. The analyzed areas of them are displayed in Figure 7.8.

Looking deeply into the Si(-Si) profile in Figure 7.7d, one can notice a Si(-Si) concentration dip at the depth of around 50 nm. This dip corresponds to a concentration

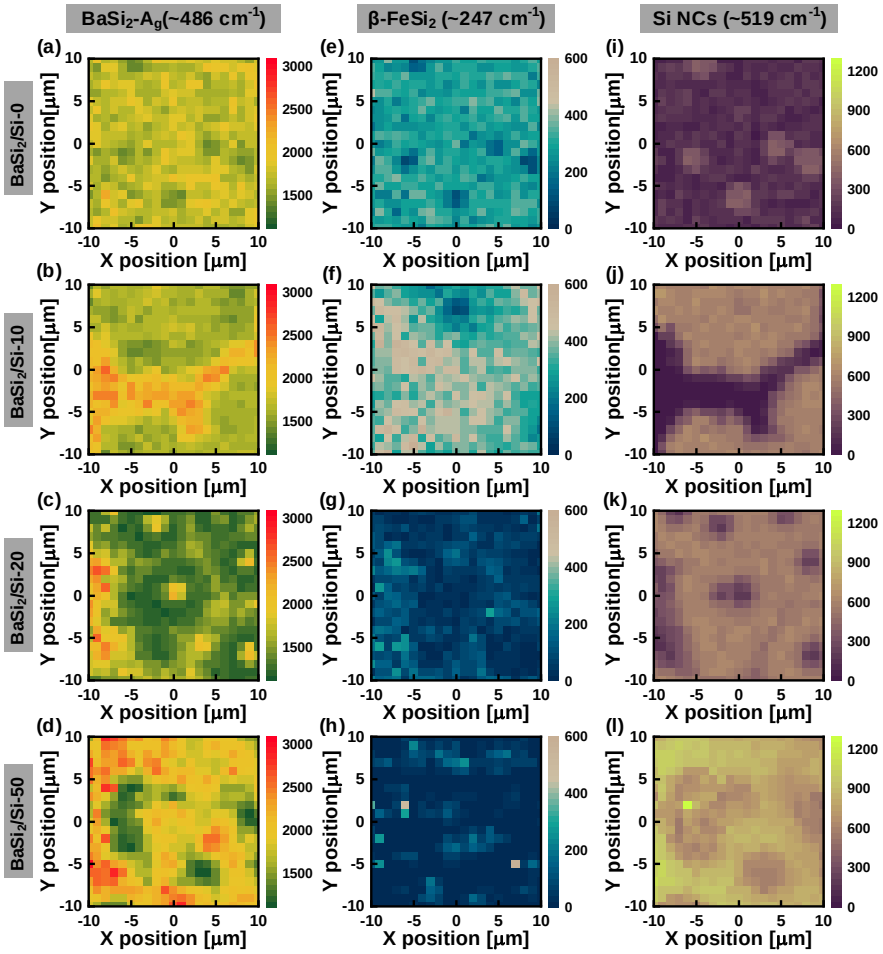

Figure 7.4: Raman mapping of peak intensity distributions of a-d) the strongest vibrational band of $BaSi_2$ A_g at ~486 cm^{-1}, e-h) β-$FeSi_2$ band at ~247 cm^{-1}, and i-l) Si NCs band at ~519 cm^{-1} in a series of deposited a-Si thicknesses of 0, 10, 20, and 50 nm. A measured area of 20×20 μm^2 is shown in each case, along with the scale bar labeled with peak intensity in arbitrary unit. The Raman map pixel size is 1×1 μm^2.

increase of BaO. Thus, the surface region is consequently divided into a double-Si-layers structure by the BaO layer. Moreover, Ba(-Si), as an indicator of $BaSi_2$ existence, can also be detected within the sup-Si layer. The formation of $BaSi_2$ and BaO in the sup-Si layer can result from the Ba diffusion, which is in great agreement with the Ba-release phenomenon revealed by SEM micrographs presented in Figure 7.6. On the other side of the Si/$BaSi_2$/Si sandwich structure, Ba atoms also penetrate through the bottom Si layer, denoted as sub-Si, and even diffuse into the poly-Si substrate. Such phenomena of Ba diffusion into the substrate layer are observed in all samples. Interestingly, the shapes

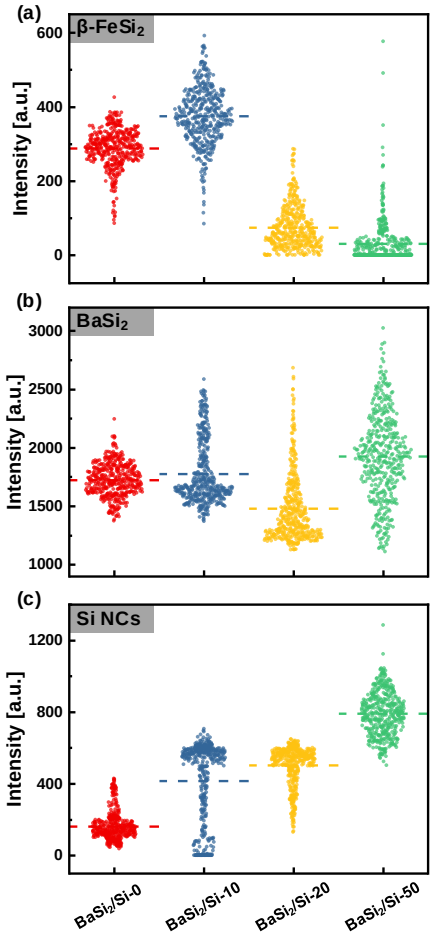

Figure 7.5: Statistical results of Raman intensities of peaks of (a) β-$FeSi_2$, (b) A_g from $BaSi_2$, and (c) Si NCs.

of elemental profiles, including Si(-Ba), Ba, Si(-Si) in the sample $BaSi_2$/Si-50, indicate an overall similarity of structural transformation between sup-Si/$BaSi_2$ and $BaSi_2$/sub-Si interfaces. This reasonably stands for the effectiveness of the thicker sup-Si layer for oxygen exclusion in the $BaSi_2$ surface region.

Apart from hetero-interface, $BaSi_2$ bulk from all samples displays a good stoichiometry of Ba/Si = 1/2. Note that oxygen atoms are incorporated with $BaSi_2$ in all samples with an atomic concentration of around 10%. According to our previous study, oxygen here is originated from the sputtering process, as it can be detected in as-deposited samples as well (see Figure 4.7).

Elemental distributions of impurities, including Fe, N, and C, are profiled in Figure 7.10. In the as-deposited sample, impurities of only Fe and N are detected. Fe, in the form of β-$FeSi_2$, is uniformly distributed throughout the $BaSi_2$ bulk with an atomic con-

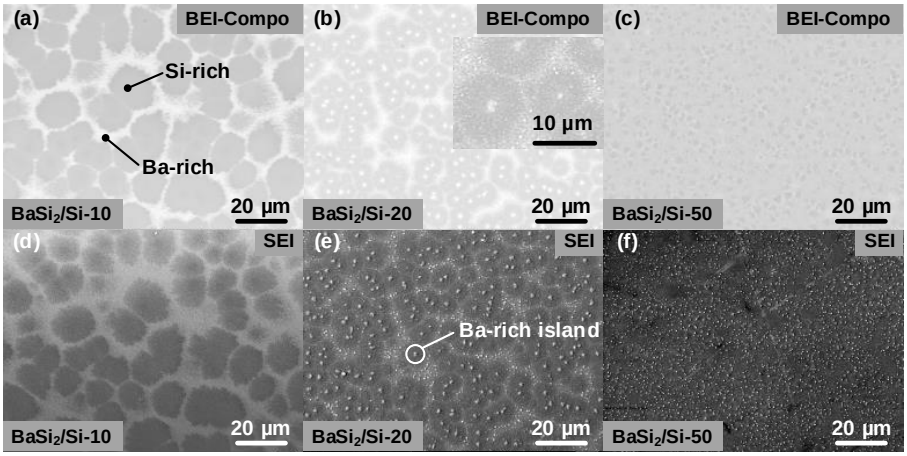

Figure 7.6: Top-view SEM micrographs under imaging conditions of BEI-Compo mode (a) $BaSi_2$/Si-10, (b) $BaSi_2$/Si-20, and SEI mode for (c) $BaSi_2$/Si-10, and for (d) $BaSi_2$/Si-10, (e) $BaSi_2$/Si-20, and (f) $BaSi_2$/Si-50.

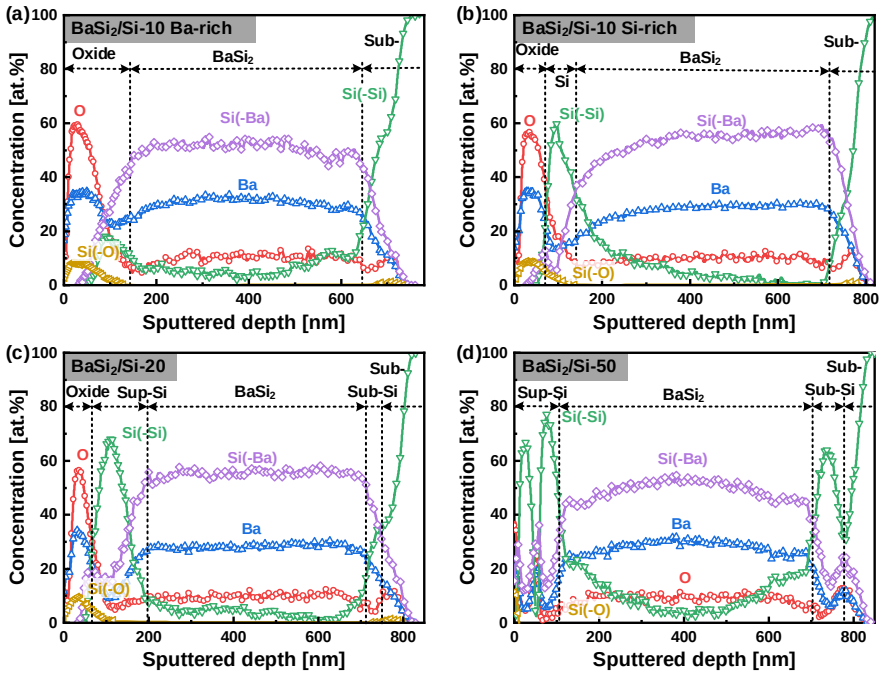

Figure 7.7: Auger electron spectroscopy compositional depth profiles of (a) $BaSi_2$/Si-10 Ba-rich area, (b) $BaSi_2$/Si-10 Si-rich area, (c) $BaSi_2$/Si-20, and (d) $BaSi_2$/Si-50. Si(-Ba), Si(-Si), and Si(-O) represent Si atoms that are bonded with Ba, Si, and O, respectively.

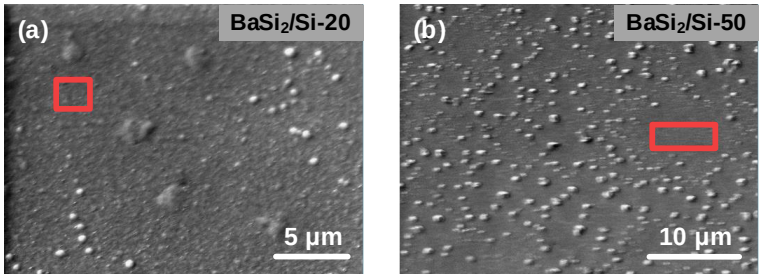

Figure 7.8: AES detected area of (a) $BaSi_2$/Si-10, and (b) $BaSi_2$/Si-20.

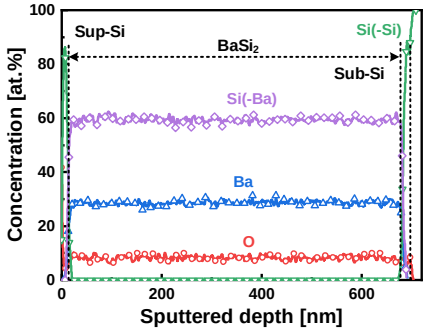

Figure 7.9: Elemental depth profiles of impurities, including C, N, and Fe, of (a) as-deposited $BaSi_2$/Si-10, and annealed samples of (b) $BaSi_2$/Si-0, (c) Ba-rich area in $BaSi_2$/Si-10, (d) Si-rich area in $BaSi_2$/Si-10, (e) $BaSi_2$/Si-20, and (f) $BaSi_2$/Si-50.

centration of ~4%. It suggests that Fe is likely from the $BaSi_2$ target. While N is only detected in the Si layer. It is hard to speculate its origin from either the Si target or vacuum contamination. On the other hand, C is mainly noticed in the very surface region of samples, which can be a consequence of the reactions between Ba and CO_2 from the annealing atmosphere plus the very thin surface contamination of hydrocarbons present in whichever sample.

Cross-sectional scanning transmission electron microscopy (STEM) results are shown in Figure 7.11. The $BaSi_2$ crystallite in $BaSi_2$/Si-20, as shown in Figure 7.11a, is determined to be orthorhombic (Powder diffraction file, PDF, number 98 009 4260) by the evaluation of the relevant Fast Fourier Transform (FFT) pattern. The bright-field (BF) STEM micrograph of the $BaSi_2$ layer shown in Figure 7.11b, associated with its corresponding Energy-dispersive X-ray spectroscopy (EDS) analyses reported in Figure 7.11c-7.11f, confirms the compositional state consisting of $BaSi_2$, BaO, β-$FeSi_2$, Si-NCs, as well as amorphous Si (a-Si).

The $BaSi_2$/sub-Si/poly-Si interfacial structure of $BaSi_2$/Si-20 is shown in Figure 7.11g. The 20-nm sub-Si layer can be noticed, which majorly presents an amorphous state with limited crystalline phases. The brightness contrast of the sub-Si layer suggests the existence of heavier atoms likely Ba Owing to its diffusion into the Si layer. Figure 7.11h is

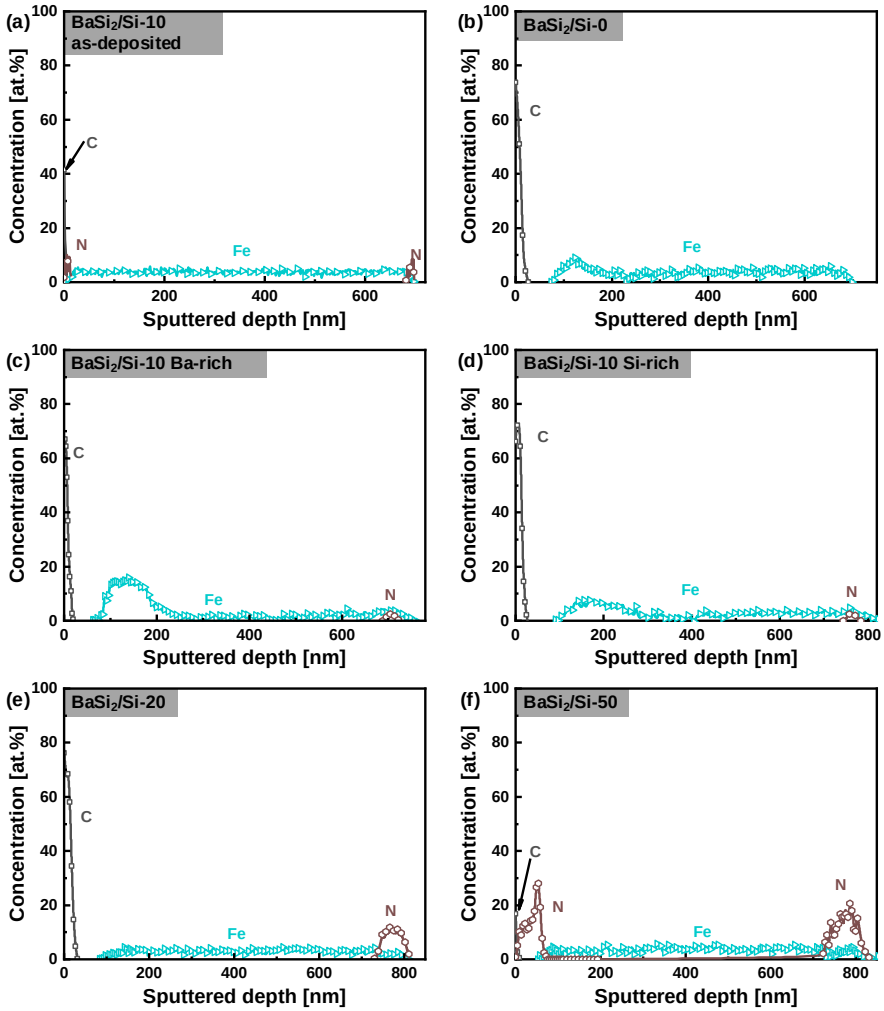

Figure 7.10: AES elemental depth profile of as-deposited $BaSi_2$/Si-10.

a high-resolution TEM (HRTEM) image of $BaSi_2$ crystallite. The $BaSi_2$ crystallite size is about 85 nm. Here, $BaSi_2$ is orthorhombic as well. Figure 7.11i further presents a mixture of crystalline $BaSi_2$ grains and amorphous phases. The 101 planes of orthorhombic $BaSi_2$ with a space of 0.7 nm is shown.

The overall cross-sectional layer structure of $BaSi_2$/Si-50 is depicted by Figure 7.11j and 7.11k. From the top down, sup-Si, $BaSi_2$, and sub-Si layers can be identified. BF and High-angle Annular Dark-field (HAADF) STEM images shown in Figure 7.11j and 7.11k, together with EDS maps presented in Figure 7.11l-7.11n, confirm the layer structure shown in Figure 7.7d. The Ba penetration into both sup- and sub-Si layers is revealed by Ba distribution in Figure 7.11l, owing to which Ba-depleted areas form the interfacial

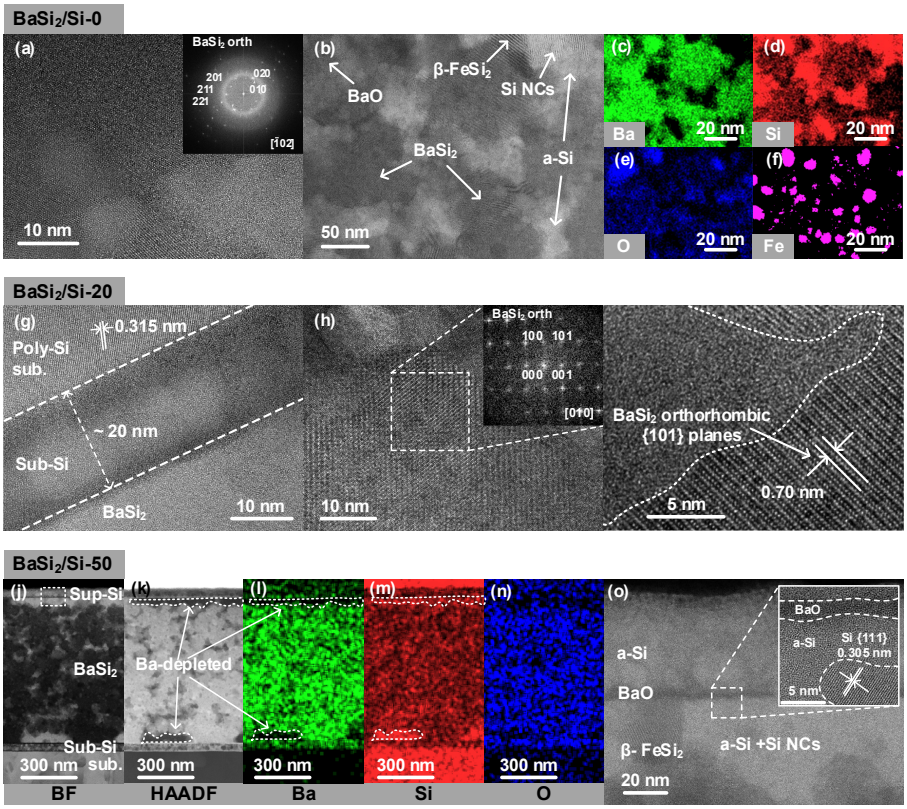

Figure 7.11: (a) BF-STEM micrograph of $BaSi_2$/Si-0 with the corresponding FFT pattern. (b) BF-STEM micrograph of $BaSi_2$ layer of $BaSi_2$/Si-0. (c-f) STEM-EDS maps of Ba, Si, O, and Fe, respectively, from the area in b. (g) BF-STEM micrograph of the interfacial region of the poly-Si/Si/$BaSi_2$ of sample $BaSi_2$/Si-20. (h) HR-TEM micrograph of $BaSi_2$ layer in $BaSi_2$/Si-20. Inset is the FFT obtained from the dashed-line boxed area. (i) HR-TEM micrograph of crystalline $BaSi_2$ and the amorphous phase. (j) BF-STEM micrograph, k) HAADF-STEM micrograph, and corresponding EDS maps of (l) Ba, (m) Si, and (n) O from sample $BaSi_2$/Si-50. (o) BF-STEM micrograph of $BaSi_2$/Si-50 surface indicated by the boxed area of j, the inset is the HR-STEM micrograph of the boxed area in o.

regions within the $BaSi_2$ layer. In fact, such a Ba-depleted area presents a Si-rich composition, in which area isolated Si atoms are partly crystallized as Si NCs. The detailed surface structure is shown in Figure 7.11o. The surface region is separated by a BaO layer into two layers, corresponding to the double-Si-layers structure in Figure 7.7d. Further looking into the surface structure, the upper sup-Si layer contains majorly a-Si, while the lower sup-Si layer rather consists of a-Si and Si-NCs (see the inset in Figure 7.11o), together with β-$FeSi_2$ crystallites.

Generally, four mechanisms can be distinguished during the structural and compositional alteration of Si/$BaSi_2$/Si structures based on the above analyses:
i) Early-stage surface oxidation of deposited-Si layer. Even though the annealing process is carried out in a high-vacuum condition, the eventual presence of contaminations,

for instance, O_2 and CO_2, cannot be ignored. This facilitates the surface oxidation of the deposited-Si layer. Such Si-layer oxidation occurs at the early stage of the annealing. The major product of the reaction is SiO_2.

ii) Growth of surface oxide layer driven by the Ba diffusion. The further growth of the oxide layer at the Si surface is determined by the d_{Si}. Considering the high-temperature condition during the annealing, the effects of Ba diffusion does count. The case of a thin Si layer, for instance, $BaSi_2$/Si-10, is illustrated in Figure 7.12a. Ba can easily diffuse through the thin Si layer, given the amorphous state of the deposited Si layer and the high diffusivity of Ba. A reasonable large amount of Ba atoms reaches the oxide layer or even the oxide surface. These Ba atoms lead to an oxide layer thickness increase as well as a compositional alteration from SiO_2 to an eventual mixture of SiO_2 and BaO, as shown in Figure 7.7. Such process follows the reaction paths [22]:

$$SiO_2 + 2Ba \rightarrow 2BaO + Si \tag{7.1}$$

$$Si + O_2 \rightarrow SiO_2 \tag{7.2}$$

$$2Ba + O_2 \rightarrow 2BaO \tag{7.3}$$

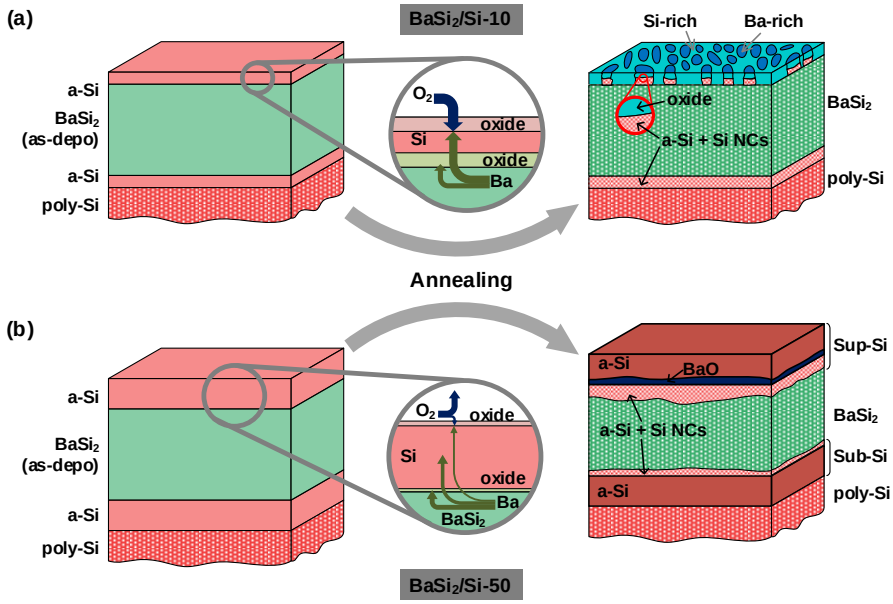

Figure 7.12: Schematic illustration of the structural variation of Si/$BaSi_2$/Si heterostructure: (a) $BaSi_2$/Si-10 and (b) $BaSi_2$/Si-50 after the thermal annealing process.

Eventually, the surface of $BaSi_2$/Si-10, no matter Si-rich or Ba-rich areas, is covered with a several-tens-to-hundreds-nanometers oxide layer that is composed of BaO and

SiO_2, as shown in Figure 7.7a and 7.7b. Once the oxide layer is thick enough to cut off the oxygen supply from the annealing environment, the growth rate of oxide decreases, and the oxide reaches a nearly constant thickness.

If the Si is sufficiently thick that a limited amount of Ba can penetrate through it, then the most of the mass transport takes place beneath the oxide and is most likely associated with the Ba movement within the Si layer. This the case of $BaSi_2$/Si-50, visualized in Figure 7.12b. The oxidation then is confined to the Si surface with a thickness as low as several nanometers as shown in Figure 7.7d. That limited amount of Ba atoms arrives at the surface and forms the Ba islands shown in Figure 7.6f.

iii) Depletion of Ba at oxide/$BaSi_2$ and Si/$BaSi_2$ interfaces. The Ba depletion is caused by the reactions between oxide and Ba that cause the longitudinal diffusion and/or the lateral migration of Ba. Due to the extremely low content of O_2 in the annealing environment ($p < 10^{-4}$ Pa), we can expect non-uniform surface oxidation of samples. It also leads a non-uniform oxide growth towards $BaSi_2$ bulk. As discussed above, the thin Si layer in $BaSi_2$/Si-10 cannot curb the oxide growth into the $BaSi_2$ bulk. The non-uniformly distributed oxide can drag the Ba to migrate laterally due to the reaction described in Equation 7.1. Such redistribution of Ba atoms enables the formation of Si-rich areas that are Ba-depleted and the Ba-rich areas that Ba atoms move to. The relatively intensive surface oxidation of $BaSi_2$/Si-10 brings a high volume of Ba migration, and then results in obvious Ba-rich and Si-rich areas at its surface as shown in Figure 7.6a. Conversely, these Ba-rich and Si-rich areas can be hardly distinguished at the surface of $BaSi_2$/Si-50, presented in Figure 7.6c. Although, STEM images imply the existence of Ba-depleted regions at Si/$BaSi_2$ heterointerfaces in $BaSi_2$/Si-50, as shown in Figure 7.11k and Figure 7.11l. The formation of these Ba-depleted regions is related to the native oxide of $BaSi_2$ and poly-Si substrate. This process is similar to the case of $BaSi_2$/Si-10. Differently, the limited amount of oxide restrains the depletion of Ba. And these Ba-depleted regions are buried beneath the thick Si layer or the whole Si/$BaSi_2$/Si structure. Thus, there is no obvious Ba-rich or Si-rich area at the $BaSi_2$/Si-50 surface. Additionally, reactions at Si/$BaSi_2$ heterointerface produce the outcome such as BaO, which is indicated by the double-Si-layer structure in Figure 7.7d and 7.11o.

iv) Si isolation and crystallization. Si atoms are isolated at the $BaSi_2$ side of the oxide/$BaSi_2$ and Si/$BaSi_2$ interface due to the Ba movement. According to AES and STEM analyses, these Si atoms can either stay amorphous state or form Si crystallites Owing to the so-called silicide-mediated Si crystallization [28, 29]. This phenomenon is clearer in $BaSi_2$/Si-50. As shown in Figure 7.11m, an intensive Si signal in the EDS map can be overserved at the Ba-depleted area. And the HRTEM image in Figure 7.11o further proves the presence of both amorphous and crystalline Si phases. The formation of the amorphous phase is understandable given the original nature of as-deposited $BaSi_2$. Before being crystallized, part of Ba diffuses out and leave the amorphous state Si. In the path of propagating to the surface layer, Ba passes by the amorphous state Si and can form $BaSi_2$ crystallites. Yet, Ba can still diffuse out of $BaSi_2$ lattice and leads the formation of Si crystallites, which is similar to the nickel-silicide-mediated Si crystallization [28]. To examine it, samples with a structure of 20-nm Si/20-nm $BaSi_2$, 20-nm $BaSi_2$, and 20-nm Si are annealed at the same condition (600 °C for 30 min). As proven by the Raman spectra in Figure 7.13, only samples endowed $BaSi_2$ exhibit the peak of Si NCs at ~519 cm^{-1}.

And the strongest Si NCs peak, as expected, is shown in the spectrum of sample Si (20 nm)/$BaSi_2$(20 nm). Isolation and crystallization of Si result in both sup- and sub-Si layers composed of a-Si and Si-NCs in $BaSi_2$/Si-50, presented in Figure 7.12b. Similarly, Si NCs forms at Si-rich are at the surface of $BaSi_2$/Si-10 illustrated in Figure 7.12a.

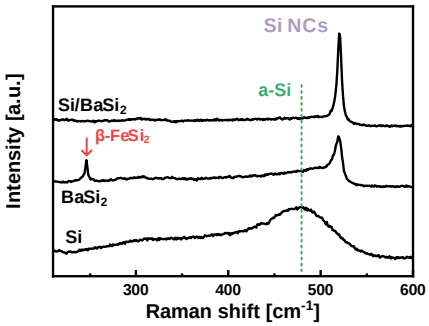

Figure 7.13: Raman spectra of the 20-nm Si layer, 20-nm $BaSi_2$ layer, and 20-nm Si/20-nm $BaSi_2$. All samples were annealed at 600 °C for 30 min.

Accordingly, the complex multi-layer structures of Si/$BaSi_2$/Si samples revealed by previous structural and compositional characterizations are obtained after annealing, which is depicted in Figure 7.12. Such a multi-layer system enables further interface engineering of $BaSi_2$, because the $BaSi_2$ bulk in $BaSi_2$/Si-50 is completely protected by the Si layers even at the high-temperature condition.

7

7.3.2. Electrical and optical properties

Wavelength-based absorptance curves are displayed in Figure 7.14, which are derived from reflectance and transmittance curves, presented in Figure 7.15. The thickness of Si does not make a significant difference in the absorptance of samples. A clear absorption edge near the reported bandgap energy of $BaSi_2$ (1.25 to 1.35 eV) can be observed in the absorptance curve of all samples. The high absorptance around 90% at near-UV and visible spectral windows can be noticed with all Si/$BaSi_2$/Si samples, suggesting it as a good light-absorber candidate for photovoltaic applications. Absorption tails can also be noticed at the near-infrared (NIR) range, which can result from the remaining metallic and defective phases within the film. The sputtered Si/$BaSi_2$/Si structures still present an n-type semiconducting nature indicated by Hall effect measurements. The n-type conductivity nature of unintentionally-doped $BaSi_2$ results from Si vacancies that act as donors [30]. As shown in Figure 7.16a, the electron concentration (n) varies with Si layer thickness. Since interfacial reactions of Si/$BaSi_2$/Si heterostructure is depended on the Si layer thickness, this may alter densities of defect and/or impurities (such as β-$FeSi_2$, Si-NCs) in the $BaSi_2$, thereby influencing the n. Meanwhile, the wider n distribution of $BaSi_2$/Si-20 and -50 can be due to the higher resistivity of the surface layer, consisting of a-Si and BaO, which leads to a higher measurement inaccuracy. The hall mobility (μ_H) of samples is shown in Figure 7.16b. An enhancement of μ_H can be noticed by increasing the d_{Si}. The thicker Si layer can suppress the surface oxidation and

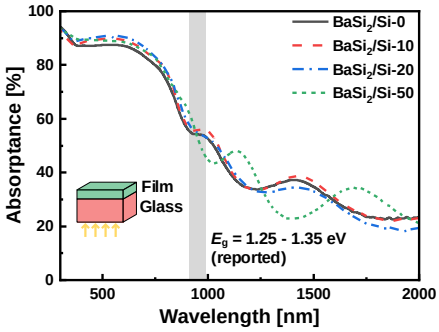

Figure 7.14: Absorptance measured with normal incident radiation from the glass substrate side. The inset sketches the geometry of the optical systems.

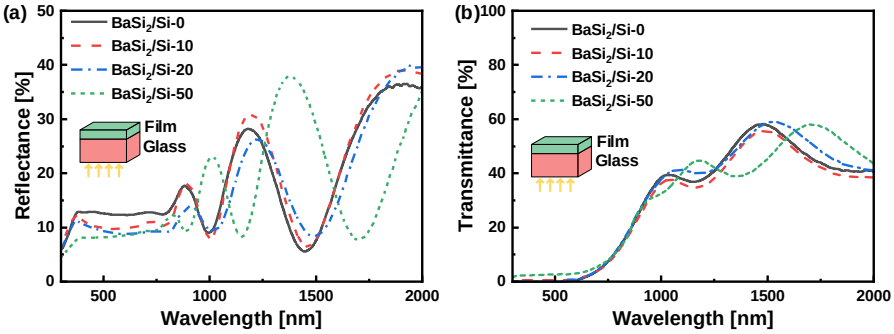

Figure 7.15: Wavelength-dependent (a) reflectance and (b) transmittance curves.

element inter-diffusion, which decreases the concentrations of defects and impurities. This results in the enhancement of the hall mobility. The temperature dependence of

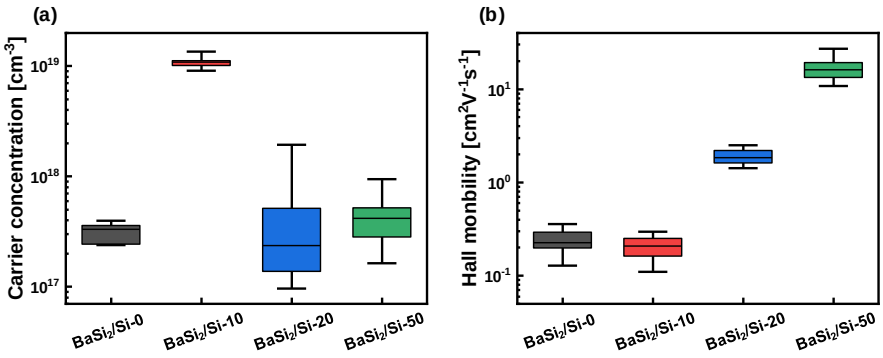

Figure 7.16: Box charts of (a) electron concentration and (b) Hall mobility. The box charts illustrate the interquartile range, median, max, and min values.

transverse electric conductivity (σ) at moderate temperatures is measured, as presented in Figure 7.17a. The lowest conductivity of $BaSi_2$/Si-20 can result from the thicker oxidation layer compared to $BaSi_2$/Si-50, as well as the thicker multi-phase Si layer compared to $BaSi_2$/Si-10 and -0. The highest conductivity of $BaSi_2$/Si-10 corresponds to its higher carrier concentration. The conductivity and temperature (T) exhibit an Arrhenius behavior,

$$\sigma = \sigma_0 \exp(-E_a / kT) \tag{7.4}$$

where k is the Boltzmann constant, σ_0 is a pre-exponential factor, and E_a is the characteristic activation energy. E_a defines the activation energy of the grain-boundary-limited conductivity and depends on the donor ionization energy as well as the barrier height between grains. The relation can be re-written as

$$\ln(1/\sigma) = E_a / kT + \ln(1/\sigma_0) \tag{7.5}$$

which is also known as the Meyer–Neldel rule [31]. Accordingly, E_a can be derived from $\ln(1/\sigma)$ vs $1/kT$ curves. The fitted $\ln(1/\sigma)$ versus $1/kT$ curves are shown in Figure 7.17b. And the fitting data are summarised in Table 7.1. All samples present low values of E_a. $BaSi_2$/Si-0, -10 and -50 exhibit the E_a of 68.01, 67.26, and 65.87 meV, respectively. While, $BaSi_2$/Si-20 possesses a slightly higher E_a of 105.77 meV. The difference of E_a among samples can result from factors such as defect density, grain size, bulk crystallinity, impurities, etc., which need to be further identified.

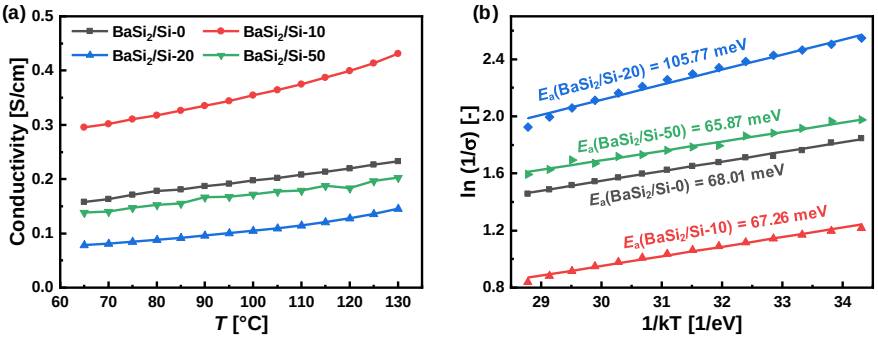

Figure 7.17: (a) Temperature-depended electric conductivity at the moderate temperature range. (b)$\ln(1/\sigma)$ versus $1/kT$ curves wherein the plot slope indicates the electron activation energy E_a.

Table 7.1: Fitting results for $\ln(1/\sigma)$ versus $1/kT$ curves.

Samples	E_a meV	E_a Standard Error meV	σ [S/cm]	σ Standard Error [S/cm]
$BaSi_2$/Si-0	68.01	1.17	1.6375	0.0353
$BaSi_2$/Si-10	67.26	1.83	2.9034	0.0546
$BaSi_2$/Si-20	105.77	3.75	2.8818	0.1055
$BaSi_2$/Si-50	65.87	2.43	1.3293	0.0712

7.4. Conclusions

Our results offer insights into structural and compositional variations of Si/$BaSi_2$/Si architectures which may contribute to the development of thin-film $BaSi_2$/Si heterojunction solar cells. Indeed, high-temperature annealing induces drastic structural and compositional variations at $BaSi_2$/Si hetero-interface wherein film oxidation and Ba depletion alter the elemental distributions and chemical combinations. The thickness of the Si layer influences oxide layer growth, Ba depletion, and multi-phase Si layer formation at the hetero-interfaces. The outcomes of this work can be extended to $BaSi_2$ deposited by other techniques and lead to implementation in photovoltaic applications. This, in turn, may open new opportunities and generate substantial advantages in $BaSi_2$ development, spinning from improvement on material qualities and deployment in thin-film solar cells.

References

[1] Y. Tian, A. R. Bento Montes, Ľ. Vančo, M. Čaplovičová, P. Vogrinčič, P. Šutta, L. Satrapinskyy, M. Zeman, and O. Isabella, *Toward $BaSi_2$/Si heterojunction thin-film solar cells: Insights into heterointerface investigation, barium depletion, and silicide-mediated silicon crystallization,* Advanced Materials Interfaces **7**, 2000887 (2020).

[2] M. Kobayashi, K. Morita, and T. Suemasu, *Growth and characterization of group-III impurity-doped semiconducting $BaSi_2$ films grown by molecular beam epitaxy,* Thin Solid Films **515**, 8242 (2007).

[3] M. Takeishi, Y. Matsumoto, R. Sasaki, T. Saito, and T. Suemasu, *Growth of Al-doped p-type $BaSi_2$ films by molecular beam epitaxy and the effect of high-temperature annealing on their electrical properties,* Physics Procedia **11**, 27 (2011).

[4] M. A. Khan, M. Takeishi, Y. Matsumoto, T. Saito, and T. Suemasu, *Al- and Cu-doped $BaSi_2$ films on Si(111) substrate by molecular beam epitaxy and evaluation of depth profiles of Al and Cu atoms,* Physics Procedia **11**, 11 (2011).

[5] K. O. Hara, N. Usami, Y. Hoshi, Y. Shiraki, M. Suzuno, K. Toko, and T. Suemasu, *Structural study of BF_2 ion implantation and post annealing of $BaSi_2$ epitaxial films,* Japanese Journal of Applied Physics **50**, 121202 (2011).

[6] M. A. Khan, T. Saito, K. Nakamura, M. Baba, W. Du, K. Toh, K. Toko, and T. Suemasu, *Electrical characterization and conduction mechanism of impurity-doped $BaSi_2$ films grown on Si(111) by molecular beam epitaxy,* Thin Solid Films **522**, 95 (2012).

[7] M. A. Khan, K. O. Hara, W. Du, M. Baba, K. Nakamura, M. Suzuno, K. Toko, N. Usami, and T. Suemasu, *In-situ heavily p-type doping of over 10^{20} cm^{-3} in semiconducting $BaSi_2$ thin films for solar cells applications,* Applied Physics Letters **102**, 112107 (2013).

[8] K. O. Hara, N. Usami, M. Baba, K. Toko, and T. Suemasu, *N-type doping of $BaSi_2$ epitaxial films by arsenic ion implantation through a dose-dependent carrier generation mechanism,* Thin Solid Films **567**, 105 (2014).

[9] K. O. Hara, Y. Hoshi, N. Usami, Y. Shiraki, K. Nakamura, K. Toko, and T. Suemasu, *N-type doping of $BaSi_2$ epitaxial films by phosphorus ion implantation and thermal annealing,* Thin Solid Films **557**, 90 (2014).

[10] T. Suemasu, *Exploring the possibility of semiconducting $BaSi_2$ for thin-film solar cell applications,* Japanese Journal of Applied Physics **54**, 07JA01 (2015).

[11] Q. Deng, H. Chen, H. Liao, L. Chen, G. Wang, S. Wang, and Y. Shen, *Numerical simulation and optimization of Si/$BaSi_2$ heterojunction and $BaSi_2$ homojunction solar cells,* Journal of Physics D: Applied Physics **52**, 075501 (2018).

[12] K. Kodama, R. Takabe, T. Deng, K. Toko, and T. Suemasu, *Spectroscopic evidence of photogenerated carrier separation by built-in electric field in Sb-doped n-$BaSi_2$/B-doped p-$BaSi_2$ homojunction diodes,* Japanese Journal of Applied Physics **57**, 050310 (2018).

[13] K. Kodama, Y. Yamashita, K. Toko, and T. Suemasu, *Operation of $BaSi_2$ homojunction solar cells on p^+-Si(111) substrates and the effect of structure parameters on their performance,* Applied Physics Express **12**, 041005 (2019).

[14] R. A. McKee, F. J. Walker, J. R. Conner, and R. Raj, *$BaSi_2$ and thin film alkaline earth silicides on silicon,* Applied Physics Letters **63**, 2818 (1993).

[15] S. Yachi, R. Takabe, H. Takeuchi, K. Toko, and T. Suemasu, *Effect of amorphous si capping layer on the hole transport properties of $BaSi_2$ and improved conversion efficiency approaching 10% in p-$BaSi_2$/n-Si solar cells,* Applied Physics Letters **109**, 072103 (2016).

[16] R. Vismara, O. Isabella, and M. Zeman, *Back-contacted $BaSi_2$ solar cells: An optical study,* Optics Express **25**, A402 (2017).

[17] J.-S. Huang, K.-W. Lee, and Y.-H. Tseng, *Analysis of the high conversion efficiencies $BaSi_2$ and $BaSi_2$ n-i-p thin film solar cells,* Journal of Nanomaterials **2014**, 1 (2014).

[18] M. A. Green, E. D. Dunlop, J. Hohl-Ebinger, M. Yoshita, N. Kopidakis, and A. W. Ho-Baillie, *Solar cell efficiency tables (version 55),* Progress in Photovoltaics: Research and Applications **28**, 3 (2019).

[19] N. A. A. Latiff, T. Yoneyama, T. Shibutami, K. Matsumaru, K. Toko, and T. Suemasu, *Fabrication and characterization of polycrystalline $BaSi_2$ by RF sputtering,* physica status solidi (c) **10**, 1759 (2013).

[20] T. Yoneyama, A. Okada, M. Suzuno, T. Shibutami, K. Matsumaru, N. Saito, N. Yoshizawa, K. Toko, and T. Suemasu, *Formation of polycrystalline $BaSi_2$ films by radio-frequency magnetron sputtering for thin-film solar cell applications,* Thin Solid Films **534**, 116 (2013).

[21] K. O. Hara, Y. Nakagawa, T. Suemasu, and N. Usami, *Realization of single-phase $BaSi_2$ films by vacuum evaporation with suitable optical properties and carrier lifetime for solar cell applications,* Japanese Journal of Applied Physics **54**, 07JE02 (2015).

[22] Y. Tian, R. Vismara, S. Van Doorene, P. Šutta, Ľ. Vančo, M. Veselý, P. Vogrinčič, O. Isabella, and M. Zeman, *Oxidation-induced structure transformation: Thin-film synthesis and interface investigations of barium disilicide toward potential photovoltaic applications,* ACS Applied Energy Materials **1**, 3267 (2018).

[23] T. Yoshitake, T. Nagamoto, and K. Nagayama, *Microstructure of β-$FeSi_2$ thin films prepared by pulsed laser deposition,* Thin Solid Films **381**, 236 (2001).

[24] Y. Tian, A. R. Montes, Ľ. Vančo, O. Isabella, and M. Zeman, *Properties of sputtered $BaSi_2$ thin films annealed in vacuum condition,* Japanese Journal of Applied Physics **59**, SFFA03 (2020).

[25] A. G. Birdwell, R. Glosser, D. N. Leong, and K. P. Homewood, *Raman investigation of ion beam synthesized β-$FeSi_2$,* Journal of Applied Physics **89**, 965 (2001).

[26] G. Faraci, S. Gibilisco, P. Russo, A. R. Pennisi, and S. L. Rosa, *Modified raman confinement model for Si nanocrystals,* Physical Review B **73** (2006), 10.1103/physrevb.73.033307.

[27] T. Sato, H. Hoshida, R. Takabe, K. Toko, Y. Terai, and T. Suemasu, *Detection of local vibrational modes induced by intrinsic defects in undoped $BaSi_2$ light absorber layers using raman spectroscopy,* Journal of Applied Physics **124**, 025301 (2018).

[28] C. Hayzelden, J. L. Batstone, and R. C. Cammarata, *Insitutransmission electron microscopy studies of silicide-mediated crystallization of amorphous silicon,* Applied Physics Letters **60**, 225 (1992).

[29] C. Hayzelden and J. L. Batstone, *Silicide formation and silicide-mediated crystallization of nickel-implanted amorphous silicon thin films,* Journal of Applied Physics **73**, 8279 (1993).

[30] R. Takabe, T. Deng, K. Kodama, Y. Yamashita, T. Sato, K. Toko, and T. Suemasu, *Impact of Ba to Si deposition rate ratios during molecular beam epitaxy on carrier concentration and spectral response of $BaSi_2$ epitaxial films,* Journal of Applied Physics **123**, 045703 (2018).

[31] A. Yelon and B. Movaghar, *Microscopic explanation of the compensation (Meyer-Neldel) rule,* Physical Review Letters **65**, 618 (1990).

8

Conclusion

8.1. Conclusion

In this thesis, insights and knowledge of synthesis and characterizations of sputtered $BaSi_2$ films are presented, which can serve as the foundation for the development of high-quality $BaSi_2$ films and efficient $BaSi_2$-based solar cells. As a low-cost thin-film deposition technique, RF magnetron sputtering is employed for the deposition of $BaSi_2$ films at room-temperature condition. Subsequent post-growth annealing treatments are applied for the material crystallization. Comprehensive structure, composition, and properties characterizations have been executed to acquire a deep understanding of $BaSi_2$. The results and outcomes of this thesis can be concluded as follows:

- **Deposition of $BaSi_2$ thin films**.

  $BaSi_2$ films are deposited by sputtering a stoichiometric $BaSi_2$ target at room temperature, as presented in Chapter 4. The substrate-to-target distances d_{T-S} affects the film thickness uniformity and deposition rate that a larger d_{T-S} enhances the thickness uniformity while decreases the deposition rate. With d_{T-S} = 135 mm, the sputtered $BaSi_2$ film shows a relative uniform distribution of thickness with a moderate deposition rate around 6.6 nm/min. According to the AES depth profiling, the as-deposited $BaSi_2$ film shows a homogeneous and stoichiometric composition. However, the as-deposited samples show an amorphous structure. Further treatments are needed to obtain crystalline films.

- **Post-growth annealing treatments**.
  To obtain crystalline $BaSi_2$ films, various post-growth annealing methods are applied, including:

  - **Annealing in an N_2 atmosphere under an atmospheric pressure**.
    Poly-crystalline $BaSi_2$ thin films are obtained after the annealing at temperatures over 600 °C in N_2 atmosphere. The annealed $BaSi_2$ films show a multi-phase composition and an inhomogeneous structure in the depth direction, as shown in Chapter 4. Besides orthorhombic $BaSi_2$, cubic and hexagonal phases, as well as other Si-Ba compounds (e.g., Ba_5Si_3)are detected in the annealed films by XRD. Silicon nano-crystals were also observed by Raman spectroscopy. The AES depth composition profiles and cross-section TEM images portray a layered structure of the annealed $BaSi_2$ film, consisting of a surface oxide layer, a Si-rich $BaSi_2$ layer, and an inter-diffusion layer (the interfacial region between $BaSi_2$ film and the substrate). The thick surface oxide layer around 200 nm hinders the electrical characterization of the annealed $BaSi_2$f films. These composition and structure features of annealed $BaSi_2$ films originate from surface oxidation and elemental diffusion under high-temperature conditions. Accordingly, an oxidation-induced structure transformation mechanism is proposed to interpret the transition from once homogenous and stoichiometric films to the layered and multi-phase structure. This theory is not limited to the sputtered films but also can be extended to epitaxial and evaporated $BaSi_2$ thin films that are treated under high-temperature conditions.

– **Annealing under a vacuum condition**.

For the sake of avoiding surface oxidation, the annealing processes of $BaSi_2$ are carried out under a vacuum condition, which is discussed in Chapter 5. Indeed, employing the vacuum condition can suppress the surface oxidation to some degree, which reduces the thickness of the oxide layer to ~100 nm from ~200 nm (in the N_2 annealing atmosphere). As a result, less elemental diffusion occurs, and a stoichiometric $BaSi_2$ layer can be observed in the sample. The thinner oxide layer allows the electrical characterizations of annealed $BaSi_2$ films which show an n-type conductivity with an electron concentration of $n = 3 \times 10^{17}$ cm^{-3}. The annealing temperature of 600 °C with a duration of 30 min is sufficient to promote the $BaSi_2$ crystallization in vacuo.

– **Face-to-face annealing under a vacuum condition**.

In Chapter 6, the so-called face-to-face annealing (FTFA) approach has been introduced for the post-growth treatment of sputtered $BaSi_2$ films for the material crystallization and thin-film property improvements from perspectives of surface homogeneity and crystal quality. In the FTFA approach, two $BaSi_2$ films are placed together, the film surface to the film surface. The FTFA sample shows an obvious improvement of surface homogeneity depicted by both optical microscopy and Raman mapping. FTFA method can suppress the formation of silicon nano-crystals and $FeSi_2$ according to the disappearances of their peaks in Raman spectra. By employing various covers for FTFA including $BaSi_2$, silicon, and glass, $BaSi_2$ films exhibits a transition of conductivity type from n- to p-type. Impacts of FTFA on $BaSi_2$ films originate from two aspects: i) the confined $BaSi_2$ surface annealing condition suppresses the oxidation and elemental diffusion, and ii) the altered heat-transfer system tunes the degree of film crystallization as well as the electrical and optical properties. Based on this research, further improvement of $BaSi_2$ film quality can emerge by the delicate design of the annealing configurations, the optimization of FTFA parameters, and the comprehensive understanding of mechanisms of FTFA on film crystallization.

- **Interface investigations on Si/$BaSi_2$/Si heterostructures**.

Interfaces and surfaces are of great significance for the development of efficient photovoltaic devices. Chapter 7 presents a comprehensive interface investigation of Si/$BaSi_2$/Si heterostructures, serving as the foundation for the design and realization of $BaSi_2$/Si heterojunction thin-film solar cells. Si/$BaSi_2$/Si heterostructures are fabricated by sputtering an intrinsic silicon target and a $BaSi_2$ target. By tailoring Si layer thickness (d_{Si}), composition and structure variations of the Si/$BaSi_2$/Si heterostructures under high-temperature conditions are observed. Raman spectral mapping, SEM, AES, STEM-EDS are applied for structure and composition analysis. In the cases of thinner $d_{Si} < 20$ nm, oxidation at the surface region leads to an inhomogeneous structure in both lateral and depth directions, while the Ba diffusion at the bottom side leads to the disappearance of the deposited Si layer. The thicker Si layer ($d_{Si} > 20$ nm) can effectively suppress the surface oxidation and Ba diffusion, in which Si layers can be observed at both

surface and bottom side of Si/$BaSi_2$/Si heterostructures. The process of structure and composition variations of Si/$BaSi_2$/Si samples consist of the oxidation of deposited Si layer, growth of the oxide layer, Ba diffusion and depletion, as well as Si isolation and crystallization. These interfacial phenomena lead to the complex structure and composition of Si/$BaSi_2$/Si heterostructures, which need additional attention for the design and fabrication of $BaSi_2$/Si heterojunction thin-film solar cells.

8.2. Outlook

Results in this work focus on the insights and understanding of the material behavior of sputtered $BaSi_2$ with subsequent high-temperature annealing. We have attempted to fabricate $BaSi_2$ thin-film solar cells on the basis of *n-i-p* a-Si:H solar cell architectures, wherein the a-Si:H absorber layer was directly replaced by sputtered $BaSi_2$. Yet we failed to obtain a working device, which may be caused by

- the thick oxide layer hindering carrier transport;
- thermal expansion mismatch leading the layer exfoliation;
- reactions between $BaSi_2$ with other layers, e.g., TCO and SiO_x;
- the instability of $BaSi_2$ in oxidizing or moist environments;
- high-volume of defects in the sputtered $BaSi_2$;
- insufficient knowledge of sputtered $BaSi_2$ electronic and optical properties for cell architecture designs;
- few investigations and research upon materials capable to form junctions with $BaSi_2$;
- lack of effective measures to precisely control the composition and properties of sputtered $BaSi_2$, etc.

Herein, the future research outlook of the $BaSi_2$ for photovoltaics is given from the perspectives of material research and device development.

8.2.1. Material research

Recommendations of further material-level research on $BaSi_2$ are given as follows:

- **Sputtering process:**
  - **Composition-tunable sputtering process**. In this research, a stoichiometric $BaSi_2$ target is applied for the depositions. Based on the research on epitaxial $BaSi_2$ films, the slightly Ba-rich composition benefits the opto-electronic performance of $BaSi_2$ [1]. It is challenging to control the Ba/Si ratio of the sputtered $BaSi_2$ film by using the stoichiometric $BaSi_2$ target. To obtain Ba-rich sputtered films, a method of adding supplementary Ba source on the $BaSi_2$

target for sputtering has been reported [2]. However, this method can hardly ensure a precise composition control of deposited films, and may even cause some irreversible damages of the $BaSi_2$ target. Indeed, co-sputtering of Ba and Si targets may allow the precise composition control of sputtered $BaSi_2$ by adjusting deposition rates of Ba and Si separately. Composition-tunable sputtered films can definitely broaden the research on sputtered $BaSi_2$ and accelerate the progress of manufacturing high-quality sputtered $BaSi_2$ films.

- **High-temperature depositions with Ar/H plasma**. The passivation effect of H plasma treatments has been studied with epitaxial $BaSi_2$ films [3, 4]. Replacing the Ar gas by the Ar/H_2 mixed gas for sputtering may enable the material passivation during its growth. Due to the temperature limitation of the sputtering equipment, we have tried to fabricate $BaSi_2$ films by using the Ar/H_2 mix gas at room temperature with post-growth annealing. No obvious property improvement or composition change can be observed with the samples. This may be caused by the H emission during the annealing process. Methods such as sputtering deposition with heated substrates or post-growth annealing in the H_2 atmosphere may help.
- **Flexible substrates**. Sputtering enables thin-film deposition on various substrates. Substrates including glass, quartz, and silicon wafers have been used in this work. The possibility of $BaSi_2$ deposition on flexible substrates remains to be explored. Given the high-temperature conditions required for film crystallization, metal foils can be regarded as good candidates as flexible substrates. The possible reactions between the metal foils and $BaSi_2$ as well as their thermal expansion difference need to be considered and investigated.

- **Material properties**
  - **Optical properties**. Sputtered $BaSi_2$ films show a complex layer structure due to the surface oxidation. This increases the difficulty for optical characterizations of $BaSi_2$, such as determinations of refractive index n, and extinction coefficient k, and absorption coefficient α. Efforts are still needed to extract these parameters of sputtered $BaSi_2$ films from optical characterizations such as spectroscopic ellipsometry and UV-vis-NIR spectroscopy.
  - **Impurity elements**. Major impurity elements in sputtered $BaSi_2$ include O, Fe, N, and C. Among them, O, N, and C can originate from residual air in the deposition, while the Fe may come from the target or sputtering apparatuses. Further research is needed to determine the origin of these impurities. Besides, a deeper understanding of their impacts on film properties is essential to improve the film quality.
  - **Defects**. It is of great importance to identify the defects in $BaSi_2$ films. Various techniques can be used for the defect study of $BaSi_2$, including deep-level transient spectroscopy (DLTS), positron annihilation spectroscopy (PAS), electron paramagnetic resonance spectroscopy (EPR), etc. Theoretical research on defects is also important for $BaSi_2$ development, such as the calculation

research on point defects and defect complexes (the combination of two-point defects) [5].

- **Wet and dry etching**

  Etching is critically important for device fabrication, and useful for understanding $BaSi_2$ properties. For instance, after removing the surface oxide layer of sputtered $BaSi_2$ by etching, we may be able to accurately determine the optical and electronic properties of the material. Both wet and dry etching methods can be applied. There are some concerns about the research of etching methods:

  - **Wet etching**. Finding suitable etchants for a controllable process is crucial for wet etching. According to our processing experience, both as-deposited and annealed $BaSi_2$ show high reactivity with water and acid. Hence, applications of aqueous solutions as etchants need to be carefully considered.
  - **Dry etching**. We attempted to remove the surface layer of sputtered $BaSi_2$ by reactive ion etching with chlorine plasma, which resulted in the formation of a high-resistivity surface of the etched sample. Hence, it is also crucial to choose suitable plasma etchants for $BaSi_2$ films.

- **Chemical properties of $BaSi_2$**. Currently, most researches of $BaSi_2$ focus more on the physical properties of $BaSi_2$ films. It is important to understand the chemical properties of $BaSi_2$ films. In this research, various chemical reactions are involved in the manufacturing of $BaSi_2$ films, e.g., oxidation (both during and after depositions), Ba depletion, silicon isolation, etc. However, these reactions are our speculation based on the film composition analysis. To obtain high-quality thin-film $BaSi_2$, it is important to get a deeper understanding of these chemical variations through simulation and/or experimental methods. Meanwhile, the instability of $BaSi_2$ in a moist or oxidizing environment is crucial for its deployment in practical applications, about which no systematic research has been carried out. A comprehensive understanding of $BaSi_2$ from both physical and chemical aspects can definitely accelerate the development of the material.

8.2.2. Device development

To date, no efficient solar cell that uses $BaSi_2$ as the absorber material has been reported. It is crucial to understand the factors that hinders the fabrication of efficient $BaSi_2$-based solar cells. If we limit the scope to the sputtered $BaSi_2$, one of the key factors is the material quality. Obtaining PV-grade $BaSi_2$-based films is the first step towards the efficient solar cells, which can stem from two aspects: i) the definition of “PV-grade” for $BaSi_2$, and ii) the approach to achieve it.

This preliminary research on sputtered $BaSi_2$ is driven by the considerations upon depositions and post-growth treatments to understand material properties and to identify the challenges for the material development. To accelerate the progress of sputtered $BaSi_2$ towards PV applications, we need to get a clear definition of "high quality" and/or "PV-grade" for $BaSi_2$ films, on the basis of requirements of designed solar cell structures,

current research results on material properties, and limitations of manufacturing processes. A better understanding of the gap between the fabricated materials and device-required materials is of great significance for the development of $BaSi_2$-based solar cells.

Besides, there are some general recommendations on the $BaSi_2$ solar cell development, which is not limited to sputtered films:

- **Selections of suitable materials for forming the junction with $BaSi_2$.** The high reactivity of $BaSi_2$, as well as its material-synthesis conditions (e.g., high temperature) make it challenging to find suitable candidate materials. Well-performed junctions are the basics of solar cell fabrications and optimizations.

- **Controllable doping process of $BaSi_2$.** Controllable doping process of $BaSi_2$ films deposited by MBE has been reported. It is necessary to develop the doping process for $BaSi_2$ films deposited by low-cost techniques such as sputtering and thermal evaporation. Doped-$BaSi_2$ expands the possibility of solar cell architecture design.

Studies in solar cell structure design, interface engineering, light management, device stability, etc., are also of great importance. All of these are on the basis of a comprehensive understanding of the material. It is still a long way off from high-performance $BaSi_2$-based solar cells. This work sheds some light on the development of sputtered $BaSi_2$ films. Consistent efforts are needed for the goal of low-cost and high-efficiency $BaSi_2$-based thin-film solar cells.

References

[1] R. Takabe, T. Deng, K. Kodama, Y. Yamashita, T. Sato, K. Toko, and T. Suemasu, *Impact of Ba to Si deposition rate ratios during molecular beam epitaxy on carrier concentration and spectral response of $BaSi_2$ epitaxial films,* J. Appl. Phys. **123**, 2 (2018).

[2] S. Matsuno, R. Takabe, S. Yokoyama, K. Toko, M. Mesuda, H. Kuramochi, and T. Suemasu, *Significant photoresponsivity enhancement of polycrystalline $BaSi_2$ films formed on heated Si(111) substrates by sputtering,* Applied Physics Express **11**, 071401 (2018).

[3] Z. Xu, D. A. Shohonov, A. B. Filonov, K. Gotoh, T. Deng, S. Honda, K. Toko, N. Usami, D. B. Migas, V. E. Borisenko, and T. Suemasu, *Marked enhancement of the photoresponsivity and minority-carrier lifetime of $BaSi_2$ passivated with atomic hydrogen,* Physical Review Materials **3**, 065403 (2019).

[4] Z. Xu, T. Sato, L. Benincasa, Y. Yamashita, T. Deng, K. Gotoh, K. Toko, N. Usami, A. B. Filonov, D. B. Migas, D. A. Shohonov, and T. Suemasu, *Atomic hydrogen passivation for photoresponsivity enhancement of boron-doped p-$BaSi_2$ films and performance improvement of boron-doped p-$BaSi_2$/n-Si heterojunction solar cells,* Journal of Applied Physics **127**, 233104 (2020).

[5] M. Kumar, N. Umezawa, and M. Imai, *Recent advances in computational studies of thin-film solar cell material $BaSi_2$,* Japanese Journal of Applied Physics **59**, SF0803 (2020).

Acknowledgements

In all probability, you may start reading my thesis from this page. You may also find your name mentioned here. My sincerest apologies if I have left you out. Indeed, I could not have done this without help from you. I wish to thank all the people whose assistance was a milestone in the completion of this project.

First and foremost, I would like to express my deepest gratitude to my promotors Prof. Miro Zeman and Dr. Olindo Isabella for their support and help at every stage of the research project. With immense knowledge and plentiful experience, Miro can always provide advice and insights from a helicopter view that deepens my understanding of the research project from various perspectives. Those advanced material characterizations cannot be done without the support and help from Miro. As my promotor and daily supervisor, Olindo is always available for offering advice, support, and help. His unwavering support and belief in me created a pleasant research atmosphere with complete freedom during this project. Rather than pushing me forward, Olindo gave me a chance to handle the research at my pace. Besides, his positive attitude, critical views on the work, and timely responses every time were always very helpful for me. It is wholeheartedly appreciated that great advice and support from both of you for my research proved monumental towards the success of this project.

I would like to pay my special regards to committee members, Prof. Takashi Suemasu, Prof. Simona Olga Binetti, Prof. Pere Roca i Cabarrocas, Prof. Bernard Dam, Dr. Stephan Eijt, Prof. Peter Palensky, for evaluating my thesis. Their constructive and insightful feedbacks are valuable for the refinement of my thesis.

I would like to recognize the invaluable assistance and help from Dr. Ľubomír Vančo with the material characterizations with AES and Raman, and his advice and suggestions in my research. It was a great experience to talk with him and visit his laboratory in Bratislava. I am deeply grateful to Dr. Pavol Šutta for the help with the XRD analysis. I am indebted to Mária Čaplovičová, Peter Vogrinčič, and Dr. Leonid Satrapinskyy for their help with STEM measurements and lamella sample preparations.

The four-year experience in Photovoltaic Materials and Device group is pleasant and fruitful. What makes it possible is the people in the group who I worked with, Prof. Arno Smets, Dr. René van Swaai, Prof. Arthur Weeber, Dr. Hesan Ziar, Dr. Rudi Santbergen, Dr. Luana Mazzarella, Dr. Guangtao Yang, Dr. Fai Tong Si, Dr. Paula Perez Rodriguez, Dr. Yuan Gao, Dr. Dimitris Deligiannis, Dr. Gianluca Limodio, Dr. Robin Vismara, Dr. Nasim Rezaei, Johan Blanker, Dr. Paul Procel, Dr. Engin Özkol, Dr. Gregory Pandraud, Klaas Bakker, Thierry de Vrijer, Andres Calcabrini, Ana Rita Bento Montes, Juan Camilo Ortiz Lizcano, Yifeng Zhao, Dr. Carlos Ruiz Tobon, Can Han, Manvika Singh, Yilong Zhou, and Yudai Yamashita. I would like to offer my special thanks to Guangtao for his assistance and help at every stage of the research project. I wish to show my gratitude to Fai Tong for his invaluable suggestions both in research and life. I am indebted to Robin and Steve Van Doorene who contributed a great deal to the early stage of the project, Rita

who joined the research in the most difficult and challenging stage of the project, and Nasim who took over the research on $BaSi_2$. I would like to extend my thanks to Gianluca, Yifeng, and Yiran Zhao for their help with the substrate preparations in this research, Pual and Can for their inspiring discussions and suggestions, Daan Bijl for his help with translating the Dutch summary of the thesis. I would like to pay my special regards to Martijn Tijssen, Stefaan Heirman, and Remko Koornneef for their technical support. I am thankful to Ilona van der Wenden, Sharmila Rattansingh, Ellen Schwencke-Karlas, and Mark Vielvoije for their daily support and assistance.

很久没有写中文的内容了，如果要追溯到上次，可能就是硕士毕业论文了。在这边呆久了，中文慢慢退步了：很多字看着熟悉，却下不了笔；有的话到了嘴边，却想不起下句是什么。若是没有拼音输入法，可能要守着字典写这篇致谢。

过去的一年，感触最多可能就是“武汉”这两个字了。武汉，从一个曾经需要我用北京和上海定位向人介绍的城市，突然变得“世界闻名”，其中总有种莫名的滋味。小时候觉得武汉很大，感觉怎么走都走不出水果湖；长大点，感觉武汉变小了，走出教室就能看着黄鹤楼；离开了武汉，有了对比才发觉武汉的破，到处都是挖不完的坑；离的久了，才想起到武汉的好，一碗面，一份豆皮，一个面窝，一瓢藕汤的好。又想回家吃饭了，这大抵是每个离家久了的人的共同想法吧。在武汉度过了我（到目前为止）人生的三分之二以上，知识的积累和性格的养成大概都得益于武汉的这一方水土。能完成博士论文，绝离不开这一路的点点滴滴，从水果湖到省实验，从华科到浙大。这一路上，有太多的人的照顾和帮助，没有机会对每一个人说一声谢，只能祝愿你们福泰安康，前程似锦！

我想感谢我的父母，他们以他们最大的努力给我创造了最好的条件，像他们所说的，比上不足，比下有余吧！能把我塞到我的小学着实也是花了不少功夫。我能取得今天小小成就，离不开他们默默的支持和关心！我还要感谢我的弟弟，能有个弟弟确实难得，可以从小就有一个玩伴。也要感谢女友的父母，他们一直给于我们无微不至的关心和支持，让我们没有过多的顾虑。最后，我还要感谢我的女友，感谢你这一路的陪伴和支持，尤其是在疫情的这一年。

田义磊

Curriculum Vitæ

Yilei TIAN

2009 – 2013	Bachelor of Engineering Huazhong University of Science and Technology, Wuhan, China
2013 – 2016	Master of Engineering Zhejiang University, Hangzhou, China *Thesis:* Tuning the Surface Roughness and Wettability of Vertical Graphene Channels for Supercapacitor Energy Storage *Supervisor:* Prof.dr. Z. Bo
2016 – 2021	PhD Delft University of Technology, Delft, the Netherlands *Thesis:* Barium Disilicide for Photovoltatic Applications: Thin-Film Synthesis and Characterizations *Promotors:* Prof.dr. M. Zeman Dr. O. Isabella

List of Publications

Peer-reviewed journal articles in this thesis

1. **Y. Tian**, R. Vismara, S. van Doorene, P. Šutta, Ľ. Vančo, M. Veselý, P. Vogrinčič, O. Isabella, and M. Zeman, *Oxidation-Induced Structure Transformation: Thin-Film Synthesis and Interface Investigations of Barium Disilicide toward Potential Photovoltaic Applications*, ACS Applied Energy Materials, **1**, 7, (2018).

2. **Y. Tian**, A.Montes, Ľ. Vančo, O. Isabella, and M. Zeman, *Properties of Sputtered $BaSi_2$ Thin Films Annealed in Vacuum Condition*, Japanese Journal of Applied Physics, **59**, SFFA03, (2020).

3. **Y. Tian**, A. Montes, Ľ. Vančo, M. Čaplovičová, P. Vogrinčič, P. Šutta, L. Satrapinskyy, M. Zeman, and O. Isabella, *Towards $BaSi_2$/Si Heterojunction Thin-film Solar Cells: Insights into Hetero-Interface Investigation, Barium Depletion, and Silicide-mediated Silicon Crystallization*, Advanced Materials Interfaces, **7**, 19 (2020).

4. **Y. Tian**, M. Zeman, and O. Isabella, *Face-to-face Annealed Sputtered $BaSi_2$: Investigations on Surface Homogeneity, Film Properties, and Annealing Mechanisms*, Physical Review Materials, **4**, 12, 125403, (2020).

Conference contributions related to this thesis

Poster presentations

1. **Y. Tian**, R. Vismara, S. van Doorene, P. Šutta, Ľ. Vančo, M. Veselý, P. Vogrinčič, O. Isabella, and M. Zeman, 33rd European Photovoltaic Solar Energy Conference and Exhibition (EU PVSEC), Amsterdam, (2017).

2. **Y. Tian**, R. Vismara, S. van Doorene, P. Šutta, Ľ. Vančo, M. Veselý, P. Vogrinčič, O. Isabella, and M. Zeman, International Photovoltaic Science and Engineering Conference (PVSEC), Otsu, (2017).

3. **Y. Tian**, A. Montes, M. Zeman, and O. Isabella, MRS Fall Meeting & Exhibit, Boston, (2019).

Oral presentations

1. **Y. Tian**, A. Montes, O. Isabella and M. Zeman, 12th International Conference on Advanced Semiconductor Devices and Microsystems (ASDAM), Smolenice, (2018).

2. **Y. Tian**, A. Montes, O. Isabella and M. Zeman, MRS Fall Meeting & Exhibit, Boston, (2018).